Materials Horizons

Two decades of ceria nanoparticles research: structure, properties and emerging applications

Journal:	*Materials Horizons*
Manuscript ID	MH-REV-01-2024-000055.R1
Article Type:	Review Article
Date Submitted by the Author:	06-Apr-2024
Complete List of Authors:	Othman, Ali; Clarkson University, Chemistry + Biomolecular Science Gowda, Akshay ; Clarkson Unviersity, Chemistry & Biomolecular Engineering Andreescu, Daniel; Clarkson University, Chemistry and Biomolecular Science Hassan, Mohamed; Clarkson University Department of Chemistry and Biomolecular Science, Chemistry Babu, S.; Clarkson University, Seo, Jihoon; Clarkson University, Department of Chemical and Biomolecular Engineering Andreescu, Silvana; Clarkson University, Department of Chemistry

Wider Impact Statement

Ceria nanoparticles, or nanoceria is a versatile material with unique and unusual optical, mechanical and catalytic properties. The co-existence of two-oxidation states, Ce^{3+}/Ce^{4+} at the nanoscale level facilitates formation of oxygen vacancies and defect states which confer an extremely high reactivity and the ability to act as a catalyst for both oxidation and reduction reactions. Due to its unique features, we now see a broad interest in the implementation of this material across a wide array of industries. However, its unique features are a function of the chemical, structural, surface defects, size, shape and doping effects which are currently not fully understood.

This review provides a comprehensive, critical, and accessible resource of general interest to the materials community, highlighting the structure and fundamental properties of this unique material and translation of its distinct features into applications. Scientists can use this resource as a starting point to explore this material's unique and unusual properties and pursue avenues for creating new products and breakthrough innovations.

Two decades of ceria nanoparticles research: structure, properties and emerging applications

Ali Othman[a,b†], Akshay Gowda[b†], Daniel Andreescu[a], Mohamed H. Hassan [a], S. V. Babu[b], Jihoon Seo[b*], and Silvana Andreescu[a]*

[a] Department of Chemistry and Biomolecular Science, Clarkson University, Potsdam, New York 13699-5810, USA.

[b] Department of Chemical and Biomolecular Engineering, Clarkson University, Potsdam, New York 13699, USA

*Corresponding Author: E-mail: jseo@clarkson.edu and eandrees@clarkson.edu

[†]*contributed equally to this work.*

Table of Contents

ABSTRACT

Cerium oxide nanoparticles (CeNPs) are versatile materials with unique and unusual properties that vary depending on their surface chemistry, size, shape, coating, oxidation states, crystallinity, dopant, structural and surface defects. This review details advances made over the past twenty years in the development of CeNPs and ceria-based nanostructures, the structural determinants affecting their activity, and translation of these distinct features into applications. The two-oxidation states of nanosized CeNPs (Ce^{3+}/Ce^{4+}) coexisting at the nanoscale level, facilitate formation of oxygen vacancies and defect states which confer extremely high reactivity and oxygen buffering capacity, and the ability to act as catalysts for oxidation and reduction reactions. However, the method of synthesis, surface functionalization, surface coating and defects are important factors in determining their properties. This review highlights the key properties of CeNPs, their synthesis, interactions and reaction pathways, and provides examples of emerging applications. Due to their unique properties, CeNPs have become quintessential candidates for catalysis, chemical mechanical planarization (CMP), sensing, biomedical applications and environmental remediation, with tremendous potential to create novel products and translational innovations in a wide range of industries. This review highlights the timely relevance and the transformative potential of these materials in addressing societal challenges and driving technological advancements across these fields.

1. Introduction

Cerium, a member of the lanthanide series, is the most abundant of all rare earth metals. Unlike others in the series that typically exist in the +3 state, cerium changes between +3 and +4 oxidation states, giving unique redox properties and reactivity. Its oxide form, e.g. ceria, cerium oxide or cerium dioxide (CeO_2) has gained significant interest in both industry and academia. Ceria-based materials, composed of CeO_2, embodies an array of distinctive features that make them highly desirable across many scientific areas and a wide range of industries. The nanosized form of ceria has gained significant attention over the past twenty years owning to its exceptional properties at the nanoscale. The unique crystal structure, characterized by the presence of oxygen vacancies and cerium cations with variable oxidation states confer a plethora of properties including high oxygen storage capacity, redox activity, high surface functionality and catalytic power. Notably, nanoscale ceria can accommodate more oxygen vacancies in its crystal structure than its bulk counterpart [1]. This attribute enables ceria nanoparticles (CeNPs) to exhibit very high oxygen mobility and exceptional oxygen storage capacity (OSC), making them adept at releasing and storing oxygen depending on the redox environment. These distinctive features have spurred intense investigation into CeNPs research and exploration of their properties in applications ranging from catalysis, energy conversion, semiconducting industries to environmental remediation, biosensing and biomedicine.

Ceria-based materials are utilized in catalytic converters, solid oxide fuel cells (SOFCs), catalysts for volatile organic compounds (VOCs) oxidation, sensors and chemical mechanical planarization (CMP). More recently, the scope of CeNPs has expanded to water and CO_2 splitting for hydrogen production and biomedical applications as enzyme mimetics, theranostic probes and therapeutic materials. Over 30,000 articles have been published on synthesis, properties and applications of ceria-based materials,[2-7] many focusing on their role in catalytic, energy and environment. An emerging trend is the exploration of CeNPs in fields like pharmacology, medicine, biosensing and bioimaging[8, 9]. However, challenges like biodistribution, cross-reactivity with clinically relevant species, and potential toxicity constrain their commercial potential[10 11].

This review aims to offer readers a comprehensive understanding of critical physicochemical properties of the CeNPs, focusing on surface modification, doping and structure-activity relationships followed by an exploration of their significant applications. Throughout this review, we will highlight the importance of CeNPs' structural design parameters, interactions, and reactivity in the context of next-generation devices. We will commence by examining the structural and shape-dependent properties of CeNPs, followed by a discussion of size-dependent characteristics, with a particular emphasis on the Ce^{3+}/Ce^{4+} ratio and oxygen vacancies, along with the mechanisms underlying oxygen vacancy formation. Ceria doping is a pivotal focus, as it can substantially enhance ceria's properties, opening doors to innovative applications. We delve into the intricacies of the doping process and the role of doped-ceria in catalytic reactions. Subsequently, we address the antioxidant properties of CeNPs and their interactions with reactive oxygen species (ROS), touching upon their potential applications in catalysis, sensing, and biomedicine. A dedicated section will cover surface functionalization and its crucial role in modulating interactions between NPs and their surrounding environment. Additionally, we will explore the incorporation of CeNPs into composite and nanohybrid structures interfaced with other metals or rare-earth metal oxides,[12] enhancing their performance and augmenting their area of applicability. Finally, we will delineate applications and future directions, encompassing catalysis, CMP, biosensing, and environmental remediation.

2. Physicochemical properties of ceria nanoparticles

Physicochemical properties, including size, shape, crystal plane, surface chemistry, have significant influence over the reactivity of ceria particles. Over the past two decades, substantial efforts have been dedicated to modulating oxygen vacancy levels and Ce^{3+}/Ce^{4+} ratio by manipulating synthesis conditions. A significant body of research has been dedicated to the creation of ceria particles with enhanced reactivity and higher Ce^{3+} concentration at the surface. This can be achieved through variations in surface size and by doping with rare earth (RE), transitional, or noble metals. This interest is driven by CeNPs' remarkable capacity to neutralize free radicals, which has garnered considerable attention in the field of biomedicine. It has led to the development of innovative ceria-based antioxidant therapeutics. The recognized antioxidant activity of CeNPs is strongly linked to their redox activity, the Ce^{3+} levels present at the surface,

and the presence of oxygen vacancies. In this section, our focus will be on elucidating how the structural and physicochemical properties of ceria influence over oxygen vacancies and surface reactivity (**Figure 1**).

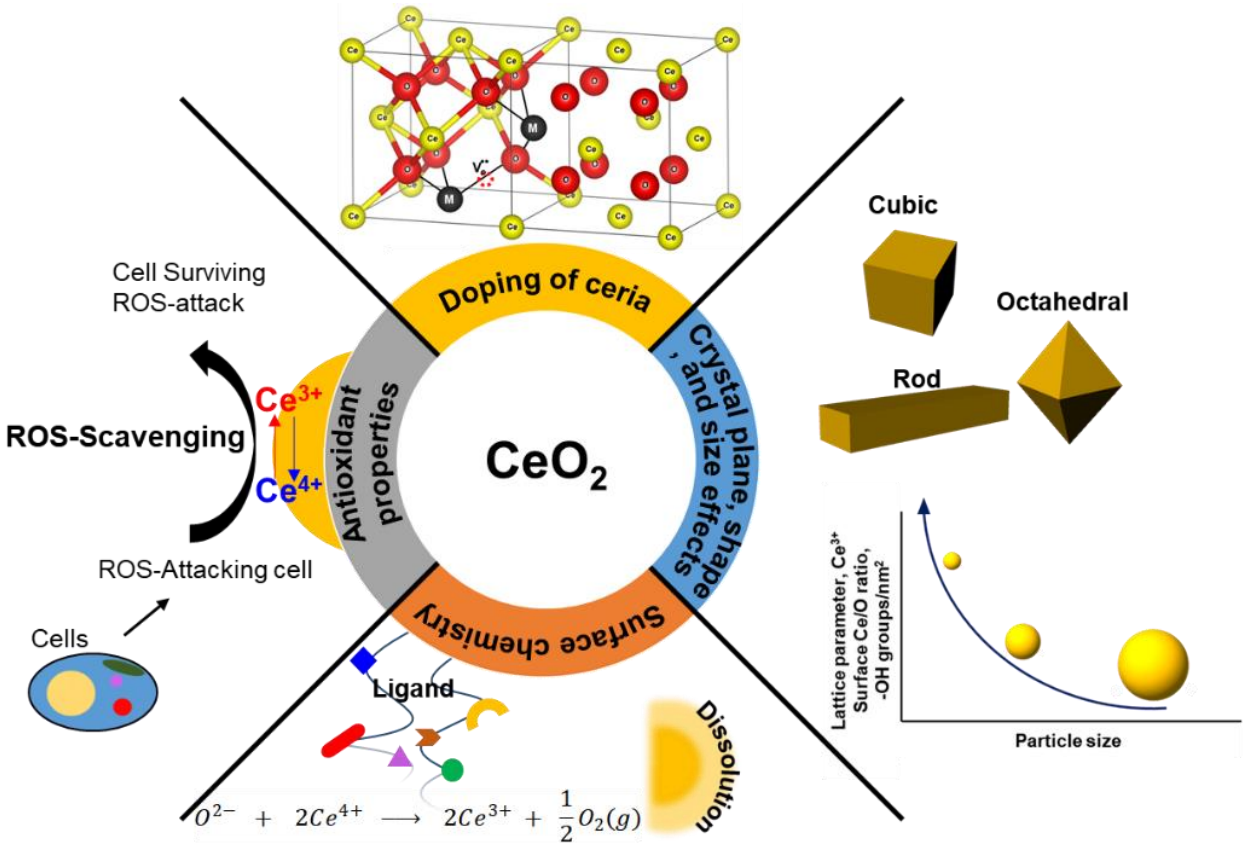

***Figure 1**. Summary of physicochemical properties that influence the reactivity of CeNPs.*

2.1. Structural and defect properties

Bulk cerium oxide or ceria has a fluorite crystal structure with face-centered cubic unit cell (space group F$m\bar{3}m$) and a lattice parameter of 5.411 Å at room temperature. In this arrangement, each Ce^{4+} ion (yellow spheres) is surrounded by eight nearest-neighbor O^{2-} ions (red spheres) forming a cube structure. Each O^{2-} ion is tetrahedrally coordinated to four closest Ce^{4+} ions as depicted in Figure 2a.

Defects within ceria can be introduced by altering factors such as temperature, oxygen partial pressure, electrical field or surface stress, or through the incorporation of other ions, and these defects can be broadly categorized into intrinsic and extrinsic types[1]. Intrinsic defects primarily arise due to thermal fluctuations or interaction with the surrounding environment such as redox

processes. In contrast, extrinsic defects emerge from impurities or the introduction of dopants[1] (will be covered in section **2.4**.). The two most noteworthy intrinsic defects observed in ceria are oxygen vacancies [13, 14] and anion Frenkel defect. In an anion Frenkel defect, an oxygen ion is displaced from its lattice position to an interstitial position, resulting in a defect at the interstitial location and a vacancy at the original position [15]. These defects are typically present in low concentrations and do not impact the lattice change.

In oxygen vacancy type defect, an oxygen vacancy is created due to the liberation of an oxygen ion from a lattice site. The two excess electrons generated by the vacancy created are localized on two neighboring cerium ions thereby reducing Ce^{4+} to Ce^{3+} [16, 17]. This process can be represented as:

$$O^{2-} + 2Ce^{4+} \longrightarrow 2Ce^{3+} + \frac{1}{2}O_2(g) \quad \textbf{(2.1)}$$

$$O_o^x + 2Ce_{Ce}^x \longrightarrow V_o^{\cdot\cdot} + 2Ce'_{Ce} + \frac{1}{2}O_2(g) \quad \textbf{(2.2)}$$

Eq. 2.1 which represents the vacancy formation reaction is written using Kröger-Vink defect notation in **Eq. 2.2** where: Ce_{Ce}^x represents a Ce^{4+} ion on a Ce lattice site, O_o^x represents a O^{2-} ion on an O lattice site, Ce'_{Ce} represents a Ce^{3+} ion on a Ce lattice site and $V_o^{\cdot\cdot}$ represents a neutral oxygen vacancy site.

Formation of an oxygen vacancy results in a decrease in the coordination number of Ce^{4+} to O^{2-} ions and introduces Ce^{3+} ions into the crystal lattice as shown in **Figure 2b**. Ce^{3+} ions have a larger ionic radius (1.034 Å) as compared to Ce^{4+} ions (0.92 Å) [18]. Therefore, the introduction of Ce^{3+} ions and oxygen vacancies results in a distortion (dislocation of atoms from their equilibrium lattice points) of the local symmetry and generates strain in the lattice. Ceria particles release strain by undergoing lattice expansion [19, 20] as shown in **Figure 2b**. Different distortions can be induced due to different Ce^{3+} localization motifs with correspondingly different vacancy formation energies. The localization of electrons upon vacancy formation occurs either on the cerium ions neighboring the vacancy (i.e., Ce–O) or cerium ions next to the nearest neighbor (i.e., Ce–Ce) [21, 22].

2.1.1. Oxygen vacancies

Oxygen vacancy defects can be categorized into surface (present on the surface) and subsurface

oxygen vacancies (present in the bulk) depending on their location [23, 24]. Oxygen vacancies can either be isolated (single oxygen vacancy) or form clusters. Vacancy clusters of different shapes including triangular, dimers and straight lines have been reported[25, 26]. Scanning tunneling microscopy (STM) provided the most visually convincing demonstrations of clusters of oxygen vacancies. Clusters of oxygen vacancies like linear surface vacancy clusters (LSVCs) are more favorable for migration of oxygen in ceria that happens through a vacancy hopping mechanism. STM images showed that one subsurface vacancy per LSVC is necessary [24]. This structural requirement reveals the high reduction tendency of cerium ion upon liberation of an oxygen ion.

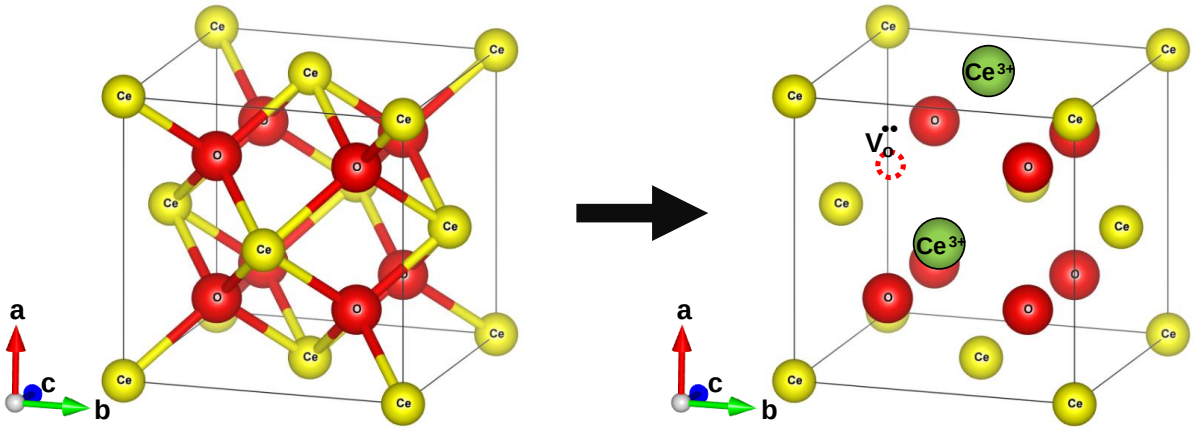

***Figure 2**. Schematic diagram of reversible lattice distortion in a cubic ceria unit cell. (**a**) Fluorite crystal structure of bulk ceria.(**b**) Distorted crystal structure of nanoceria due to the formation of oxygen vacancy and concomitant reduction of Ce^{4+} ions to Ce^{3+} ions. Red and yellow colored spheres represent O^{2-} and Ce^{4+} ions, respectively while green sphere and $V_o^{\bullet\bullet}$*

Yang et al. reported vacancy formation energies of 3.39 and 3.21 eV for surface and subsurface oxygen vacancies, respectively, on a (111) surface, implying that the energies for formation of surface and subsurface vacancies are relatively close to each other[27]. Using state-of-the-art STM as well as DFT calculations, Esch and co-workers showed in an elegant study that the surface oxygen vacancies on (111) a ceria surface are immobile at room temperature and that direct diffusion (movement of lattice oxygen) needs higher temperatures (>400 °C) [24]. Note, that with increasing annealing time, the number of surface defects should decrease due to the small diffusion barrier offering it highly mobile at the elevated temperatures in which the clustering of surface vacancies is energetically unfavorable [28].

Figure 3a and **Figure 3b** show the two types of vacancies, namely surface and subsurface oxygen vacancies, identified on a partially reduced ceria surface in filled-state and empty-state,

respectively. Both types of vacancies were present with similar coverages. This observation was indeed in line with their DFT calculations, which predicted the same vacancy formation energy for both the defects, as shown in **Figure 3c**. Furthermore, on a fully reduced ceria surface, three configurations of surface vacancies were identified: single surface or subsurface vacancies, vacancy dimers and vacancy trimers. The structural models of dimers and trimers of oxygen vacancies are summarized in **Figure 3d.** Superposition of single surface and subsurface vacancies results in the formation of a vacancy dimer. Double LSVCs form after the removal of another surface oxygen atom. Two possible variations of vacancy trimers, of which only the one that exposes Ce^{3+} ions (SVT 1 in **Figure 3d**), was observed.

Both surface and subsurface oxygen vacancies on a partially reduced (111) ceria surface were observed by several other researchers [29-31]. Oxygen vacancies are located at the third surface atomic layer. When the concentration of subsurface oxygen vacancies is very high, the defects form arrays with a propensity to form linear motifs [29]. The oxygen vacancies initially form triangular clusters and upon annealing form line defects. The clustering of oxygen vacancy defects on ceria surface is energetically more favorable than the formation of isolated surface oxygen vacancy defects [30].

2.1.2. Non-stoichiometric oxides of ceria and their structural properties

In reducing atmospheres (low oxygen pressures) and at elevated temperatures, ceria forms a continuum of oxygen deficient nonstoichiometric oxides with composition CeO_{2-x} where $0<x\leq0.5$ [32] as shown in **Eq. 2.3**. The actual reduction limit of nonstoichiometric ceria is Ce_2O_3 (i.e. when x = 0.5), where all cerium ions in the unit cell are in 3+ oxidation state.

$$CeO_2 \leftrightarrow CeO_{2-x} + \frac{x}{2}O_2(g) \qquad \textbf{(2.3)}$$

Different types of CeO_{2-x} oxide phases are identified in literature. However, some conflicting results exist on the structures and compositions of intermediate phases. The traditional powder x-ray diffraction (XRD) method has limitations in determining the structural characteristics of nonstoichiometric oxides [3]. Due to the low X-ray scattering power of O atoms, it is difficult to obtain the detailed sublattice structure of O from XRD technique [13]. So neutron and electron diffraction techniques have been employed to overcome the limitations of the XRD technique [33, 34].

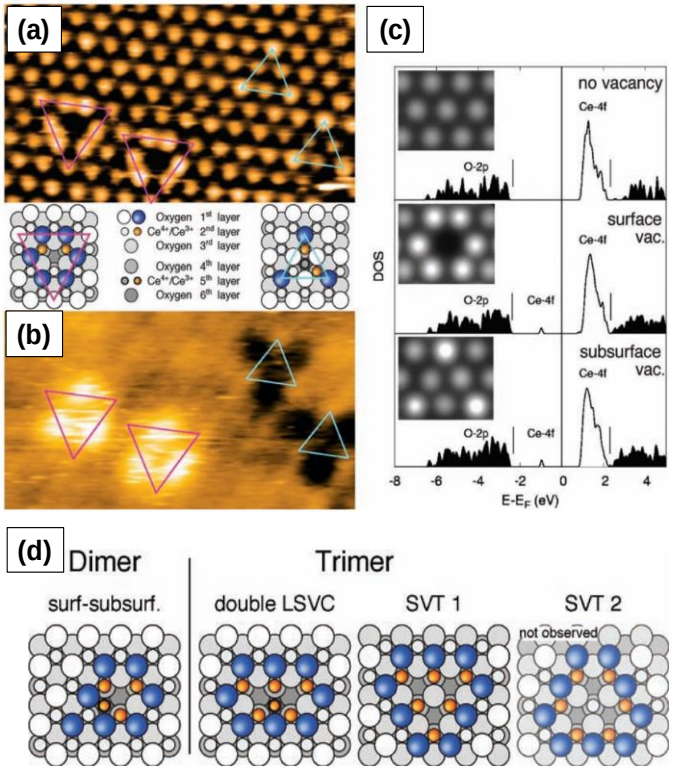

Figure 3. *STM images of surface and subsurface oxygen vacancies in (a) filled-state and (b) empty-state. Pink and blue triangles represent surface and subsurface vacancies, respectively. (c) Density of states (DOS) calculations along with STM images in filled-state (inset). Structures of the observed vacancy dimers and trimers. Reprinted with the permission from Ref [24].*

The so-called α phase non-stoichiometric oxides have compositions in the range of $0 < x < 0.286$ for CeO_{2-x} ($CeO_{1.714} - CeO_2$). The α phase shows a disordered nonstoichiometric fluorite-related structure that is stable at high temperatures (above 685 °C). XRD patterns obtained at high temperatures do not show superstructures and the lattice parameter of the cubic phase increases with x [34]. At lower temperatures however, the α phase transforms into a series of fluorite related phases described by the general formula Ce_nO_{2n-2m}. The lattice parameters at low temperatures are close to those reported for α phase although the α phase is disordered and low temperature phases show structural changes [35-37]. This implies that variation in oxygen partial pressure and temperature does not alter the positions of cerium ions and that the change in symmetry arising due to the reduction of ceria is primarily due to the formation of oxygen vacancies. Some examples of these phases are $Ce_{10}O_{18}$ (the ε phase), Ce_6O_{11} (the β phase, monoclinic) and $Ce_{11}O_{20}$ (the δ phase, triclinic) [37, 38].

The CeO_{2-x} oxides with the compositions $x>0.286$ at high temperature are dominated by the σ

phase, a nonstoichiometric phase with body-centered cubic crystal structure. The C-type sesquioxide (Ce_2O_3), end member of the σ phase, shows bixbyite crystal structure (space group I*a*3) [35]. The structures of CeO_2 and Ce_2O_3 are closely related in that their cerium ion arrays are almost identical and oxygen ions occupy tetrahedral positions in both cases. The oxygen ions occupy all available locations in the fluorite structure while only three-quarters are occupied in the bixbyite structure [19, 36]. As a result, the lattice parameter of Ce_2O_3 is almost twice that of CeO_2. The nonstoichiometric σ phase is very difficult to distinguish from the C-type sesquioxide.

2.2. Crystal plane and shape dependent properties

The reactivity of ceria-based materials is significantly affected by the morphology, oxidation states and the exposed crystal planes [39-41]. In this section, we will discuss the three thermodynamically stable low-index crystallographic planes of ceria namely (100), (110) and (111) [42-44] shown in **Figures 4a-c**. Some of the important characteristics of these three crystal planes are summarized in **Table 1**. Other ceria surfaces like (211), (210) and (310) are less stable and suffer severe reconstruction[40]. The (110) surface is a type 1 surface which exposes both cerium and oxygen ions and each layer has zero charge as the anions and cations are present in stoichiometric proportions in each plane (six coordinate cerium ions and three coordinate oxygen ions) [45, 46]. The (111) ceria surface is a type 2 surface which is terminated with oxygen ions. There is no net dipole moment as the three O-Ce-O layers (stacked one on top of the other) maintain charge neutrality. The coordination number is three and seven for oxygen and cerium, respectively [44]. The (100) surface of ceria is a type 3 surface which is intricate because an ideal surface could have either oxygen or cerium ions in the top surface thereby leading to a polar and unstable surface [46]. Oxygen and cerium have coordination numbers of two and six, respectively.

The structures and stabilities of the three low-index lattice planes of ceria have been extensively investigated by many researchers. Although the results vary, the stability generally follows the order (111) > (110) > (100) [27, 47]. Vacancies are the active sites for oxygen activation in oxidation reactions in many catalytic applications. (110) and (111) ceria surfaces have the lowest and highest vacancy formation energies, respectively. The (111) surface is less prone to accommodate a vacancy and hence energy needed for vacancy formation on its surface is the highest among the three [47]. The subsurface vacancy site is the most stable vacancy on the (111)

surface [48]. In (110) surface, the vacancy with one Ce^{3+} ion in both surface and first subsurface layers is determined to be the most stable. In (100) surface, two Ce^{3+} ions neighboring the vacancy site is the most stable; the next most stable site is 0.30 eV higher in energy [22]. In case of (110) and (100) ceria surfaces, for the same oxygen vacancy, more than one distribution of Ce^{3+} sites are observed.

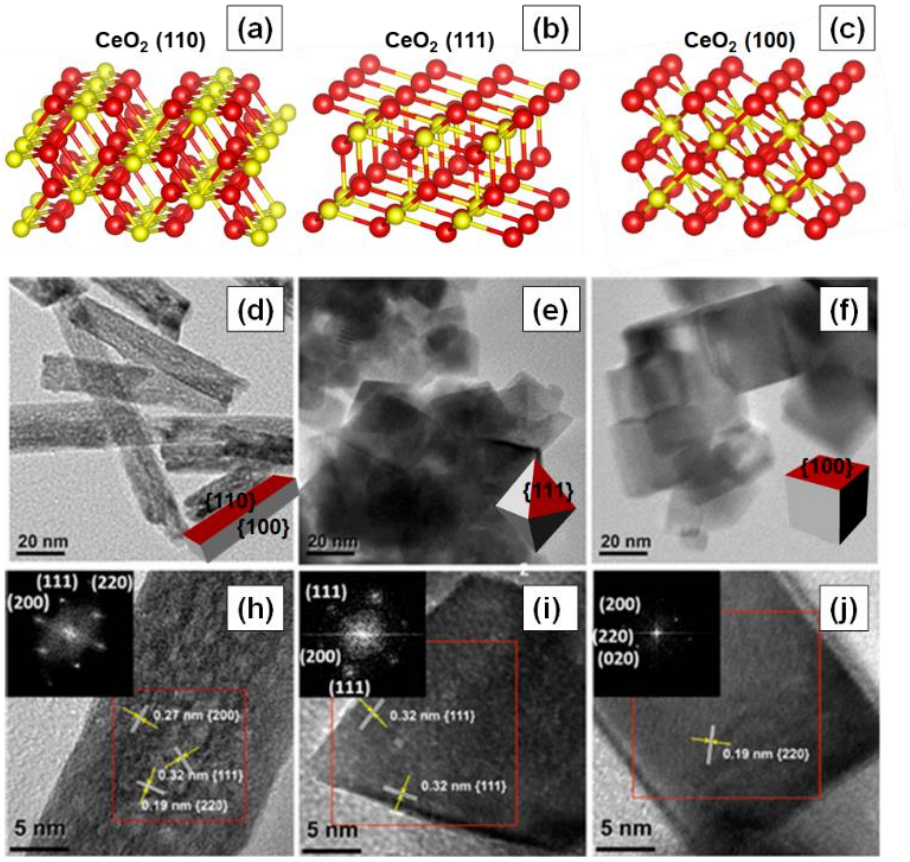

Figure 4*. Atomic structures of the three low index crystal planes of ceria. (a) 110 (b) 111 and (c) 100. Red and yellow colored spheres represent O^{2-} and Ce^{4+} ions, respectively. TEM and HRTEM images of the three different ceria nanoshapes (d, h) nanorods, (e, i) nanooctahedra and (f, j) nanocubes. Fourier transform patterns of selected areas of the samples are shown in the insets of HRTEM images. Figures 4d-j reprinted with permission from Ref [39]. Copyright 2018 American Chemical Society.*

The morphology and crystal plane of ceria can be affected by the synthesis method and the cerium precursor salt [49-53]. Ceria with well-defined lattice planes and morphologies can be obtained by modulating some of the critical synthesis parameters. Synthesis of ceria nanomaterials with different shapes like cube, octahedron, tetrahedron, sphere, rod and plate have been reported in literature. The most widely employed synthesis procedure to produce ceria in industrial

applications is by chemical precipitation, which results in the formation of NPs. Factors like pH, base concentration, reaction temperature and time affect the physicochemical properties of NPs including the shape and size [54-58]. Facet engineering can be used as a powerful tool to enhance modification of CeNPs, for example silanization through favorable adsorption of tetraethyl orthosilicate (TEOS) on the (100) facets and spontaneous breakage of the Si-O bonds of TEOS, as the rate determining step for silanization [59].

Table1. Properties (coordination number and oxygen vacancy formation energy) of low-index crystallographic planes of ceria

Property/*Crystallographic plane*	***(110)***	***(111)***	***(100)***
Coordination number	Ce(6) O(3)	Ce(7) O(3)	Ce(6) O(2)
Atom/s exposed by first layer	Ce and O	O	O
Relaxed surface energy (eV)	1.01	0.68	1.41
Unrelaxed surface energy (eV) (estimated from DFT calculations)	1.26	0.69	2.05
Oxygen vacancy formation energy (eV) (calculated from DFT corrected for on-site Coulomb interactions)	1.99	2.6	2.27

Among various other methods, hydrothermal process has been used to prepare different ceria nanoshapes. Mai and collaborators showed that ceria nanocubes, nanorods and nanopolyhedra can be selectively synthesized by varying the base concentration and temperature during hydrothermal synthesis. First, anisotropic $Ce(OH)_3$ nuclei form from the reaction of Ce^{3+} precursor ions with the base (NaOH). At low base concentration (0.01 mol/L) and temperature of 100 °C, the rate of dissolution/recrystallization is very low. Consequently, the driving force for the anisotropic growth of $Ce(OH)_3$ nuclei is also low and hence nanopolyhedra exposing (111) and (100) crystal planes are formed. At a much higher base concentration (6 mol/L) and 100 °C temperature, the dissolution/recrystallization rate is enhanced. $Ce(OH)_3$ nuclei grow anisotropically to form

nanorods exposing (110) and (100) surfaces. Increase in synthesis temperature to 180 °C led to the oxidation of $Ce(OH)_3$ to CeO_2 and nanocubes exposing (100) planes were formed. Besides NaOH, PO_4^{3-}, urea and H_2O_2 can also be used for hydrothermal synthesis of ceria nanomaterials [60-65].

Surfactant- or organic-assisted synthesis, with organic molecules used as coating agents, are often used to control the particle growth as the organic material adsorbs on specific planes of nanocrystals and directs the oriented growth. As mentioned above, the concentration of surfactant and cerium precursor salt, reaction temperature and time are some of the crucial factors that affect the morphology of ceria nanomaterials [66-70]. Pan et al. used a surfactant-assisted method to synthesize nanorods, nanoplates and nanotubes [52] using cetyltrimethylammonium bromide (CTAB). CTA^+ adsorbs on ceria nanocrystals and interacts with the (111) and (100) facets. The exposed surfaces couple to reduce the surface energy to form nanoplates. Due to the low coating ability at lower CTAB concentrations, nanoplates are transformed into nanorods to lower the surface energy by an anisotropic growth mechanism. At high CTAB concentrations, the nanoplates transform into nanotubes due to a rolling mechanism. Sometimes, combination of different organic molecules can also be used to selectively fabricate ceria nanomaterials with specific shapes. For example, addition of oleic acid (OA) as a co-surfactant to a solution of $Ce(NO_3)_3$ and diphenyl ether in oleylamine at 320 °C in sol-gel synthesis method led to the generation of nanowires and tadpole-shaped ceria nanocrystals due to anisotropic growth of nuclei [71].

Surfactants or surface coating agents play an important role in the synthesis, and later dictate the properties of the CeNPs. For instance, nanospheres were obtained by using diethylene glycol as the reaction solvent and polyvinylpyrrolidone (PVP) as the surfactant but when the synthesis was carried out in the absence of PVP, agglomerated and irregular shaped nanoparticles were obtained [72]. The charge of the surfactant can affect the morphology and the stability of ceria nanomaterials and should be considered. Anionic surfactants can adsorb on the positively charged ceria and effectively stabilize them while cationic surfactants repel away from cerium cations and result in agglomeration of nanocrystals. The ceria nanomaterials prepared by surfactant-assisted synthesis usually have good dispersibility and uniform size distribution. This technique can be employed to fabricate different shapes ceria which cannot be obtained using the conventional methods. Nonetheless, the use of organic solvents and surfactants can results in impurities and depending of the solvent and surfactant used can increase manufacturing costs. The effect of other synthesis methods on different ceria nanoshapes and the associated formation mechanisms are

presented in several comprehensive reviews and the readers can refer to them for additional information[73-75]. The anions of the cerium precursor salt can selectively interact with specific crystal planes and hence form nanocrystals with different morphologies. The Br^-, I^-, Cl^- and SO_4^{2-} counter anions of cerium precursor salt form nanorods whereas NO_3^- and BrO_3^- anions lead to the formation of nanocubes and NPs, respectively [50]. The anisotropic growth of $Ce(OH)_3$ nuclei formed by Br^-, I^-, Cl^- and SO_4^{2-} results in nanorods formation. In the presence of NO_3^- and BrO_3^-, CeO_2 nuclei are formed due to the oxidizing ability of these anions and the growth of isotropic CeO_2 nuclei results in the formation of nanocubes/NPs. $CeCl_3$ precursor salt exposes (100) and (110) planes due to the formation of nanorods while $Ce(NO_3)_3$ exposes (100) planes due to the formation of nanocubes [51].

The shape of nanoceria can also affect the concentration of oxygen vacancy defects and hence their reactivity. Numerous studies have indeed investigated the effect of shape on vacancy concentration and catalytic activity. For instance, Cao and collaborators studied the effect of shape or crystal plane on catalytic activity of ceria for CO oxidation[39]. Different morphologies, e.g. nanorods, nanooctahedra and nanocubes, with all having similar crystallite sizes were synthesized. The high-resolution transmission electron microscopy (HRTEM) images of the synthesized ceria nanoshapes are shown in **Figures 4d-j**. The ceria nanocubes and nanorods exposed (100) crystal plane while the nanooctahedra exposed (111) crystal plane. The concentration of Ce^{3+} ions, however, was similar in all three nanoshapes. Electron paramagnetic resonance (EPR) spectra suggested the presence of isolated vacancies on (100) facets of ceria nanorods and nanocubes and vacancy clusters on (111) facets of ceria octahedra. Furthermore, the type of oxygen vacancies and surface properties of ceria nanoshapes were correlated to their catalytic activity.

Ceria octahedra expose eight (111) planes while ceria cubes expose six (100) planes. Ceria nanorods expose (100) and (110) surfaces[76]. The reactivity of different facets, as determined by theoretical calculations, follows the order (110)>(100)>(111)[1, 77, 78]. This order, in fact, is in agreement with the experimental results on the activity of different crystal planes of ceria. Nevertheless, different vacancy formation energies in a given surface can be obtained, which is due to some of the limitations of techniques used for theoretical calculations, discussed in detail elsewhere[1, 44].

2.3. Size impact on the reactivity and catalytic activity properties

Particle size has a significant impact on the reactivity and catalytic activity of ceria nanomaterials. The effect of particle size was first experimentally probed by Tsunekawa's group. In a series of publications, they showed that the lattice parameter (calculated from electron diffraction patterns) increases with the decrease in the particle size from 6.7 to 2.1 nm[18, 19]. Three possible models were proposed to explain the increase in lattice parameter value based on the fact that oxygen forms peroxide, O_2^{2-}, and superoxide, O_2^{-}, on the surface of reduced CeO_2. One model suggests that the CeNPs consist of a layer of Ce_2O_3 with an estimated thickness of 0.561 nm on the outside while the core is CeO_2. Several studies also observed size-induced lattice expansion in CeNPs particularly for sizes below 20 nm due to increase in the oxygen vacancies and Ce^{3+}.

Wu et al. determined the concentration of Ce^{3+} as a function of particle size using electron energy loss spectroscopy (EELS)[79]. The fraction of Ce^{3+} ions rapidly increased with decreasing particle size below 15 nm. Interestingly, their EELS spectra revealed completely reduced ceria, Ce_2O_3, at a diameter of 3 nm. This reduced ceria was found to have a fluorite structure like that of bulk CeO_2. Also, EELS spectra acquired from the edge and the center of the particles showed that, for larger particles, the reduction of Ce^{4+} to Ce^{3+} happens mainly at the surface, resulting in a Ce_2O_3 surface layer but leaving the core as CeO_2. Hailstone and collaborators studied the size-dependent lattice expansion of colloidal ceria NPs using TEM[80]. The lattice constant increased with a decrease in particle size, with 1.1 and 11.8 nm particles having values of 0.578 and 0.547 nm, respectively. The corresponding lattice expansion was found to be about 6.8% and 1.1% for 1.1 and 11.8 nm CeNPs, respectively. The diffraction patterns for all the three different sized particles were found to be consistent with that of the fluorite crystal structure of CeO_2 and not with the predicted cubic or the hexagonal structure of Ce_2O_3. Most of the surface ions were Ce^{3+} and correspondingly there were substantial oxygen vacancies. The larger radius of Ce^{3+} along with the associated oxygen vacancies corroborate the higher lattice constant and hence the greater lattice expansion observed for smaller particles.

As the size of ceria NP decreases, more and more oxygen vacancies are formed and hence the concentration of Ce^{3+} increases as shown in **Figure 5a**. Since Ce^{3+} ions have a larger ionic radius than Ce^{4+} ions, the particle size reduction leads to lattice distortion and introduces strain in the lattice. This strain is liberated after lattice expansion and therefore the lattice parameter increases (**Figure 5a**)[16, 17, 19 4,6,8]. Xu et al. studied the size-dependent structural, chemical and electronic properties of ceria[81]. The lattice parameter increased with the decrease in particle size as shown in

Figure 5b, but their results did not provide any proof for increase in Ce^{3+} concentration and oxygen vacancies. Nonetheless, a dramatic increase in the concentration of reducible oxygen was observed at sizes below 5 nm due to peroxide formation on ceria surface. It is now established that the CeNP size influences the degree of hydroxylation and hydroxyl stability, with particles <5 nm having a higher density of more thermally stable hydroxyl groups as compared to larger particles [82]. These functional groups dictate the surface reactions and the behavior of the CeNPs in aqueous environments, which is relevant for many processes, e.g. pro- or anti-oxidant activity, surface sorption. This also suggests that, beyond the varying Ce^{3+}/Ce^{4+} ratios, the surface hydroxyl groups also play a critical role to the CeNP reactivity.

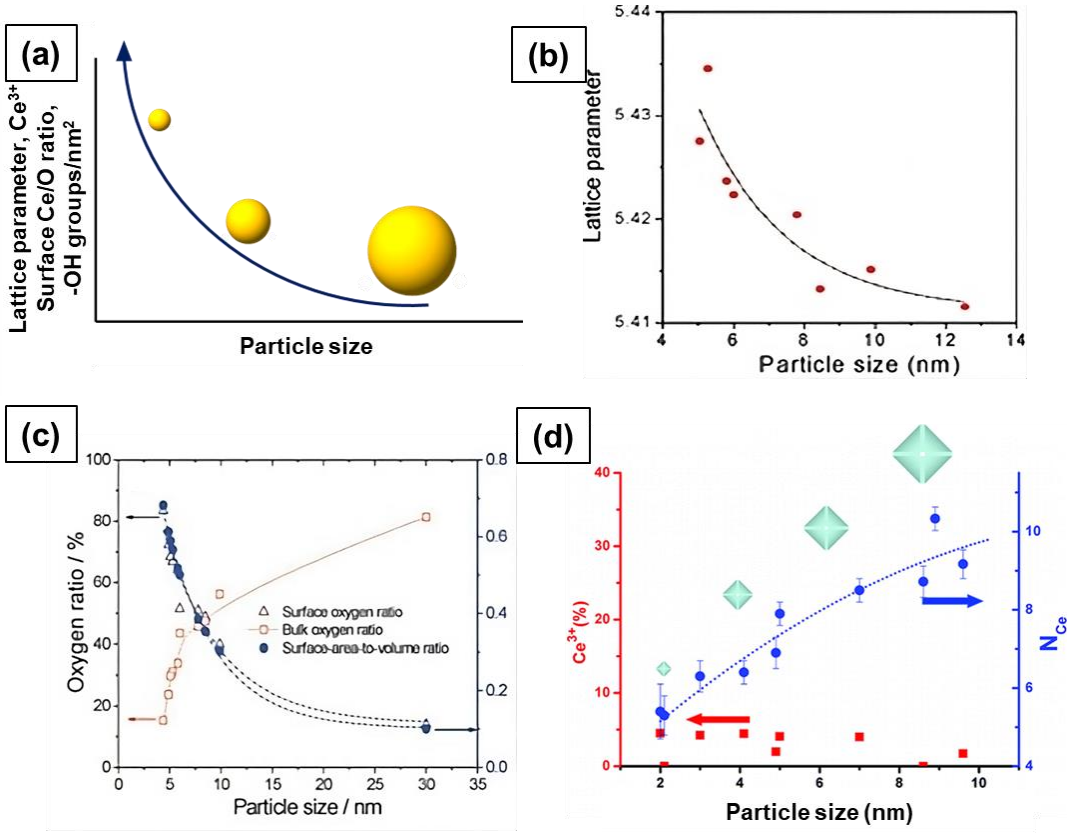

Figure 5. *(a) Effect of particle size on lattice parameter, concentration of Ce^{3+}, oxygen vacancies and hydroxyl species. More and more oxygen vacancies form with decrease in size and this leads to an increase in the concentration of Ce^{3+} ions and lattice parameter. (b) Increase in lattice parameter with the decrease in size and (c) The concentration of surface oxygen and bulk oxygen as a function of particle size and (d) Concentration of Ce^{3+} and Ce-Ce coordination as a function of particle size. Figures 5b and c reproduced from Ref [81] with permission from the Royal Society of Chemistry. Figure 5d reprinted with permission from Ref [83].Copyright 2012 American Chemical Society.*

The surface oxygen concentration varies inversely with the bulk oxygen concentration as a function of particle size as shown in **Figure 5c**. The concentration of surface oxygen increases at the expense of the concentration of bulk oxygen. It is likely that the significant increase in the concentration of reducible/surface oxygen is due to the increased Ce^{3+} concentration as Ce^{3+} ions interact with O_2 and form cerium superoxide ($Ce^{4+}O_2^-$). A decrease in particle size leads to increased Ce^{3+} species and hence a higher concentration of $Ce^{4+}O_2^-$ species. The formation of cerium superoxide ($Ce^{4+}O_2^-$) and cerium peroxide ($Ce^{3+}O_2^{2-}$) species will be discussed in section **2.6**. The size-dependent lattice parameter and relative Ce^{3+} concentration values of ceria particles reported by several published studies are summarized in **Table 2**.

Table 2. Size-dependent relative Ce^{3+} concentration and lattice parameter values of ceria particles from different studies.

Particle size range (nm)	**[Ce^{3+}] range (%)**	**Preparation method**	**Lattice parameter range (nm)**	**Ref.**
2-7	17.3-42.5	Hydrothermal	0.5453 - 0.5560	[18, 19]
4-60	---	Precipitation (semi-batch reactor)	0.5401 - 0.5419	[84]
3-20	---	Thermal evaporation	0.5402 - 0.5615	[79]
6-15	---	Precipitation	0.5413 - 0.5433	[85]
1-12	---	Precipitation	0.547 - 0.578	[80]
4-10	29.4-29.5	Microemulsion	0.5415-0.5435	[81]
3-30	17-44	Precipitation	0.548 - 0.560	[17]
10-90	15-26.3	Precipitation	---	[86]
10-235	19.3-27.6	Supercritical solvothermal	0.5406-0.5425	[87]
~10	34	Green synthesis	---	[88]
Bulk	---	---	0.5403	[89]

In some studies, some very low Ce^{3+} concentrations have been reported for CeNPs particles,

contradictory to majority of the published reports. For instance, Vayssilov et al. showed that 2 nm ceria particles prepared by thermal evaporation contained only 2% Ce^{3+} [90]. Using x-ray absorption near edge structure spectroscopy (XANES), Nachimuthu et al. estimated that the concentration of Ce^{3+} ions was very low (<5%) even for 2 nm ceria particles[91]. Paun et al. studied size-dependent properties of ceria particles using TEM, XRD, X-ray spectroscopy (XPS), extended x-ray absorption fine structure (EXAFS) and XANES[83]. These analyses revealed that the Ce^{3+} concentration does not vary with size under ambient conditions although the lattice parameter increases with the decrease in particle size. As can be seen in **Figure 5d**, the Ce^{3+} concentration remained at the same ~4% value with the decrease in particle size from 8 nm to 2 nm. This value of 4% is way lower than that reported in other studies which are in the range of 20-30% for about the same particle size. The presence of Ce^{3+} ions in traces was attributed to the use of Ce^{3+} precursors used for synthesis.

While most studies reported lattice expansion in the range of 0.1-0.5% for particles smaller than 5 nm, Tsunekawa et al. [19] and Wu et al. [79] observed lattice expansion in the range of 2-3.5% for similar particle sizes. Hailstone and collaborators reported a very high lattice expansion of 7% for 1 nm CeNPs[80]. These dramatic differences in lattice expansion is potentially attributed to the effect of surface stabilizers used in the synthesis to control the particle growth. Another aspect that is worth highlighting is the relative Ce^{3+} concentration. Majority of the studies reported Ce^{3+} concentrations greater than 15% for particles smaller than 5 nm. Nevertheless a few studies reported very low (<5%) relative Ce^{3+} concentration values for particles smaller than 5 nm. These apparent differences could be due to variations in preparation method, synthesis conditions, surface coating agents, or the characterization method employed to estimate Ce^{3+} concentration. A thorough knowledge of the particle synthesis chemistry is necessary to understand the effect of synthesis method on Ce^{3+} concentration. In this regard, it is critical to create standards for the synthesis method and the determination of relative Ce^{3+} concentration.

The size-dependent oxygen vacancy formation energies in $(CeO_2)_n$ with n values in the range of 20-140 was investigated using DFT calculations[92-94]. The removal of a low-coordinate O atom from ceria needs the least energy, consistent with the results reported for other metal oxides. The removal of such O atoms from nanosized particles is more favored than from the extended surfaces. The increase of particle size is associated with a marked decrease in the oxygen vacancy formation energy, indicating that this energy reaches a minimum at certain sizes. The size dependence of the

oxygen vacancy formation energy is controlled by electrostatics. The bandwidth of the unoccupied density of states projected on to the cerium 4f orbital levels is a crucial factor that affects energy of vacancy formation. Presence of corner cerium atoms is identified as the structural pattern necessary for a significant reduction of vacancy formation energy.

By summarizing these results, the following conclusions can be drawn. (1) With a decrease in particle size, more and more oxygen vacancies are formed and, consequently, the Ce^{3+} concentration is enhanced. (2) An increase in Ce^{3+} concentration increases the lattice parameter due to the lattice expansion as Ce^{3+} ions have higher ionic radius than Ce^{4+} ions. (3) Most of these changes (formation of oxygen vacancies and generation of Ce^{3+} ions) occur on the surface. As a result, the surface is very similar to that of Ce_2O_3 while the bulk remains as CeO_2. When the particle size decreases to about a nanometer or two, the particle transforms from CeO_2 to Ce_2O_3 as showed by several studies and the particle mostly consists of Ce^{3+} ions. The conversion from CeO_2 to Ce_2O_3 C-type sesquioxide does not require a change in the crystal structure. Hence, in some studies, even ~1-2 nm particles showed fluorite structure as the C-type is a combination of three types of fluorite like unit cells. (4) The oxygen vacancy formation is thermodynamically more favorable on CeNP' surfaces than in the bulk. (5) The corresponding formation energies of the Ce^{3+} ions are also lower on the nanoceria surfaces than in the bulk. Clearly, these findings suggest that the concentration of surface Ce^{3+} ions, the surface functional groups and the associated oxygen vacancies and, hence, the reactivity of NPs increases with a decrease in particle size while the oxygen vacancy formation energy diminishes markedly.

2.4. Modification by doping

Due to the increased surface area to volume ratio and relative ease of vacancy defect formation, CeNPs show enhanced reactivity and outstanding catalytic activities enabling their use in many commercial applications. However, pure CeNPs are associated with some drawbacks like deactivation of OSC and catalytic activity, and a loss of surface reactivity due to thermal sintering at high temperatures which limit their use in some commercial applications[95, 96]. It is therefore of interest to modify the properties of CeNPs, and alter the surface energies, to facilitate their use in such applications. Any chemical modification or doping of CeNPs involving an increase in the concentration of oxygen vacancies should in principle increase their reactivity. This is true only if

(a) the chemical modification process does not lead to a significant reduction in the concentration of active redox species and (b) the defects formed at high degrees of reduction do not cluster, making ion transport difficult.

One of the important strategies to overcome these limitations is to incorporate other metal ions into the crystal structure of CeNPs by doping. Addition of dopants results in higher resistance to sintering at elevated temperatures and an enhancement of reducibility and OSC of CeNPs and therefore improves the overall catalytic performance[97, 98]. The concept of modifying CeNPs by doping with foreign materials indeed led to enhanced thermal stability and improved catalytic activity. In a typical doping process, cerium atoms in the crystal lattice are replaced with noble metals, transition metals or rare earth metals.

Doping is done during synthesis and the dopants substitute Ce^{4+}. The result is that oxygen vacancies are introduced in the crystal structure of ceria for charge compensation[99] as shown in **Figure 6a**. Doped CeNPs show very high oxygen mobility through a vacancy diffusion mechanism and hence high ionic conductivity[100, 101]. Given the importance of oxygen vacancy defects of CeNPs in many applications, this topic has garnered a lot of attention. Most reported works explored the use of rare earth (Y^{3+}, Gd^{3+}, Sc^{3+}, Sm^{3+}, Er^{3+}, Eu^{3+}, La^{3+}, etc.), noble (Pt, Pd, Au, and Rh) and transition metals (Cu, Co, Ni, Mn, Zr, Zn, Fe, etc.) as dopant materials to modify the physicochemical properties of CeNPs (**Figure 6b**). The dopants are further categorized into two types, isovalent and aliovalent, based on their oxidation state[102, 103]. Isovalent dopants are the ones that have a 4+ oxidation state (same as that of the host Ce^{4+}) and aliovalent dopants have an oxidation state that is different from that of the host. Substitution of Ce^{4+} with the isovalent dopants in the crystal lattice of ceria introduces intrinsic oxygen vacancies and reduces the oxygen vacancy formation energy because of structural distortion [72]. On the other hand, substitution with aliovalent dopants incorporates both extrinsic and intrinsic defects and reduces vacancy formation energy due to structural distortion and electronic modifications.

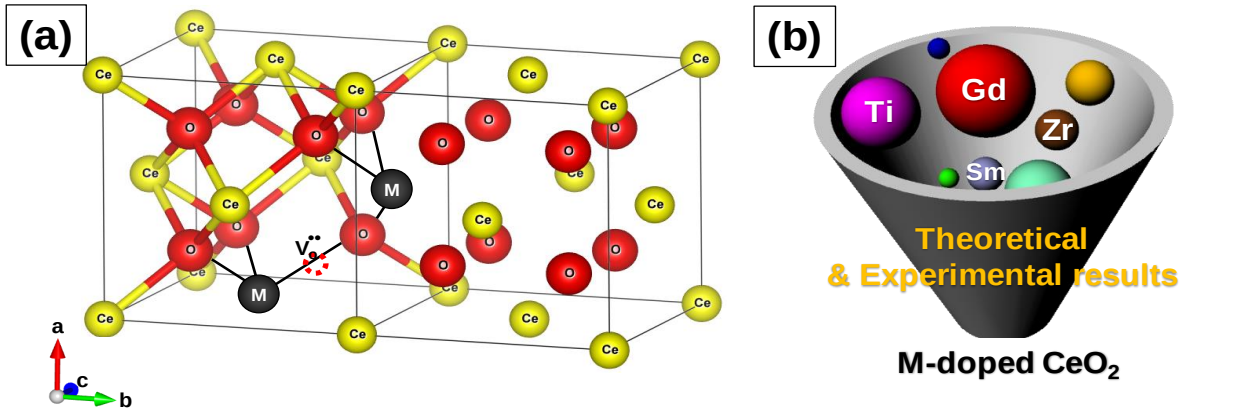

Figure 6. *(a) Schematic of the crystal structure of ceria with metal ion dopant M. Addition of dopants (rare earth, transition or noble metal ions) during synthesis results in the formation of oxygen vacancies. (b) Development strategy for ceria with metal ion dopant M.*

2.4.1. Doping with rare-earth metals

Rare earth doped CeNPs are attractive candidates for many industrial oxidation reactions, biomedical and biosensing applications and electrodes in solid oxide fuel cells (SOFCs). The introduction of oxygen vacancies upon doping ceria with rare-earth ions can be represented as follows in Kröger-Vink defect notation (**Eq. 2.4**)

$$Re_2O_3 + 2Ce_{Ce}^{x} + O_O^{x} \longrightarrow V_o^{\cdot\cdot} + 2Re_{Ce}^{\prime} + 2CeO_2 \qquad (2.4)$$

Where $Re_{Ce}^{\prime}$ represents a Re^{3+} ion on a Ce lattice site.

Increase in the concentration of Gd from 0 to 15% increased the OSC of CeNPs but with a further increase, the OSC decreased [104]. The enhanced OSC was attributed to the increased specific surface area and decreased particle size. In contrast, Hennings et al. reported that the OSC decreased after with Gd[105]. Nevertheless, the concentration of oxygen vacancies increased with the increase in Gd concentration. They argued that the drop in OSC was due to the replacement of reducible Ce^{4+} by non-reducible Gd^{3+} and suppressed reduction of Ce^{4+}. Trivalent La, Sm, Y and Gd increase the concentration of Ce^{3+} ions on the surface of particles[106]. Increase in Ce^{3+} concentration enhances oxygen vacancies and facilitates transport of oxygen from the bulk to the surface. La and Pr doping boosted the concentration of surface reducible Ce^{4+} ions and shifted the reduction peak of CeNPs to lower temperatures[107]. It is important to point out that the optimal concentration of dopant required to obtain maximum increase in the concentration of Ce^{3+} and oxygen vacancies depends upon the type of the dopant. For instance, in one study, it was shown that the optimal concentration of La and Pr was about 5% and 50%, respectively[108].

Of all RE elements, Pr yields the maximum concentration of oxygen vacancies. In case of Pr doping, the presence of both Ce^{3+} and Pr^{3+} ions increased the concentration of oxygen vacancies due to the reduction of Pr^{4+} to Pr^{3+} and Ce^{4+} to Ce^{3+} [107]. Of Nd- and La-doped CeNPs prepared using microemulsion method, the oxygen vacancy defect concentration was higher for La-doped ceria than for Nd-doped ceria and this difference was attributed to the larger ionic radius of La as compared to Nd[109]. Y, Sm and Gd doping increased the Ce^{3+} and oxygen vacancy defect concentration while Yb doping reduced it due to the smaller ionic radius of Yb^{3+} as compared to that of the other three ions[110]. Er and Ho also decreased the density of oxygen vacancies due to a similar reason[111]. Using DFT calculations, Kim et al. established a trend between the radius of the RE metal ion and oxygen vacancy formation energy, which is related to the catalytic activity[112]. The relationship between the oxygen vacancy formation energy and the ionic radius of RE metal, and the highest reaction energy and ionic radius of RE metal ion **(Figures 7a** and **7b**) showed an increase in the vacancy formation energy with the ionic radius whereas the maximum reaction energy (for the case of CO oxidation considered as an example) decreases with the ionic radius. The contribution of the dopant to oxygen vacancy formation energy was also investigated. The ionic radius of the dopant (R_{ion}) was also found to influence the RE-O interaction which in turn altered the oxygen vacancy formation energy (E_{vf}), by measuring how easily oxygen vacancies are formed. While most research suggests that doping CeNPs with RE elements typically results in expansion, the radius and coordination number of the dopant ion also play an important role and can lead to variations in RE-O bonds length and different E_{vf}. The charge density distribution between RE-O was studied by calculating the RE-O bond strength. The charge of cerium ion in pure CeO_2 is 4+ and the ionic radius of Ce^{4+} is 114.3 pm. In contrast, the charge of the other RE elements in CeO_2 is 3+ and the ionic radius of the RE ion is relatively smaller than that of Ce^{4+} with La being an exception. As a result, structural stress is induced along RE-O. The stress created by the dopant ion having a smaller ionic radius weakens the strength of the RE-O as shown in **Figure 7c**. Therefore, dopants having a lower ionic radius lead to a lower E_{vf}.

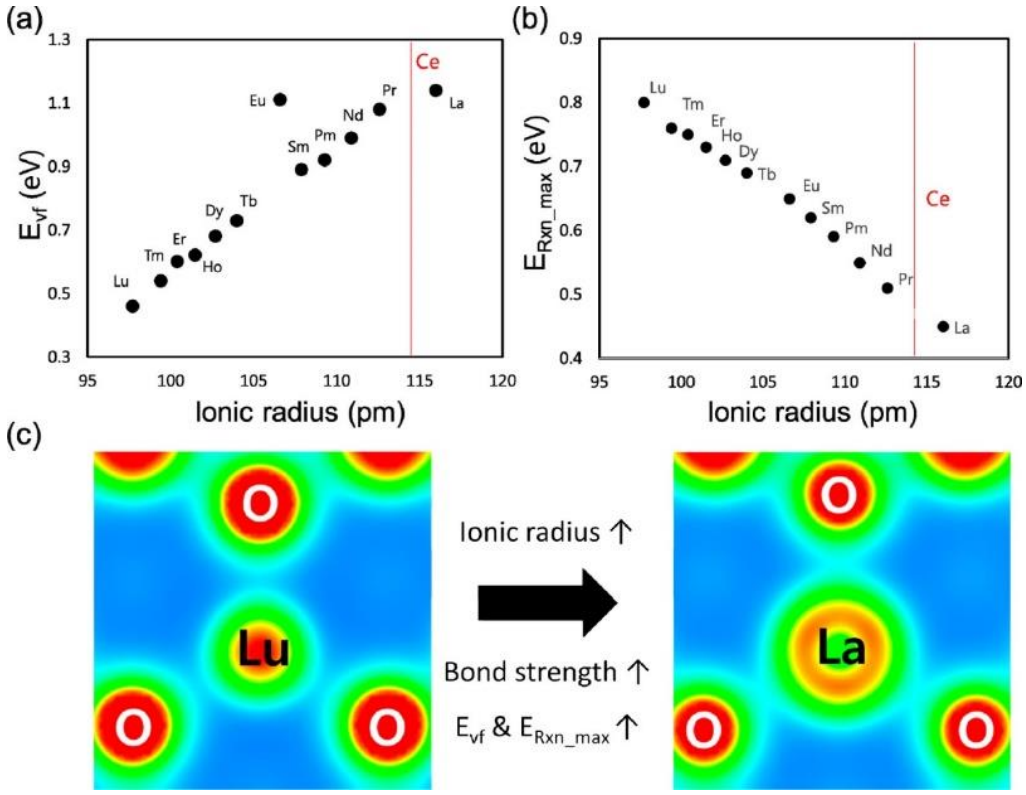

Figure 7. *Relationship between (a) oxygen vacancy formation energy and radius of RE ion and (b) maximum reaction energy and radius of RE ion. (c) Charge density distribution in RE ion having largest ionic radius (La) and with smallest ionic radius (Lu) bonded with O atoms in RE doped ceria. Reprinted from permission from Ref [112]. Copyright 2017 American Chemical Society.*

Because lanthanide complexes have excellent luminescence, these structures can be widely used in biosensing and bioimaging applications[113, 114]. CeNPs show weak emission characteristics that restrict their use in fluorescence-based imaging and sensing. Europium (Eu), one of the rare earth metals has a strong red light emission upon doping and is considered a suitable dopant to enhance emission in CeNPs as the ionic radius of Eu^{3+} ion (0.1066 Å) is higher than that of Ce^{4+} (0.097 Å) but lower than that of Ce^{3+} (0.1143 Å) and shows excitation from ultraviolet to visible region[115]. Therefore, Eu doping intensifies the photoluminescence properties of CeNPs, opening up many possible opportunities for applications in molecular imaging. The appearance of a broad band in the excitation spectrum of Eu doped CeNPs is due to the charge-transfer from O^{2-} to Ce^{4+} [116]. Both Ce^{3+} and oxygen vacancy concentration increase with an increase in Eu concentration. Conflicting roles of Ce^{3+} ions and oxygen vacancy defects in influencing the photoluminescence response of doped CeNPs have been reported. Kumar et al. found that the increase in Ce^{3+} concentration enhanced the photoluminescence properties whereas an increase in vacancy defect

concentration adversely affected the photoluminescence by interfering with the radiative route of emission[117]. Erbium (Er) is another rare-earth element that has been used by several investigators as a dopant to impart fluorescence in ceria particles[118, 119].

Not all trivalent rare-earth metals increase the concentration of Ce^{3+} and of oxygen vacancies. An important question that then needs to be answered is – what cations can be used for doping ceria particles? Several studies suggested that dopants having ionic radii lesser than that of Ce^{4+} ion can be doped into ceria lattice. However, this is not always the case as evidenced from many contradictory results reported in literature.[2, 120] When the dopant substitutes a Ce^{4+} ion in the crystal lattice of ceria, the periodic electrostatic field distribution changes due to different electronegativity, oxidation state and ionic radius of the dopant with respect to the Ce ion. The thermodynamics (enthalpy) of dopant incorporation and other thermodynamically relevant factors can potentially be helpful in identifying the right dopant. Computational techniques can also provide some guidance in understanding the thermodynamics of dopant addition to ceria lattice.

2.4.2. Doping with transition and noble metals

Apart from rare earth metals, transition and noble metals were also used to dope CeNPs to enhance their catalytic properties. CeNPs doped with transition metals like Co, Zr, Cu, Fe, Mn, Cr, etc. have good redox ability and can therefore act as active materials for oxidation reactions. The reactivity of these ceria-mixed materials is influenced by various factors like valency of the dopant, catalyst composition, nature and type of the support, as well as the synthesis technique, particle size and shape and crystal structure.

Among composite structures, zirconia doped ceria (ceria-zirconia) has been studied intensively due to its significance in various industrial catalytic reactions. Ceria forms a substitutional type solid solution with zirconia. When CeNPs are doped with zirconia, the smaller Zr^{4+} ion causes lattice distortion, leading to an increase in oxygen mobility. After introducing Zr^{4+} ions into the crystal lattice of ceria, both Ce-O-Zr and Ce-O-Ce bond lengths in $Ce_xZr_{1-x}O_2$ lattice decrease and oxygen shows a centro-symmetric eight-fold coordination[121]. This change in the local environment of oxygen around Ce^{4+} and Zr^{4+} cations leads to the formation of active oxygen species that plays an important role in the OSC property, and therefore its catalytic activity. The reduction of ceria in ceria–zirconia solid solutions can be described by the following chemical reaction:

$$Ce_xZr_{1-x}O_2 + H_2 \leftrightarrow Ce_xZr_{1-x}O_{2-\delta} + H_2O + V_o \quad (\mathbf{2.5})$$

The oxygen nonstoichiometric (δ) value in the above equation changes with composition x. The enhanced reducibility is due to the improved oxygen mobility of solid solutions as compared to the pure oxides. The high concentration of oxygen vacancy defects increases the active sites for ionic conduction and provides a high diffusion path through the nanosized grain boundaries that promote fast kinetics[122, 123]. Introduction of Zr^{4+} ions in the fluorite crystal structure of ceria decreases the specific surface area at the operating conditions. Nonetheless, the increased thermal resistance to sintering, decreased oxidation enthalpies, higher reduction efficiency and increased OSC of zirconia doped ceria contribute to the enhanced performance of ceria-zirconia system in designing a new generation of three-way catalytic converters (TWCs)[124].

Ceria-zirconia catalysts have gradually replaced pure ceria whose properties did not meet the requirements of high conversion efficiency and thermal resistance needed to sustain stringent emission regulations. Additionally, a critical need for more thermally stable materials to improve performance of TWCs during cold start led to the development of several strategies. Among them, doping of ceria-zirconia with rare earth elements like La, Pr, Y, Sm and Nd resulted in an increased thermal stability and OSC[125]. The cerium precursor salt was found to have a significant influence on the catalytic properties. The ceria-zirconia catalysts prepared using cerium salt having +4 oxidation state, $(NH_4)_2Ce(NO_3)_6$, was found to have higher Ce^{3+} concentration than those prepared using cerium salt having +3 oxidation state $Ce(NO_3)_3{\cdot}6H_2O$[126]. Also, the catalysts prepared with Ce^{4+} precursor salt had higher Zr concentration and showed improved oxygen mobility than those prepared by Ce^{3+} precursor. The catalytic activity of ceria-zirconia catalysts is dependent on both the BET surface area and Ce/Zr surface atomic ratio. The Ce/Zr value in turn depends on the synthesis technique and therefore the catalytic activity strongly depends on the preparation method. Thus, the BET surface area of the catalyst prepared using $Ce(NO_3)_3{\cdot}6H_2O$ was higher than that prepared using $(NH_4)_2Ce(NO_3)_6$; the latter showed higher catalytic activity which was attributed to the higher Zr concentration on its surface.

In other reports, the addition of Cu to the ceria lattice increased its OSC and redox properties by reducing the activation energy for Ce^{4+} reduction as showed by Hu et. al.,[127, 128]. Their results showed that the Cu/Ce ratio in the catalyst strongly influenced the catalytic and redox properties. The pore structure and morphology of Cu-doped ceria NPs can be affected by the precursor used for synthesis. $CuCeO_x$ nanofiber catalysts prepared by electrospinning technique showed higher catalytic activities as compared to those prepared by other conventional methods[129]. The enhanced

catalytic activity of nanofibers was ascribed to the large specific surface area and increased concentration of Ce^{3+} ions and oxygen vacancy defects. Doping of CeNPs with Cu also increased the overall surface area and improved the redox properties.

Mn doping into ceria lattice has also showed to increase the concentration of oxygen vacancy defects. XPS analysis of the surface indicated that the Ce is present in +4 or +3 oxidation states while Mn exists in +3 or +2 oxidation state[130]. EPR analysis indicated the presence of Mn^{2+} and Mn^{3+} species in defect sites of ceria lattice, interstitial spots and on the surface of ceria. Doping with Mn decreased the particle size of calcined CeNP powders and dramatically increased the BET surface area[131]. Impedance spectroscopy measurements have revealed that the Mn ions enter into solid solution and increased the conductivity by decreasing the apparent activation energy. DRIFTS results showed that a fraction of Mn ions remain segregated on particle surface. The remarkable enhancement in catalytic activity of Mn doped ceria at low temperature is ascribed to good dispersion of Mn^{2+}/Mn^{3+} ions in the ceria matrix, high OSC, increased redox properties and synergistic interaction between the Mn and Ce. Among co-precipitation (CP), sol-gel (SG) and hydrothermal methods used to prepare Mn-doped ceria, the catalyst synthesized by HT method showed very high catalytic activity at low temperature[131]. The larger surface area, increased reducibility, higher concentration of surface adsorbed active oxygen species and an increased number of oxygen vacancy sites are the possible reasons for the enhanced catalytic activity of the mixed catalyst prepared by hydrothermal method.

In other structures, the presence of Ni^{3+} ions and a very high concentration of oxygen vacancy defect sites in Ni-doped ceria NPs ($Ni_{0.1}Ce_{0.9}O_{2-x}$) has showed an increase in the surface reducibility of these doped structures as compared to pure ceria[132]. Ni-doped ceria showed superior electrochemical properties due to increased concentration of Ce^{3+}, Ni^{3+} and oxygen vacancy defects used to boost Faradaic surface redox reactions[133]. Doping with Ni leads to additional structural stress and lattice expansion and extrinsic defects on the particle surface and near grain boundaries. It also results in enhanced surface oxygen reactivity and thus more active reduction sites at their surface. Other reports explored the use of Co to increase catalytic properties of CeO_2 and found enhanced performance of Co–CeO_2 catalyst as compared to that of bulk Co_3O_4 or ceria due to a synergetic effect between Co and CeO_2, leading to increased concentration of oxygen vacancy defects and enhanced reducibility[134]. The preferential exposure of (112) crystal plane of Co-CeO_2 which contained a large concentration of Co^{3+} active sites was also suggested

to be responsible for the higher catalytic activity. The increase in cobalt dopant concentration also increased the band gap energy and reducibility of the catalyst[135].

Fe doping of ceria enhanced the catalytic activity due to the increased concentration of surface Ce^{3+} and chemisorbed reactive oxygen species[136]. Addition of iron into the crystal lattice of ceria decreased the crystallite size and increased the specific surface area[137]. Fe-doped ceria favors sintering at lower temperatures, enhances the reducibility and increases the number and strength of basic sites[138]. Doping of ceria with iron can also improve the conductivity, decrease the activation energy and enhance the dynamic oxygen storage capacity (DOSC). Therefore, the Fe-doped ceria catalyst showed low temperature activity and increased total oxygen storage capacity (TOSC). It was suggested that the incorporation of Fe into the crystal lattice of ceria strongly modifies the kinetics of oxygen diffusion and enhances the OSC.

Ag, Au, Pt and Pd doping are other suitable approaches to enhance the catalytic activity of CeNPs. The addition of Ag favors the formation of reducible oxygen species that is suggested to be responsible for the improved catalytic activity[139]. The synergistic interaction between Ag and ceria is the key for low temperature reduction of ceria[140]. Three different methods used to prepare Pt-doped ceria catalyst resulted in different values of ionic Pt/Pt^0 ratios[141]. Furthermore, these three different catalysts were found to achieve varying catalytic activities, increasing with the increasing concentration of ionic Pt species. DFT calculations suggested that the presence of ionic Pt species activated the oxygen atoms on the cerium next to it resulting in decreased activation energy for dissociative methane adsorption. As a result, the novel square-planar configuration of PdO_4 in Pd-doped ceria is shown to be more reactive[142]. Creation of an oxygen vacancy in this structure is energetically more favorable. The structural and chemical attributes of Pd-O-Ce moieties were found to contribute to the higher catalytic activity of Pd-doped ceria [143]. All Ce ions in the crystal are in 4+ oxidation and they are not reduced to 3+ state upon formation of oxygen vacancies as evident from the density of electron states where the filled Ce4f gap states associated with the reduced ceria are not present. The physicochemical properties of rare earth, transition and noble metal doped ceria particles are summarized in **Figure 8.**

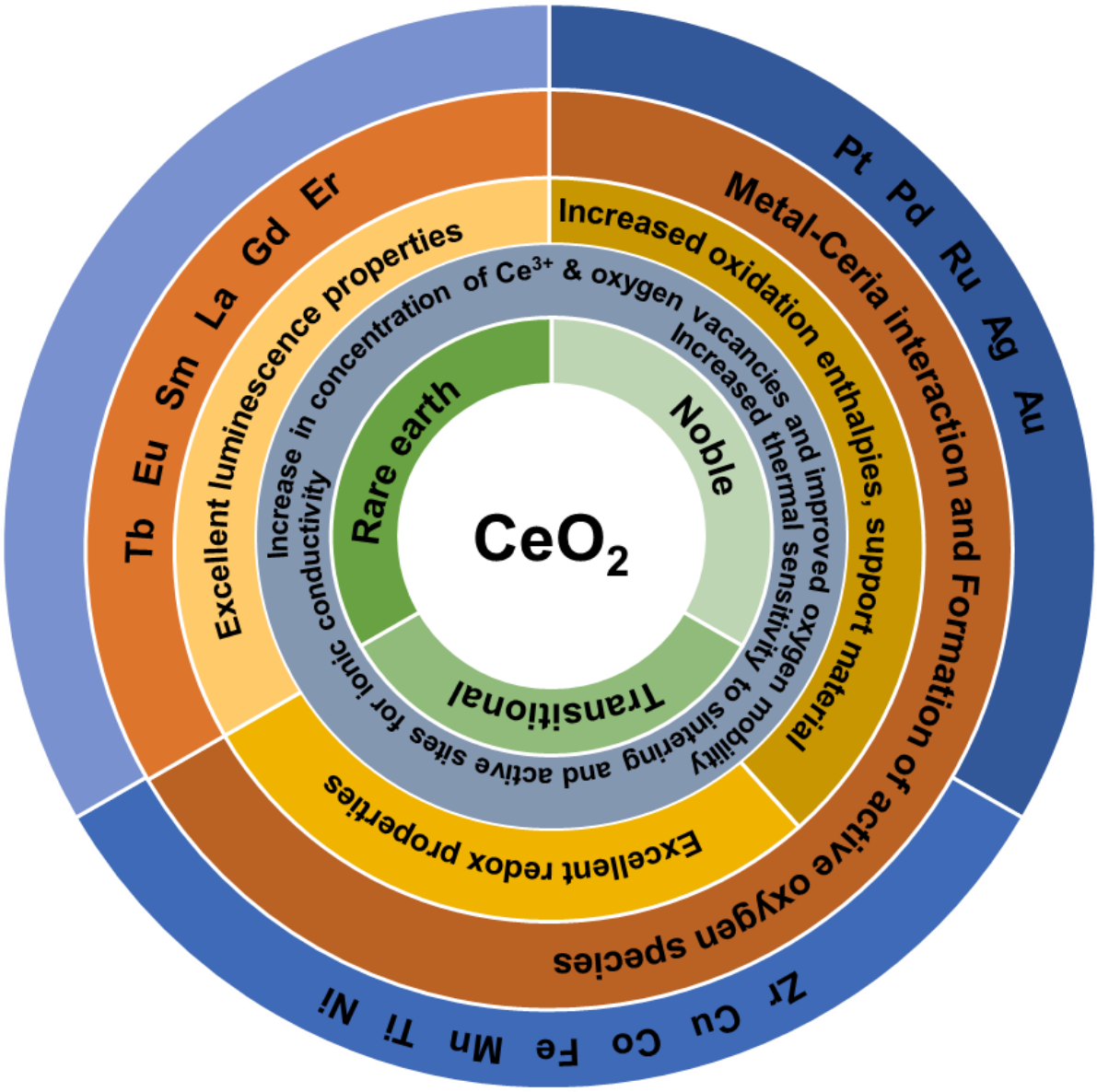

Figure 8. *Schematic of the physicochemical properties of rare earth, noble and transitional metal doped ceria particles used to obtain mixed and doped structures with CeO_2.*

The improved catalytic activity of doped CeNPs has been generally attributed to an increased concentration of oxygen vacancies and Ce^{3+}, and OSC. Other factors like large surface area, improved redox activity, enhanced thermal resistance and the synergistic interaction between the metal and ceria also contribute to the enhanced activity. Almost all transition and noble metals investigated were reported to enhance catalytic activity. Nevertheless, other factors like the preparation method, concentration of the dopant, type of dopant, oxidation state, crystal structure, also influence the catalytic properties of doped ceria[144-146].

Experimental studies provide critical information on the characteristics of the catalyst, oxidation reactions, surface processes and its mechanism. Selection of appropriate characterization methods is essential in gaining mechanistic details on important aspects of the ceria's activity such as metal-ceria interactions, role of the dopant, oxygen vacancy defect and surface oxygen species[125]. In addition to experimental tools, theoretical studies based on computer simulations can provide atomistic understanding of the structure of ceria-based catalysts, the role of dopant, oxygen vacancy defect and Ce^{3+} ions on catalytic properties of catalysts.

Detailed structural analysis of $Ce_{1-x}Zr_xO_2$ catalyst suggests that the formation of long and short Zr-O bonds in fluorite structure is mainly responsible for enhanced OSC observed for ceria-zirconia[147-149]. Substitution of Ce^{4+} ion with Zr^{4+} increases the reducibility of Ce^{4+} in ceria although ZrO_2 is not a reducible oxide. Addition of reducible ions like Sn^{4+} and Ti^{4+} into the ceria lattice can enhance the OSC of $Ce_{1-x}Sn_xO_2$ and $Ce_{1-x}Ti_xO_2$, respectively. Along with Ce^{4+}/Ce^{3+} couple, the Sn^{4+}/Sn^{2+} and Ti^{4+}/Ti^{3+} redox couples can also contribute to and therefore increase the reducibility of CeNPs. The coordination around Ti^{4+} or Sn^{4+} ion is different from the fluorite structure of ceria due to the lower ionic radius (0.74 Å for Ti^{4+} and 0.69 Å for Sn^{4+}) of these ions as compared to that of Ce^{4+} ion (0.97 Å) and this results in distortion of the ceria lattice[150-152].

Computational methods were used to study the properties of doped ceria materials[72, 153, 154]. The distortion of the oxygen sublattice leads to long and short Ce-O and Ti-O, Zr-O, Fe-O, and Zn-O bonds in CeO_2-TiO_2, CeO_2-ZrO_2, CeO_2-Fe_2O_3 and CeO_2-ZnO_2 solid solutions. The increased reducibility of these materials was explained by weak longer bonds[155, 156]. The Ce^{4+} coordination gets distorted to 4 + 4 type coordination from its ideal 8-fold coordination in these different materials. Transition and noble metal ion doping significantly enhanced the reducibility of $Ce_{1-x}M_xO_{2-\delta}$ (M = Co, Mn, Cu, Ni, Fe, Ru, Pt, and Pd) whereas doping with rare earth metal ions $Ce_{1-x}A_xO_{2-\delta}$ (A = La, Y) was seen to have little effect in increasing the OSC and reducibility of ceria. The optimized structure obtained by computer simulations exhibited deviation in bond length of cation-oxygen from the ideal bond length value of 2.34 Å (for Ce-O in CeO_2)[155]. For instance, simulation results for $Ce_{28}Mn_4O_{62}$ structure showed that the mean Mn-O bond length was 2.0 Å in 4 + 2 coordination. Doping with other transition and noble metal ions also changed the coordination of Ce^{4+} and formed longer Ce-O bonds. Addition of Pd in $Ce_{1-x}M_xO_{2-\delta}$ (M = Mn Ni, Fe, Cu and Co) resulted in further increment in OSC and correspondingly the model calculations revealed a further increment in bond length. These enhancements have been attributed to improved

reducibility of both host and dopant ions induced because of lattice distortion in the presence of dopant[72]. In the case of rare earth ion doping, the calculations showed very little increase in bonds lengths from fluorite structure and therefore the absence of longer Ce-O and RE-O (rare earth or RE = La and Y) bonds make the resulting structure less susceptible to reduction[153].

Dopants like Zr, Hf, Ti, Nb and Ta in the (110) ceria surface reduce the oxygen vacancy formation energy[157]. Pentavalent dopants like Nb and Ta in the (110) ceria surface enhance reducibility by charge transfer from the dopant ion to a cerium ion in the surface. Doping of ceria with Pd and Pt also lowers the oxygen vacancy formation energy attributable to the gap states formed above the valence band and below the empty Ce 4f states[158]. Alfredsson and Catlow compared the adsorption energies of Pt and Pd on (111) zirconia and ceria surfaces using periodic DFT analysis[159]. They found higher adsorption energies for Pt layer (400 kJ/mol) on both ceria and zirconia than Pd layer (200 kJ/mol).

Krcha et al. used density functional theory (DFT + U) to investigate the structural and electronic effects of transition metal dopants belonging to groups IV–XII in the (111) surface of ceria[160]. The dopant can have an oxidation state anywhere between 3+ and 8+ and in such a case the Ce^{4+} ions are reduced to Ce^{3+} only when the dopant has an oxidation state higher than 4+. **Figure 9a** summarizes the oxidation state of dopant in both the completely oxidized and oxygen vacant surfaces. The transition metal ions in groups IV and V change the surface reducibility and the ones in groups X–XII become the reduction center. Metal ions in groups IV and V are associated with their stable oxidation states of 4+ and 5+, respectively in the oxidized as well as reduced surfaces. Metal ions of groups X–XII are associated with 4+ oxidation state in oxidized surface and a 2+ oxidation state in reduced surface. Au, however, is an exception as it has a 3+ oxidation state in reduced surface. There is no clear trend in metal ions of groups VI through IX. Group metals have a 6+ oxidation state and the metals in the 4^{th} row of groups VII, VIII and IX (Co, Fe and Mn) have a 4+ oxidation state in oxidized surface and a 3+ oxidation state in reduced surface. They also showed that the oxygen vacancy formation energy decreases with the group number as shown in **Figure 9b.** The oxygen vacancy formation energies are usually higher when the dopant reduces as compared to only when Ce reduces. Oxygen vacancy formation increases more or less linearly with M-O bond energy as shown in **Figure 9c**.

(a)

Ti	V	Cr	Mn	Fe	Co	Ni	Cu	Zn
Zr	Nb	Mo	Tc	Ru	Rh	Pd	Ag	Cd
Hf	Ta	W	Re	Os	Ir	Pt	Au	Hg

Key	Fully Oxidized		Reduced		Atom Reduces
	Dopant	Cerium	Dopant	Cerium	
	4+	All 4+	3+	1 – 3+	Cerium & Dopant
	4+	All 4+	4+	2 – 3+	Cerium
	5+	1 – 3+	5+	3 – 3+	Cerium
	6+	2 – 3+	5+	3 – 3+	Cerium & Dopant
	6+	2 – 3+	6+	4 – 3+	Cerium
	7+	3 – 3+	6+	4 – 3+	Cerium & Dopant
	4+	All 4+	2+	All 4+	Dopant

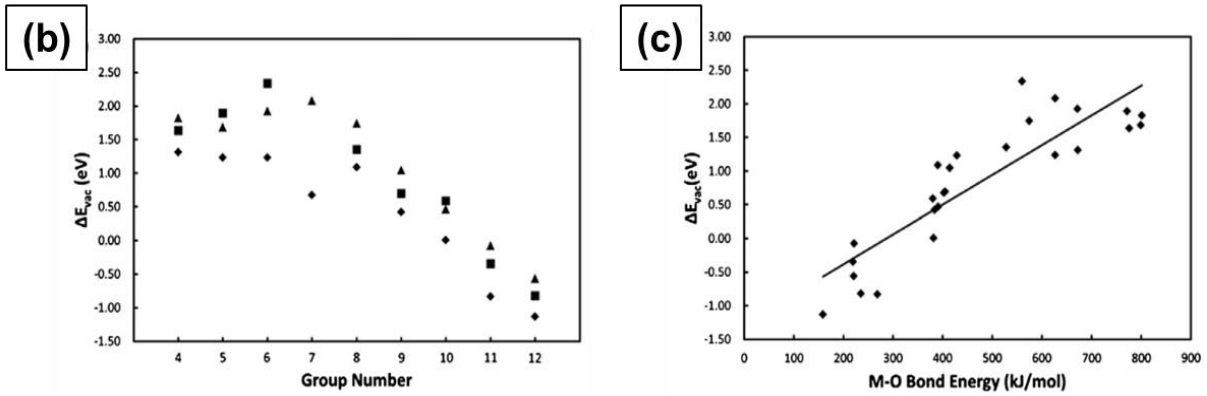

Figure 9. *(a) Trends in the electronic behavior of M-doped CeO_2 upon the formation of a surface oxygen vacancy in the nearest neighbor, Relationship between (b) oxygen vacancy formation energy and metal ion dopant column in the periodic table of elements and (c) oxygen vacancy formation energy and M-O bond dissociation energy. Reprinted from Ref [160].*

Structural changes or effects modifying the Ce-O chemical bonding are local effects while the global electronic structure is considered as global effect[101]. To identify whether a particular dopant exhibited a local or global effect, the dopant ion was placed next to and far away from oxygen vacancy and the vacancy formation energy was calculated. If the energy of forming an oxygen vacancy far away from the dopant is equal to the energy of forming a vacancy on nondoped oxide, then the dopant has a local effect. On the other hand, if the energy needed to form a vacancy next to the dopant is equal to that needed to form a vacancy far from it, then the dopant has a global effect. Dopants like La and Y reduce the energy needed for formation of an oxygen vacancy next to them or far from them[72]. Such dopant ions affect vacancy formation energy due to the creation

of a hole in the valence band maximum. When an oxygen vacancy is formed, one of the two electrons fills the hole and the other electron occupies a Ce 4f state. As the Ce 4f gap states are energetically higher than the hole states, La or Y doping lowers the vacancy formation energy. This is considered as a global effect as this mechanism is found to be independent of the distance between the vacancy formation site and the dopant. In case of non-reducible dopant like Zr, since Zr^{4+} is smaller than Ce^{4+}, structure relaxation effects drive the lowering of the vacancy formation energy and hence the energies of the doped and defective surfaces are about the same. On the contrary, reducible dopants like Pt, Ru, Nb and Ta exhibit both local and global effects and hence the energy required to form a vacancy near the dopant is lower than that required to create a vacancy defect away from it. The local effect with these dopants is related to the chemical interaction i.e. dopant-oxygen binding.

The catalytic properties at the interface of ceria-metal have been extensively studied, as this interface is the favored spot for exchange of oxygen and is recognized as the active site responsible for the enhanced catalytic activity[161, 162]. An interfacial reaction mechanism was proposed in which CO is suggested to be adsorbed on the metal and then oxidized by oxygen transfer from ceria, which in turn is oxidized by H_2O[163, 164]. More detailed information has been obtained on the ceria–metal interaction in which ceria is supported on the metal[165]. Additional proof of the interfacial activity involving dissociation of CO-like molecules on oxygen vacancies on the ceria surface and a systematic investigation of ceria-metal properties has been demonstrated using advanced characterization techniques[166-168]. Some of the important fundamental observations of these studies explain the enhanced catalytic activities due to: (a) the interplay between metal and oxygen vacancy, with the metal enabling the creation of oxygen vacancies on ceria; (b) the primary role of interface spots in the creation of reaction intermediates, therefore describing the different behaviors of metal–ceria systems and the ceria or metal alone; and (c) the presence of Ce^{3+} species under transient reaction conditions in CO oxidation mechanism.

Theoretical studies using DFT calculations have unraveled a great deal of information on the structure of ceria-based catalysts, the mechanism and the role of oxygen vacancy defects and dopants in enhancing the catalytic activity. These results are in line with those of experimental studies and hence are helpful in gaining a fundamental understanding of the catalytic attributes of ceria-based materials in industrially relevant applications. While extensive research has been dedicated to this topic over the past twenty, there remain several questions that still have to be

explored. (i) Will different sized doped-ceria materials behave differently – does size of the doped-ceria particle have an influence on catalytic activity; (ii) Can any dopant enhance the catalytic activity – can dopants be grouped into different categories like dopants that have a very little effect and the ones that have significant effect on catalytic activity; (iii) Will doping with multiple metals enhance the catalytic activity greatly? If yes, what combination of metals can do this; (iv) Will surface coating on doped ceria particles alter their catalytic properties (iiv); Is surface modification by addition of metal oxide clusters possible? If yes, what impact will it have on catalytic activity?

2.5. Free radical scavenging

The distinctive free radical scavenging and regenerative antioxidant properties of the CeNPs have attracted considerable interest in a broad range of applications in biomedicine[169-171]. In 2007, Seal's group first showed that CeNPs can efficiently scavenge superoxide radical anions and attributed this scavenging activity to the ability of Ce to switch between 3+ and 4+ oxidation states[172]. Subsequently, Pirmohamed and coworkers reported that the CeNPs show catalase mimetic activity[173]. Over the past decade, CeNPs have been investigated intensively as a potential therapeutic tool to inactivate free radicals and ameliorate causes of oxidative stress in a variety of *in vitro* and *in vivo* models, including cells, bacteria and whole animals. CeNPs can show antioxidant enzyme-mimetic activity, scavenge reactive oxygen species (ROS) and reactive nitrogen species (RNS) and protect against radiation[174-178]. They were also found to be effective in treating many diseases including cardiovascular diseases and neurodisorders[170, 179, 180]. Here, we review reaction mechanisms and discuss the physicochemical properties of CeNPs that are responsible for their ROS/RNS scavenging activities and enable them to be used in pharmaceutical and biomedical applications.

2.5.1. Antioxidant enzyme-like mimetic and ROS scavenging activity

ROS ($O_2^{\bullet -}$, H_2O_2, •OH) and RNS ($ONOO^-$ and •NO) are powerful oxidizing and nitrating agents that play a critical role in several important biological processes including signal transduction, biochemical reactions and physiological and pathological changes[181]. While ROS/RNS are important in cell signaling, an excessive level of these species can damage the DNA, proteins and lipids and thereby cause oxidative stress that subsequently results in the damage of

tissues and cells. These conditions can lead to diseases like cancer, diabetes, cardiovascular and neurodegenerative diseases and arthritis[182, 183]. While conventional antioxidants can only scavenge a particular type of ROS or RNS, CeNPs can scavenge many ROS and RNS, and their effectiveness is dependent of the size and surface properties of the NPs. The deleterious effects arising from surplus $O_2^{\bullet-}$ are usually controlled and alleviated by endogenous SOD enzymes located in the cytoplasm and mitochondria[184]. SOD enzymes eliminate $O_2^{\bullet-}$ species by converting them to O_2 and H_2O_2 through a catalytic dismutation reaction that occurs in two steps as follows[185, 186]. This process is schematically shown in **Figure 10a**.

$$O_2^{\bullet-} + 2H^+ + (Cu+)\text{-SOD} \rightarrow H_2O_2 + (Cu^{2+})\text{-SOD} \quad (\mathbf{2.6})$$

$$O_2^{\bullet-} + (Cu^{2+})\text{-SOD} \rightarrow O_2 + (Cu^{+})\text{-SOD} \quad (\mathbf{2.7})$$

$$2O_2^{\bullet-} + 2H^+ \rightarrow H_2O_2 + O_2 \text{ (overall)} \quad (\mathbf{2.8})$$

The SOD enzyme works by accepting electrons from or losing electrons to $O_2^{\bullet-}$. In reaction **2.6**, the reduced (Cu^+)-SOD catalyzes the oxidation of $O_2^{\bullet-}$ to H_2O_2 while in reaction **2.7**, the oxidized (Cu^{2+})-SOD catalyzes the reduction of $O_2^{\bullet-}$ to O_2. Reduced (Cu^+)-SOD is regenerated after reaction **2.7** and the cycle begins again. Overall, for every molecule of H_2O_2 formed, $2O_2^{\bullet-}$ molecules are dismutated. A similar mechanism for superoxide radical anion scavenging by ceria NPs has been proposed involving oxidoreduction of Ce^{3+}/Ce^{4+} states at the NP surface, as shown below[170, 180].

$$O_2^{\bullet-} + Ce^{3+} + 2H^+ \rightarrow H_2O_2 + Ce^{4+} \text{ (Oxidation of } Ce^{3+} \text{ to } Ce^{4+}) \quad (\mathbf{2.9})$$

$$O_2^{\bullet-} + Ce^{4+} \rightarrow O_2 + Ce^{3+} \text{ (Reduction of } Ce^{4+} \text{ to } Ce^{3+}) \quad (\mathbf{2.10})$$

The above two reactions indicate that the Ce^{3+}/Ce^{4+} redox couple of ceria NPs can be regenerated. In the first step, superoxide anions bind to oxygen vacancies around two Ce^{3+} species and an electron is transferred from Ce^{3+} ion to an oxygen atom. In the second step, two protons in the solution bind to two oxygen atoms and form a molecule of H_2O_2. The second superoxide anion then binds to the remaining oxygen vacancy and a second H_2O_2 molecule is formed and Ce^{3+} is oxidized to Ce^{4+}. Furthermore, the two electrons produced will reduce the Ce^{4+} ions to Ce^{3+} ions and in this case H_2O_2 acts as a reducing agent. However, while these reactions have been postulated, the mechanisms driving the SOD-mimetic activity of ceria NPs are still subject to debate and their behavior in biological environments are subject of numerous scientific investigations. In some studies, CeNPs having higher Ce^{3+} concentration were more efficient

scavengers of $O_2^{\bullet-}$ than those with lower Ce^{3+} concentration[172]. In another study, CeNPs treated with H_2O_2 and hence having lower Ce^{3+} concentration showed a decrease in the SOD mimetic activity as compared to bare ceria, implying that the surface Ce^{3+} species play a key role in SOD mimetic activity[187] as indicated in **Figure 10c**. These processes take place at the surface of the metal oxide and are affected by conditions such as pH and temperature.[169]

High H_2O_2 levels are considered detrimental to cellular homeostasis as compared to high levels of $O_2^{\bullet-}$ as H_2O_2 forms highly toxic •OH radicals via the Fenton reaction with metals as shown in **Figure 10a**. Enzymes like glutathione peroxidase, catalase and peroxiredoxins all lower the H_2O_2 levels in cells, but catalase is the most efficient enzyme in disproportionating H_2O_2 into innocuous H_2O and O_2 [188] as shown in **Figure 10a**. The catalase mimetic activity of CeNPs was first demonstrated based on the shift in the peak in luminescence spectra of ceria NPs after addition of H_2O_2 to astrocyte cells[174]. The luminescence spectra of the CeNPs reversed to its original form (the peak shifted back to the original wavelength) after decomposition of H_2O_2. The CeNPs protect cells from oxidative stress due to their catalase mimetic and SOD mimetic activities. The catalase mimetic activity depends strongly on the concentration of Ce^{3+} with ceria having low Ce^{3+} concentration showing improved catalase activity as compared to those with high concentration of Ce^{3+} [173] as indicated in **Figure 10c**.

Besides, Ce^{3+} concentration, factors like particle size, buffer species like PO_4^{3-}, and solution pH can all affect the catalase and SOD-mimetic activities of ceria[189, 190]. The presence of PO_4^{3-} was shown to diminish the SOD-mimetic activity and enhance the catalase activity due to the ability of Ce^{3+} ions to form strong coordination complexes on reaction with PO_4^{3-}, which bind preferentially to ceria NPs with high Ce^{3+} concentration. The mechanism by which phosphate changed the properties of ceria NPs was attributed to formation of $CePO_4$-like complexes that blocks the redox activity of ceria NPs[189]. Since the ability of ceria particles to cycle between 3+ and 4+ oxidation states is the key to their catalytic activity, the catalase mimetic activity diminishes in the presence of any compound that can block Ce^{3+} and stabilize the ceria NPs in the 3+ state. Therefore, the ability of CeNPs to swiftly change between 3+ and 4+ oxidation states is crucial in maintaining their SOD-mimetic activity. These studies indicate the need to comprehensively study and understand the influence of phosphate ions, and other ions on SOD mimetic activity of ceria, particularly because cells contain high concentrations of phosphate ions, and other ions and their presence can potentially affect the biological activities of ceria NPs.

Contradictory results were reported in literature on the influence of pH on the antioxidant activity of CeNPs with some studies showing no effect of pH and other studies revealing marked effects on both the SOD mimetic activity and Ce^{3+} concentration on the particle surface. Singh et al.[189] and Xue et al.[176] showed that the dispersion stability and SOD mimetic activity of ceria NPs are not affected by pH. In contrast, using XPS spectroscopy, Karakoti et al. showed that the Ce^{3+} concentration changed with pH[191]. Perez et al. investigated the effect of pH on antioxidant properties of CeNPs[190]. Dextran coated-ceria NPs exhibited catalase mimetic activity in alkaline conditions but not in acidic conditions (pH 4). They argued that the antioxidant ability of ceria NPs is dependent on their ability to cycle between 3+ and 4+ oxidation states and that the Ce^{3+} ions are converted to Ce^{4+} ions during the H_2O_2 scavenging process. Regeneration of Ce^{3+} occurs through chemical reactions between Ce^{4+} ions on the surface of NPs and H^+ ions in solution as shown in **Figure 10b**. The low pH of the solution inhibited the ability of ceria NPs to scavenge more free radicals and therefore diminished the antioxidant activity due to the high concentration of H^+ ions. These conflicting results could be due to different synthesis methods and hence varying surface Ce^{3+} concentrations. Moreover, the effect of surface coating or surface reactions, and the potential binding of peroxide and superoxide species to the ceria surface, and the stabilizing effects of coexisting ions, have not been taken into account in these studies, and can have significant effects in biological environments. Systematic studies of the effect of surface ligands, surface faceting and a potential reorganization of ceria NPs, are essential next steps needed to understand these processes, the interfacial reactions and their contribution to the ceria's unique reactivity.

CeNPs can also efficiently scavenge •OH (hydroxyl radical), a strong oxidant. Hydroxyl radicals in cells are usually scavenged by two methods. The first method involves preventing initiation of •OH by enzymes like SOD, catalase and glutathione peroxidase. The second method involves breaking of the chain reaction of •OH by nonenzymatic antioxidants[192]. The •OH scavenging ability of CeNPs was first shown by Das et al. who first demonstrated that CeNPs were able to scavenge •OH formed from H_2O_2 [175]. When CeNPs were treated with H_2O_2, the color changed from yellow to orange indicating that Ce^{3+} (yellow) reacts with the •OH generated from H_2O_2 and gets oxidized to Ce^{4+} (orange) as shown in **Figure 10a**. In a later report, Xue et al. demonstrated that CeNPs scavenge •OH by providing direct experimental evidence *via* a methyl violet assay[176]. With the decrease in the size of CeNPs and a corresponding increase in the concentration of surface Ce^{3+}, the efficiency of CeNPs in scavenging •OH and preventing a

reduction in the optical absorption of methyl violet increased. The •OH scavenging activity of CeNPs was attributed to a two-step mechanism involving the ability of •OH to reversibly cycle between Ce^{3+} and Ce^{4+} In the first step, •OH oxidizes Ce^{3+} to Ce^{4+}, and in the second step, Ce^{4+} is reduced back to Ce^{3+}. The mechanism can be described by the chemical reactions **2.9** and **2.10** and is also schematically represented [193] in **Figure 10b**. The morphology of CeNPs was also found to have a significant impact on their scavenging activity to the different crystal planes exposed by different morphologies. The antioxidant activity of different morphologies follows the order: nanowires > nanobars > NPs[194]. Better understanding of the catalytic mechanisms and the fundamental parameters affecting the 'enzyme-like' activity will enable future development of high performance nanoenzymes[195, 196] as alternatives to natural oxidase and peroxidase enzymes, providing advantages such as a stability, robustness and low cost, making them suitable for many applications.

2.5.2. RNS scavenging activity

Nitric oxide (NO) is not a highly reactive molecule but, nitric oxide radical (•NO) reacts with $O_2^{\bullet-}$ or O_2 and forms the highly reactive and damaging peroxynitrite anion ($OONO^-$) (**Figure 10a)** that can damage lipids, DNA and proteins[197]. Self and co-workers showed that CeNPs scavenge •NO under physiologically relevant conditions[198] and showed that the •NO scavenging was more predominant in particles with a lower concentration of Ce^{3+} and oxygen vacancies in contrast to the SOD-mimetic activity which is predominant in particles with a higher concentration of Ce^{3+} and oxygen vacancies. They postulated that the CeNPs scavenge •NO with the help of electropositive nitrosyl ligand formed by internal electron transfer from •NO to a Ce^{4+} ion according to the following reaction.

$$Ce^{4+} + \bullet NO \rightarrow (Ce^{4+}NO \leftrightarrow Ce^{3+}NO^{+}) \quad (\mathbf{2.11})$$

Figure 10c summarizes the SOD and catalase mimetic properties and •NO and $OONO^-$ scavenging properties of CeNPs and the effect of the relative surface Ce^{3+} concentration on varying radicals..

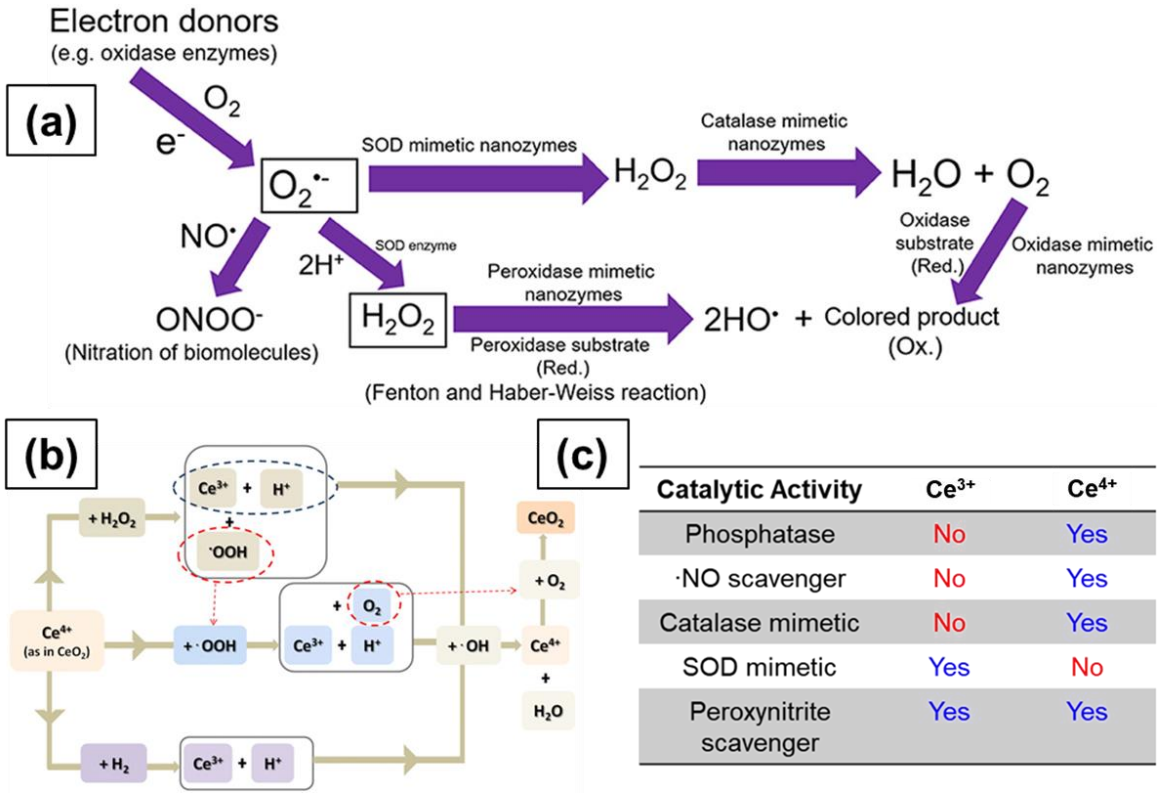

***Figure 10**. (a) Schematic representation showing the reactions involved in antioxidant enzyme-mimetic and ROS and RNS scavenging properties of ceria particles. Superoxide ($O_2^{\bullet-}$) anions are first produced by single electron donors and the $O_2^{\bullet-}$ anions react with •NO and H^+ to form $OONO^-$ and H_2O_2, respectively. The $O_2^{\bullet-}$ anions are converted to H_2O_2 by SOD and SOD mimetic enzymes. Catalase mimetic enzymes can further convert H_2O_2 into water and oxygen. Hydroxyl radicals can be generated from H_2O_2 in the presence of peroxidase mimetic enzymes and oxidase mimetic enzymes can oxidize the substrate and form a colored product without the presence of H_2O_2. Reprinted from Ref [199]. (b) Transformation of Ce^{3+} to Ce^{4+} and regeneration of Ce^{3+} from Ce^{4+}. Reprinted from Ref.[193] (c) Effect of SOD and catalase mimetic properties and •NO and $OONO^-$ scavenging properties of ceria particles on the relative surface Ce^{3+} concentration of ceria. Reprinted with permission from Ref [200].Copyright 2013 American Chemical Society.*

2.5.3. Peroxidase and phosphatase-like mimetic activities

CeNPs exhibit peroxidase, oxidase and phosphatase mimetic activities. Heckert et al. explored the ability of CeNPs to catalyze a Fenton-like reaction in the presence of H_2O_2 and showed that $CeCl_3$ generated hydroxyl radicals in the presence of H_2O_2 [187]. EPR analysis indicated the generation of both •OH and $O_2^{\bullet-}$ in the presence of cerium and H_2O_2. The authors hypothesized that •OH and $O_2^{\bullet-}$ were generated from reactions similar to Fenton/ Haber Weiss reactions:

$$Ce^{3+} + H_2O_2 + H^+ \rightarrow Ce^{4+} + \bullet OH + H_2O \quad (\mathbf{2.12})$$

$$\bullet OH + H_2O_2 \rightarrow HO_2^- + H_2O \quad (\mathbf{2.13})$$

$$Ce^{4+} + HO_2^- \rightarrow O_2 + Ce^{3+} + H^+ \quad (\mathbf{2.14})$$

CeNPs can exhibit the peroxidase-like catalytic activity over a wide range of temperatures and pH values, making them more stable substitutes to natural enzymes[201].

A phosphatase is an enzyme that hydrolyzes phosphoric acid monoesters into phosphate ions[202]. Phosphatase enzymes play a significant role in many biological processes, including signal transduction and cellular regulation. Some metal ions and their complexes were shown to enhance the rate of phosphate ester hydrolysis through different processes like nucleophile activation, Lewis acid activation and leaving group activation[203]. Lanthanide ions and their complexes are efficient catalysts for hydrolyzing phosphate esters[204]. CeNPs have been shown to effectively mediate the dephosphorylation of phosphopeptides[205] in less than ten minutes. The dephosphorylation activity of CeNPs was attributed to the Lewis acidity of Ce^{3+}/Ce^{4+} surface sites capable of coordinating oxygen atoms of phosphate groups and lowering the P–O bond scission energy by promoting nucleophilic attack from hydroxyl groups on the surface. Ceria NPs can also be used for dephosphorylation of biologically active amino acids[206]. Kuchma and collaborators investigated the reactivity of CeNPs towards phosphate ester bonds of biologically relevant molecules like ATP, p-nitrophenylphosphate (pNPP), DNA and o-phospho-L-tyrosine[207]. The dephosphorylation mechanism was investigated using DFT calculations and the reaction was found to proceed through phosphate group inversion similar to an SN2 mechanism. Because of the ability of CeNPs to interact with the phosphate ester bonds of biologically relevant molecules, they can be used as potential therapeutics.

The ability of CeNPs to eliminate surplus levels of $O_2^{\bullet -}$ and H_2O_2 from cells makes them ideal SOD and catalase-mimetic. Nevertheless, the exact mechanisms by which CeNPs act as antioxidant enzyme-mimetic in the cells have been a topic of debate. The variability in the types of CeNPs used in the *in vitro* and *in vivo* studies can strongly influence the surface Ce^{3+} concentration and hence their surface reactivity. Limitations of existing characterization tools and lack of sophisticated techniques to analyze such interactions in situ hinder the fundamental understanding of the enzyme-mimetic activity of the CeNPs. Apparent differences in results can also arise from different synthetic procedures of the particles. Moreover, the limited data on

detailed characterization of CeNPs exposed to biological environments that would take into account the effect of the medium composition, surface binding and non-specific adsorption on the particle reactivity makes it difficult to draw fundamental conclusions based on a direct comparison with the reported mimetic activity in simple aqueous solutions. Ideally, standards for synthesis techniques of CeNPs with a full characterization of their physicochemical properties should be established to prevent misinterpretation of results. Advances in different microscopy spectroscopic methods have been very helpful in the analytical characterization of these materials under biological conditions. Establishing a set of characterization tools that enable comprehensive correlation between the physicochemical properties of CeNPs and their antioxidant/prooxidant activity is necessary and, in principle, can be helpful in tuning the properties of the particles. A schematic of the SOD and catalase mimetic activities of pure ceria, triphenylphosphonium (TPP) coated ceria[208] and Gd-doped ceria[209] is shown in **Figure 11**, indicating the effect of surface ligands on CeNPs activity**.**

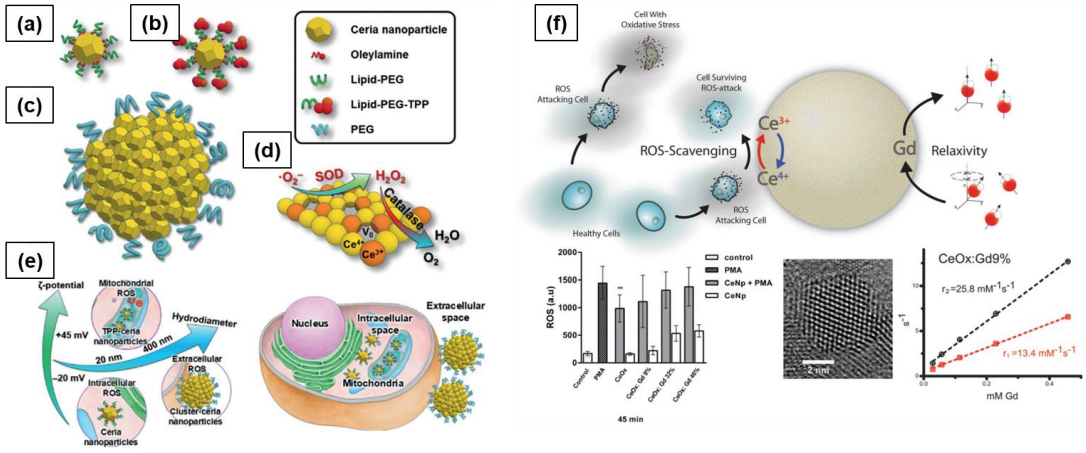

Figure 11. *Schematic showing (a) ceria particle, (b) Triphenylphosphonium (TPP) coated ceria particle, (c) ceria particle cluster, (d) SOD- and catalase-mimetic activities of ceria particles and associated ROS scavenging reactions, (e) ROS scavenging activities of ceria, TPP coated ceria and ceria particle cluster in cells and (f) top: Gd-doped ceria particles with antioxidant and MRI contrast enhancing properties; bottom: antioxidant assay, HRTEM image and relaxivity measurement results (from left to right). Reprinted from Refs [208] and [209].*

2.6. Interactions with molecular oxygen and H_2O_2

The characterization of different types of oxygen species formed by adsorption of O_2 on CeNPs is important as these species play a key role in many oxidation reactions. One of the major

applications of CeNPs is as an oxygen storage material in TWC converter in automotive exhausts. Ceria acts as a buffer to supply O_2 during O_2 deficient conditions of engine operation, and extract O_2 when there is surplus O_2 in the exhaust stream and thus helps to maintain the concentration of oxygen. The mechanism of oxidation reactions on ceria surfaces involves the reaction of the adsorbate with the O_2 present in the substrate, which is then replenished from the gas phase O_2 [125]. Studies to understand the adsorption and desorption of O_2 on ceria surfaces are thus critical for TWC applications. Using both experimental methods and theoretical models, it has been established that the reactivity of stoichiometric ceria (unreduced ceria) towards molecular oxygen is very low as compared to that of reduced ceria. O_2 physisorbs on the surface of unreduced ceria NPs by a weak interaction dominated by dispersion forces[210-212]. DFT calculations of oxygen adsorption revealed very low adsorption energies and showed that O_2 adsorbs only at very low temperatures on unreduced ceria. On the other hand, molecular oxygen binds very strongly on reduced ceria surfaces[213-215].

The formation mechanism involves creation of an oxygen vacancy which results in the formation of two Ce^{3+} ions and hence the vacancy site is a two-electron donor center. O_2 interacts with the oxygen vacancy and adsorbs such that one oxygen atom fills the vacancy and the other points out from the surface[210]. O_2 adsorption at an oxygen vacancy site therefore removes the defect and results in the formation of a surface peroxo species (O_2^{2-})[216]. The diamagnetic O_2^{2-} can be detected by Raman and FTIR spectroscopies. The peaks related to O_2^{2-} typically occur in the 820-880 cm^{-1} region[217]. O_2^- species on the other hand are formed when O_2 interacts with low-coordinated Ce^{3+} ions (steps, edges, dislocations, etc.) which are one-electron donors[218]. In this case, oxygen vacancies are not involved and O_2^- species are formed in the vicinity of exposed Ce^{3+} ions[213]. The fingerprint of the O_2^- species is, besides the characteristic EPR signal, a Raman or IR peak in the region 1110-1150 cm^{-1} [216].

Early experimental studies used FTIR spectroscopy to investigate the adsorption of O_2 on ceria. The adsorption of O_2 on partially reduced ceria resulted in an IR peak at 1128 cm^{-1} attributed to O_2^- species and at 883 cm^{-1} related to peroxide species. O_2^- and O_2^{2-} are the intermediates formed during oxygen dissociation/re-oxidation that occurs according to the following scheme[219].

$$O_{2(aq/g)} \leftrightarrow O_{2(ads)} \leftrightarrow O_2^-{}_{(ads)} \leftrightarrow O_2^{2-}{}_{(ads)} \leftrightarrow 2O^-{}_{(ads)} \leftrightarrow 2O^{2-}{}_{(lattice)} \quad (\mathbf{2.15})$$

where *aq* stands for aqueous and *ads* stands for adsorbed.

As can be seen from **Eq. 2.15**, first, the O_2^- is formed after exposure to O_2. The O_2^- is then converted into peroxide and finally to lattice oxygen by gaining more electrons from the surface. As a result of this re-oxidation, the surface will become electron deficient and further electron transfer from the surface to O_2 does not occur. Similar bands were also observed in studies that used Raman spectroscopy to probe the adsorption of O_2 on ceria. Pushkarev et al. studied adsorption of O_2 on CeNPs using in-situ Raman spectroscopy and demonstrated that O_2 adsorbs on one- and two-electron defects and forms O_2^- and O_2^{2-} species, respectively[215]. Two bands each in ranges of 1120-1140 cm^{-1} and 830-880 cm^{-1} related to superoxide and peroxide species, respectively were observed. The two different bands can be ascribed to disparate configurations of the binding of superoxide species to ceria and to the peroxide species bound to defects with different geometries. Temperature-programmed experiments revealed re-oxidation of the surface by adsorbed oxygen species. The O_2^- that form first due to adsorption of O_2 are unstable and transform into peroxides which then translate into lattice oxygen similar to what was reported previously.

Wu et al. investigated the adsorption of O_2 on ceria nanocubes, nanorods and nanooctahedra exposing (100), (110)/(100) and (111)/(100) crystal planes, respectively[220]. They illustrated the mechanism of oxygen activation and transformation on these surfaces, which is pivotal in understanding the mechanism of oxidation reactions catalyzed by nanoscale ceria. Adsorption of O_2 on ceria gave rise to a band at 1139 cm^{-1} which they attributed to O-O stretching of O_2^-. The other observed peaks at 830 and 860 cm^{-1} were ascribed to peroxide species on isolated and clustered two-electron defects. The amount of adsorbed oxygen species on reduced ceria nanoshapes changes with the degree of reduction. The weak bands of adsorbed oxygen species in ceria nanorods suggest the presence of small amounts of defect sites. Temperature dependent oxygen adsorption experiments revealed that the adsorbed O_2^- species were stable up to 350 K while the peroxide species were stable until 473 K. Based on their results, they suggested that the re-oxidation of ceria occurs as shown in **Eq. 2.15**. 20% of adsorbed oxygen desorbs into gas phase through disproportionation reactions of O_2^{2-} and O_2^- species as shown below.

$$O_2^-{}_{ads} + O_2^-{}_{ads} \rightarrow O_2^{2-}{}_{ads} + O_2 \quad (\mathbf{2.16})$$

$$O_2^{2-}{}_{ads} + O_2^{2-}{}_{ads} \rightarrow 2O^{2-}{}_{lattice} + O_2 \quad (\mathbf{2.17})$$

The adsorption of oxygen on (111) surface of ceria was studied using DFT calculations. O_2

does not adsorb on oxidized surfaces and binds weakly to one-electron defect sites[210]. O_2^- forms on hollow sites of (111) surface in a side-on configuration above Ce^{4+} ions. The O_2^- preferentially adsorbs on Ce^{4+} surface sites due to electrostatic interaction and hence $Ce^{4+}O_2^-$ is predicted to be the reactive intermediate as $Ce^{3+}O_2$ is more stable. Partially reduced ceria exposed to O_2 resulted in the formation of O_2^- and O_2^{2-} and the associated Raman peaks were observed at 1131 and 825 cm^{-1}, respectively[217]. The energies of O_2 adsorption on unreduced ceria surfaces were found to be endothermic while those on reduced surfaces were exothermic. The position of oxygen vacancies can affect the formation and dissociation of oxygen species.

Most of the experimental and theoretical results indicate that oxygen vacancy sites and Ce^{3+} play crucial roles in the formation of peroxide and superoxide species, respectively, and that these adsorbed oxygen species are active intermediates in the subsequent oxidation reactions[221, 222]. The possible geometries of adsorbed oxygen species at different active sites on the reduced and unreduced surfaces of ceria are depicted in **Figure 12**.

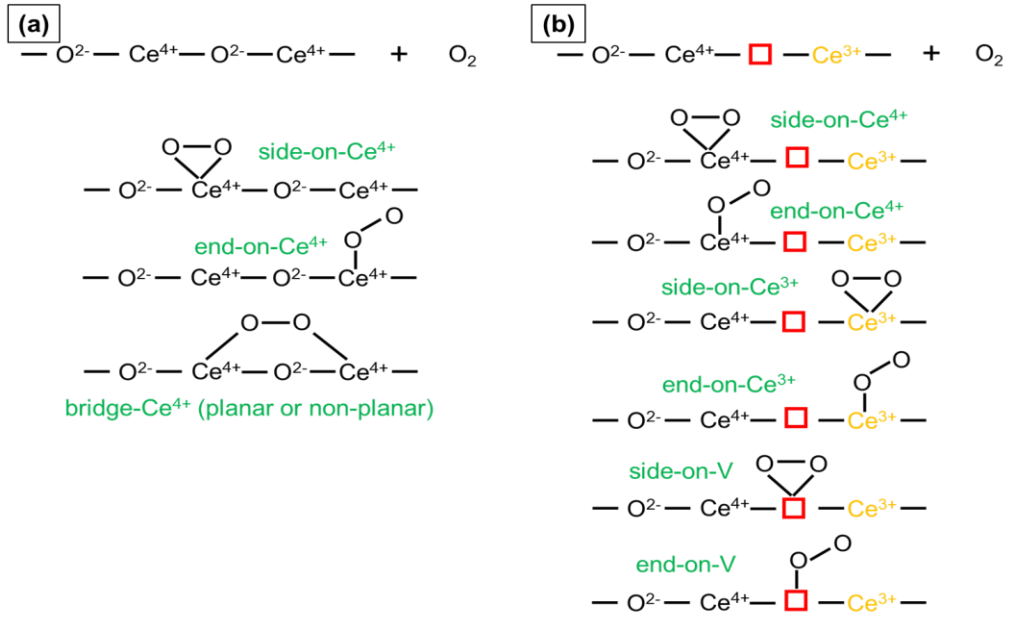

Figure 12. *Possible complexes of adsorbed oxygen species formed due to interaction of molecular O_2 with ceria NPs.*

The adsorption energies, vibrational frequencies, partial charges and relevant geometrical parameters for different configurations have been calculated by several theoretical studies[210, 213]. The end-on-V configuration of peroxide adsorption on ceria is energetically the most favorable one of all the possible structures. The side-on-V structure of superoxide adsorption is the second

stable structure. O_2 physisorbs (adsorbs very weakly) on Ce^{4+} of an unreduced surface in an end-on configuration. The values of energies suggest that O_2 binds very strongly above one-(Ce^{3+}) and two-electron defects (oxygen vacancies), implying that the dissociation process is energetically more favorable on the reduced ceria surface than on an oxidized surface[223].

In summary, O_2 adsorbs very strongly on the surface oxygen vacancy and forms diamagnetic peroxide species since two electrons from 4f orbitals of Ce^{3+} ions are transferred to the half-filled π_{2p}* orbitals of O_2[223]. O_2^{2-} species are formed from the adsorption of O_2 at low-coordinated Ce^{3+} ion that is quite far away from the oxygen vacancy site[213]. O_2 preferentially binds in a side-on configuration, with the end-on mode being less favorable. This interaction results in the charge transfer of one of the two electrons in 4f orbital of Ce^{3+} to the π_g* orbital of O_2. Simultaneously, one Ce^{3+} ion is oxidized to Ce^{4+} ion and a complex ($Ce^{4+}O_2^-$) is formed through ionic interaction[217].

The interaction of H_2O_2 with CeNPs was also studied in great detail in many reports on antioxidant activity relevant to biomedical applications. Nonetheless, the mechanism of reaction of H_2O_2 with CeNPs is still not completely understood. Postulating that H_2O_2 oxidizes Ce^{3+} to Ce^{4+}, it was shown that CeNPs exposed to H_2O_2 and, having lower concentration of Ce^{3+} suppressed the SOD mimetic activity[187]. Later, several studies demonstrated that the oxidation of Ce^{3+} to Ce^{4+} is reversible, and that the reduction happens after a long period (15 days) in aqueous solution following degradation of H_2O_2[180, 190]. The mechanism of reduction reaction was investigated, and it was proposed that H_2O_2 reacts with Ce^{4+} ions and reduces them to Ce^{3+} ions while it simultaneously gets oxidized to molecular O_2. Some controversies exist regarding the mechanism of oxidation/surface complexation of CeNPs, and the impact of surface coating on the oxidation/complexation in the presence of H_2O_2. Most of the studies ascribed the change in color of CeNPs in the presence of H_2O_2 to the conversion of Ce^{3+} to Ce^{4+} while some suggested that the color change was due to the formation of $Ce^{3+}O_2^{2-}$ and/or $Ce^{4+}O_2^-$ or Ce^{4+}.[224] With respect to surface coating, some studies showed that coating does not have any influence on the reaction of H_2O_2 with the particles while others showed apparent differences in the reactivity depending on surface coating[225, 226]. In a comparative study, the 8.2 nm ceria NPs coated with a thick layer of polyethylene imine or polymaleicanhydride-alt-1-octadecene were found to be less reactive than the smaller 3.8 nm with a thin layer of poly(lactic acid)[225].

Yu et al., developed an E-pH diagram for the CeO_2-H_2O-H_2O_2 system to understand the role of H_2O_2 in preparation of cerium conversion coating processes[227]. Their results indicated that H_2O_2

could perform dual functions, either oxidize Ce^{3+} to Ce^{4+} or reduce Ce^{4+} to Ce^{3+}. It was shown that H_2O_2 acts as a reducing agent at lower pH values (pH < 2) and as an oxidizing agent at higher pH values. Ce^{4+} can exist in several hydrolyzed forms depending on pH and the most stable ones are $Ce(OH)^{3+}$, $Ce(OH)_4$, $Ce(OH)_2^{2+}$ and polymerized form. The overall reaction for reducing action of H_2O_2 on Ce^{4+}, $Ce(OH)^{3+}$ and $Ce(OH)_2^{2+}$ in the pH regions < -0.7, -0.7-0.7 and 0.7-2.1, respectively can be written by the following equations:

$$2Ce^{4+} + H_2O_2 \rightarrow 2Ce^{3+} + O_2 + 2H^+ \quad (\mathbf{2.18})$$

$$2Ce(OH)^{3+} + H_2O_2 \rightarrow 2Ce^{3+} + O_2 + 2H_2O \quad (\mathbf{2.19})$$

$$2Ce(OH)_2^{2+} + H_2O_2 + 2H^+ \rightarrow 2Ce^{3+} + O_2 + 4H_2O \quad (\mathbf{2.20})$$

Ce^{3+} can be oxidized to Ce^{4+} in the presence of H_2O_2 with increasing pH and the oxidation reaction can be represented by the general equation shown below

$$2Ce^{3+} + H_2O_2 + xH_2O \rightarrow 2Ce(OH)_{1+x/2}^{(3-x/2)+} + xH^+ \quad (\mathbf{2.21})$$

where the value of x could be 0, 2 or 6.

Ce^{3+} is the more stable form in the lower pH range and Ce^{4+} can be reduced to Ce^{3+} by H_2O_2. Conversely, Ce^{4+} is the more stable form at higher pH values. Ce^{3+} is soluble over a wide pH range (pH <11) as compared to Ce^{4+} which is soluble at pH <4. During the oxidation of Ce^{3+} to Ce^{4+} with H_2O_2, the concentration of the intermediate Ce^{3+}/Ce^{4+} complexes is very high.

Scholes and co-workers performed titration of cerium-based conversion coating solutions to investigate the role of H_2O_2 [228]. The titration results indicated the formation of a Ce(III) peroxo complex like $Ce(H_2O_2)^{3+}$, and successive deprotonation led to the formation of $Ce^{3+}O_2^{2-}$ which on oxidation gave Ce(IV) peroxo species like $Ce(IV)(O_2)(OH)_2$. Finally, the Ce(IV)peroxo complex converted to CeO_2 after several months and the authors attributed the conversion to decomposition of the complex. The use of ceria NPs as colorimetric probes for the detection of glucose has been explored by several studies. Addition of H_2O_2 to a dilute dispersion of 20 nm ceria NPs (colorless) changed the color of the particles to reddish-orange[229] as shown in **Figure 13**. The color change indicates the modification in surface properties and chemical composition of the ceria NPs. FTIR analysis confirmed the presence of peroxo species in the presence of H_2O_2 and XPS analysis indicated a slight change in the concentration of Ce^{4+}. Ultraviolet-visible (UV−Vis) absorption analysis shows a red-shift in the spectra of CeNPs in the presence of H_2O_2 with the extent of red

shift increasing with the concentration of H_2O_2[230 231]. The coordination number of Ce ions after H_2O_2 addition was found to increase based on analysis of x-ray absorption fine structure (XAFS) measurements. However, the coordination number decreased back nearly to the original value at the end of the reaction (after 9 hours); the increase in the coordination number was attributed to the formation of surface adsorbed peroxide complexes.

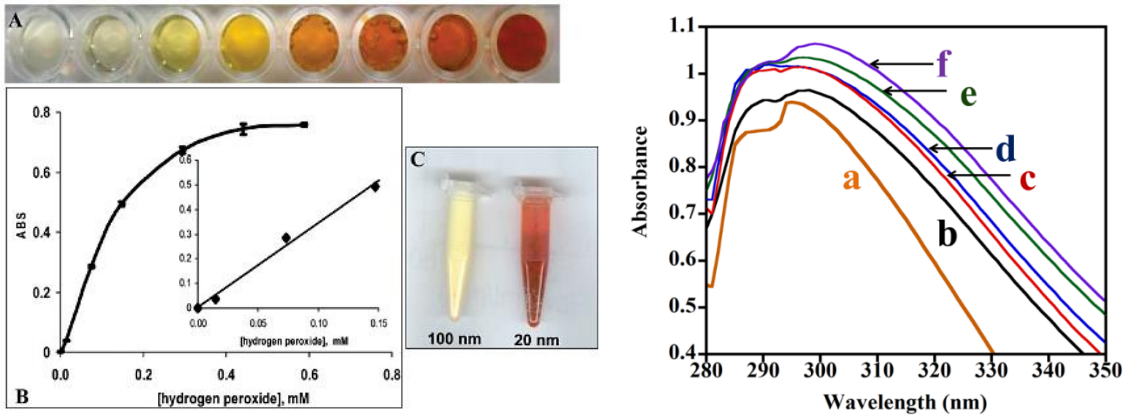

Figure 13. *Left. Colorimetric analysis of colloidal ceria nanoparticle dispersion treated with H_2O_2 as a function of H_2O_2 concentration at neutral pH indicating color change proportional with the concentration of H_2O_2: (A) Photos of ceria dispersions showing color with increasing intensity as a function of H_2O_2 concentration (B) Calibration curve obtained by plotting optical absorption as a function of H_2O_2 concentration. Inset shows the linear region. (C) Effect of H_2O_2 addition to ceria dispersion on particle size (20 and 100 nm ceria). Reprinted with permission from Ref [229]. Copyright 2011 American Chemical Society. Right. UV spectra illustrating the CeO_2 NPs peaks of Ce^{3+} (289 nm) and Ce^{4+} (297 nm) for unreduced CeO_2 NPs (no H_2O_2) (a) and CeO_2 NPs reduced for 30 min with different H_2O_2 concentrations of 5 mM (b), 10 mM (c), 20 mM (d), 50 mM (e) and 100 mM (f). Reprinted with permission from Ref [230]. Copyright 2013 American Chemical Society.*

The interaction of H_2O_2 with oleate capped CeNPs in dichloromethane (DCM) was investigated[232]. **Figure 14** shows the UV-Vis spectra of CeNPs treated with H_2O_2 as a function of time in the wavelength range of 200 to 700 nm. H_2O_2 addition was found to increase the absorbance at 2 wavelengths (λ_1 = 285 nm) and (λ_2 = 380 nm). Deconvolution of the UV-Vis spectra of the H_2O_2 adsorption by CeNPs revealed the appearance of two peaks corresponding to two processes: the peak at 285 nm was related to the oxidation of Ce^{3+} to Ce^{4+} while the peak at 380 nm was due to the formation of surface adsorbed peroxide species. Further, the FTIR peak at 840 cm^{-1} indicated the presence of peroxide/hydroperoxide species.

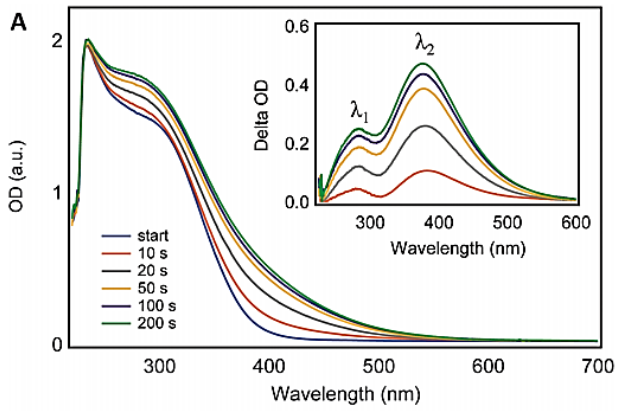

Figure 14. *UV-Vis spectra of CeNPs dispersion treated with H_2O_2 obtained as a function of time. Reproduced from Ref [232] with permission from the Royal Society of Chemistry.*

It should be noted that in an aqueous medium, ceria can exist in different hydrolyzed forms like $Ce(OH)_2^{2+}$, $Ce(OH)_3$, and $Ce(OH)_4$, and after addition of H_2O_2, it can form cerium (III) peroxide ($Ce^{3+}O_2^{2-}$), cerium (IV) peroxide ($Ce^{4+}O_2^{2-}$) and cerium hydroperoxide ($Ce(OH)_2(O_2)$). Certainly, the ratio of these different species is dependent on the size, surface coating, preparation method, pH and ionic strength. These complexes are reversible and the particles can recover their activity after several days/weeks at room temperature, or within few minutes at high temperatures of 70–100 °C due to decomposition of the surface adsorbed peroxide and hydroperoxides[5].

2.7. Dissolution of ceria-based systems as a promising strategy for regeneration

Every year, large quantities of ceria-based materials are used in TWC converters in automotive exhausts and CMP of dielectric films during integrated circuit (IC) fabrication. Recent reports suggest record high increases in the price of cerium-based materials due to more stringent export rules of the world's largest producer of rare earth materials and scarcity of cerium materials[233, 234]. A threefold approach which includes recycling and reuse of these materials and development of alternative materials having less hazardous ecological impacts has been proposed. Selective dissolution of ceria-based systems appears as a promising strategy to recover cerium and hence thorough knowledge about the fundamental aspects of ceria dissolution is essential[235]. Here we review the methods proposed for ceria dissolution and the impact of several parameters on dissolution.

Dissolution of ceria is not thermodynamically favorable ($\Delta_rG°$ = 40 kJ/mol) even in

concentrated mineral acid solutions[236, 237]. However reductive dissolution of ceria is feasible due to the highly positive redox potential of Ce^{4+}/Ce^{3+} couple (1.4 V per SHE)[238]. A solution containing a very strong mineral acid and a reducing agent can effectively dissolve ceria[239]. While any strong mineral acid can be used, sulfuric acid and nitric acid are especially known to be effective towards ceria dissolution. As far as reducing agent is concerned, a green reducing agent like ascorbic acid, citric acid, oxalic acid, etc. would be very advantageous. Choosing the appropriate mineral acid and the reducing agent is paramount since mixing a mineral acid with reducing agents like H_2O_2 (which acts as a reducing agent under highly acidic pH conditions) is an exothermic reaction and hence deleterious.

Early work on ceria dissolution was reported in patents on cleaning ceria particles after polishing glass or silicon dioxide films with slurries containing ceria particles and other chemical additives. Mitani and Saito proposed compositions containing an acid and a reducing agent to clean ceria particles adhered to glass substrates after CMP[240]. Several reducing agents were tested in solutions containing sulfuric acid/nitric acid to enhance the dissolution of ceria particles. A solution containing 0.1 M HNO_3 and 1 M H_2O_2 yielded the highest dissolution rate. However, the pH of the solutions containing H_2SO_4/HNO_3 and H_2O_2 was very low (<0) and hence such compositions caused problems with subsequently deposited materials during IC fabrication and corroded the polymeric brushes used for post-CMP cleaning. Later, significant efforts were made to developing cleaning compositions that were compatible with the consumables (polymeric pads and brushes) used for post-CMP cleaning process. Avanzino and Shonauer proposed cleaning compositions containing a reducing agent (like phosphorus acid, hypophosphoric acid, oxalic acid and L-ascorbic acid) and a complexing agent (like ascorbic acid, citric acid, tartaric acid, malic acid and glutamic acid) for removing ceria particles on silicon dioxide and silicon nitride films [241]. In an embodiment of their invention, they showed that the dissolution of ceria particles increased with the increase in phosphorus acid and ascorbic acid concentrations chosen as prototype additives.

Of all the mineral acids, nitric acid and sulfuric acid are known to yield high dissolution rates [242]. The dissolution rate in the presence of acids increases with acid concentration. Temperature has a strong influence on dissolution and the dissolution rate increases gradually with the rise in temperature[243, 244]. In fact, several studies have reported an enhancement in dissolution rate by ~3-4 orders of magnitude between 20 °C and 90 °C. The surface of ceria reacts with H^+ ions in solution

and the particle surface area decreases due to the reduction in particle radius with time[242]. The dissolution of ceria in dilute HNO_3 or H_2SO_4 can be catalyzed by Pt NPs. Ultrasound energy can also boost the dissolution of ceria in various solutions[238]. pH has a significant impact on ceria dissolution and the dissolution is significant only below pH 5[245]. Dissolution rate of ceria, however is independent of mixing rate. The dissolution of ceria in nitric acid is controlled by chemical reaction and not by diffusion as the dissolution rate did not change with the mixing rate[244].

The dissolution of CeNPs depends strongly on the chemical composition. For instance, incorporation of 10% trivalent lanthanide ions increased the dissolution rate by an order of magnitude[243] as shown in **Figure 15a**. The crystal lattice weakening because of oxygen vacancies formed to balance the charge deficit after the incorporation of lanthanide ions was found to be the key reason for the increase in dissolution rate. Modification of crystal structure of ceria did not lead to any change in the dissolution rate. While increase in temperature and concentration of acid increased the dissolution rate by one and half orders of magnitude, respectively, changing the reducing agent did not have any impact on the dissolution rate as shown in **Figure 15a**. Beaudoux et al. showed that ceria particles can be dissolved at room temperature in a mixture of ascorbic acid and a dilute mineral acid[237]. The dissolution rate of ceria particles having a specific surface area of 15 m^2/g increased with the concentration of sulfuric acid or nitric acid in a solution containing 0.5 M ascorbic acid as shown in **Figure 15b**. Ceria particles having different specific surface areas i.e. different particle sizes showed significantly different dissolution rates [237]. Regardless of the different conditions employed, CeNPs were completely dissolved in 0.5M ascorbic acid and dilute nitric acid or sulfuric acid. A three-step mechanism is proposed for the dissolution process in ascorbic acid and nitric acid mixture. The first step involves the adsorption of reducing agent on the reactive Ce^{3+} surface sites on ceria. The second step is the reduction of Ce ions from Ce^{4+} to Ce^{3+} by the reducing agent and third step involves the release of Ce^{3+} species via Ce-O bound acid hydrolyses.

Recently, the dynamics of dissolution of CeNPs using in-situ liquid cell TEM coupled with high intensity electron-beam irradiation of nanoparticle dispersions[246] were studied. Very high dissolution rates, exceeding previously reported values at room temperature by several orders of magnitude were reported by the authors. It was suggested that the radicals, ions and electrons were generated by electron–water interaction and that these species assist in reductive dissolution of CeNPs. Several procedures have been demonstrated for recovering cerium from post-polish CMP

slurry. The recovery process involves selectively dissolving ceria in a mixture containing nitric acid and H_2O_2 [247-250]. Cerium from the solution is precipitated post-dissolution as cerium(III) carbonate which is subsequently converted into ceria by annealing in a rotary kiln. However, the dissolution rates reported in most of the studies are too low to consider any practical application.

Evidently, severe conditions are required to dissolve CeNPs. Published research suggests that sulfuric acid and nitric acid yield high dissolution rates than other mineral acids. There are many unanswered questions regarding this topic and hence there is still a need to understand the dissolution of CeNPs from a fundamental perspective. In particular, it is pivotal to study the effect of preparation method, particle size and surface coating, among other factors, on dissolution of ceria particles as the results of these experiments would provide some valuable insights relevant to dissolution of ceria particles used in commercial applications.

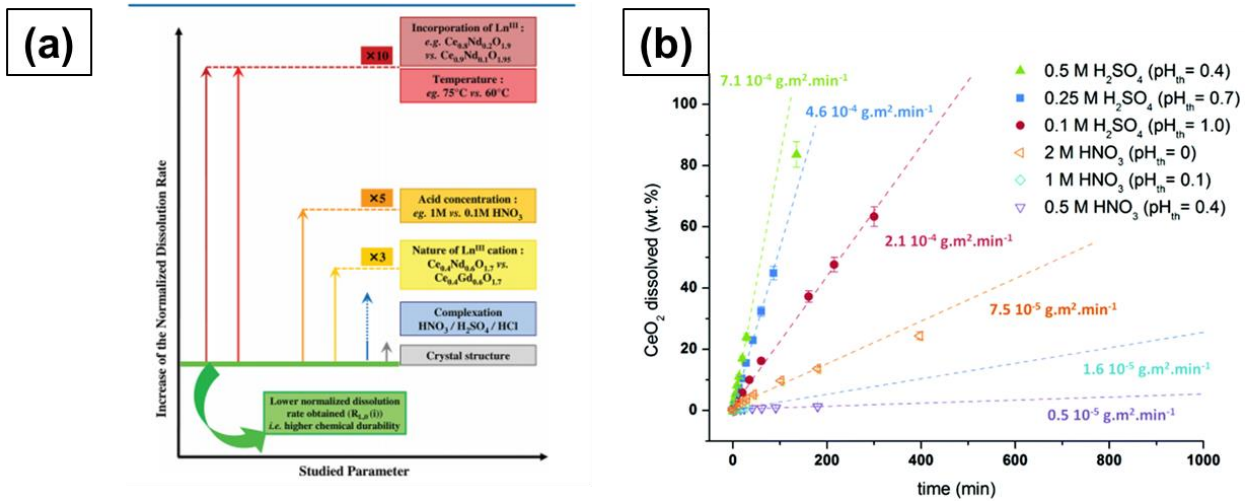

Figure 15. *(a) Effect of different physicochemical parameters on dissolution rate of $Ce_{1-x}Ln_xO_{2-x/2}$. Reprinted with permission from Ref [243]. Copyright 2012 American Chemical Society. (b) Effect of acid concentration on dissolution rate of ceria particles in a solution containing 0.5 M ascorbic acid. Reproduced from Ref [237] with permission from the Royal Society of Chemistry.*

3. Controlled synthesis of ceria-based hybrid nanomaterials

The synthesis conditions and the ability to control the surface properties are essential aspects influencing the morphology, crystallinity and surface chemistry of CeNPs, ultimately dictating their catalytic, redox and other functional properties. Variations in ceria surface have been obtained by incorporating of a variety of ligands or by binding or mixing them to form

composite hybrid structures with other molecules. The ceria nanocrystals size and variations in morphologies play a critical role in determining the surface oxidation states, the CeO_{2-x} stoichiometry, stability and catalytic performance.[73, 251] Various synthesis methods have been employed to tailor these properties, ranging from classical precipitation routes[252] to more advanced methods such as hydrothermal,[253] sol-gel[254] and microwave-assisted synthesis.[255] The selection of solvents and capping agents is also essential, particularly for achieving ultrasmall CeNPs. For example, ultrasmall (2.5±0.2 nm) mixed valence state (Ce^{3+}/Ce^{4+}) CeNPs have been obtained via a direct room temperature synthesis using ethylenediamine as a capping agent.[256] The ultimate choice of the method governs the size, shape and surface functions. Surface functionalization techniques including doping with other metals or metal oxides or organic ligands, surface oxidation/reduction treatments and deposition of metal NPs[257] allow for tailoring the surface chemistry and electronic structure to enhance catalysis activity, stability and dispersibility in various media. More recent advances include the use of green solvents and biosynthesis methods to produce less toxic NPs compatible with living tissues.[258] Furthermore, post synthesis treatments such as annealing, calcination or reduction can modify surface defects, oxygen vacancy concentration, and surface area, affecting redox behavior and reactivity.[259]

Such modifications generates novel interesting properties, allowing them to be used in a variety of applications. Many emerging applications of CeNPs in biomedicine, sensing and environment require surface functionalization to make them biocompatible for target binding and molecular recognition. However, the interfacial behavior of functional particles is sensitive to changes in the environment such as pH, ionic strength, temperature, natural organic materials, and concentration, often leading to aggregation[260] and many functionalized NPs exhibit differential behavior and reactivity profiles for practical applications. In this section, we highlight the most common strategies to create functional CeNPs and CeNPs-based hybrid materials (**Figure 16**). In particular, CeNPs used in conjunction with carbon-based materials, polymers, metal organic frameworks (MOFs), metals and metal oxides, and supramolecular assemblies are particularly attractive, due to their chemical structures, tailorability and synergistic properties, enabling effective utilization of these materials in applications.

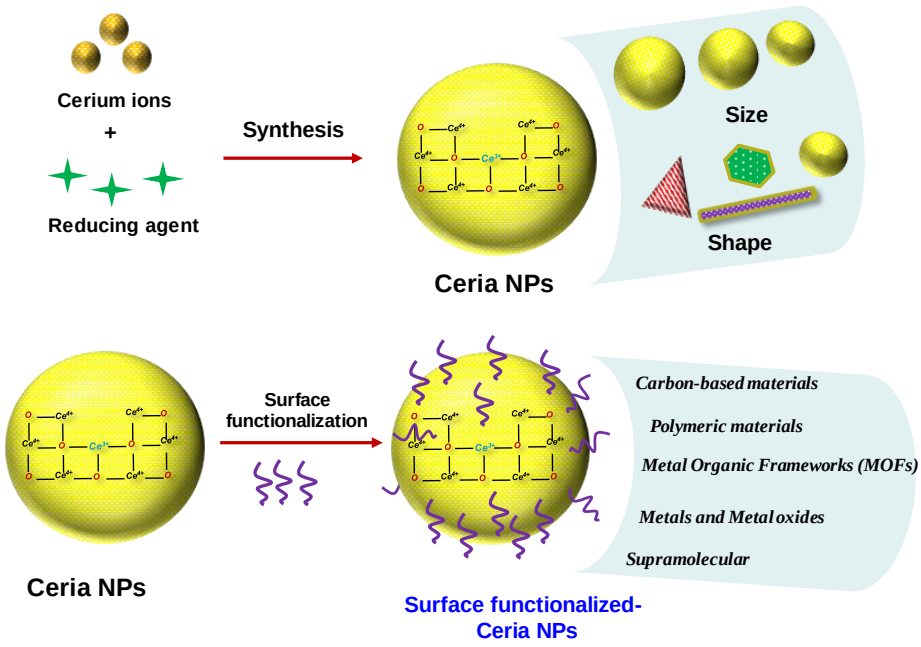

Figure 16*. Representation of the modular synthesis of CeNPs, with size and morphology control, and the surface functionalization and creation of hybrid structures with various types of materials.*

3.1. Ceria-carbon nanostructures

CeNPs stabilized on the surface of carbon-based materials such as graphene (GR), graphene oxide (GO) and carbon nanotubes (CNT) have enabled the design of a new class of hybrid two dimensional materials that combine the catalytic properties of the ceria with the large surface area and conductivity of carbon-based nanostructures. Graphene has been extensively studied due to its excellent electrical mobility, extremely large specific surface area, high thermal conductivity, and mechanical properties [261]. Two different procedures can be used to control the synthesis and graft CeNPs on graphene-based nanostructures. The first involves adsorption of the precursor salt on the surface of the graphene matrix followed by the *in situ* growth of the NPs with controlling the size and shapes. The second consists in the anchoring or deposition of the as-synthesized CeNPs onto the surface of the graphene matrix (self-assembly approach)[262]. CeO_2-graphene nanostructures synthesized using a single step (*in situ* growth) hydrothermal method demonstrated the ability to control growth of CeNPs on graphene sheets (**Figure 17**). The combination of defects in CeNPs with optimal amount of two-dimensional graphene sheets had a significant effect on the properties of the resulting hybrid, providing improved optical, photocatalytic, and photocapacitive performance[263].

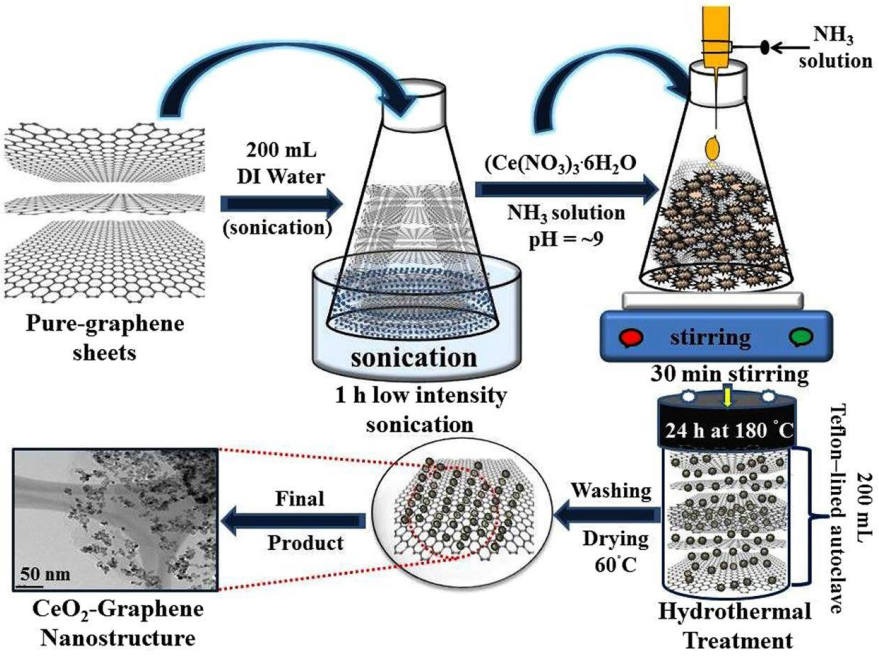

Figure 17*. Schematic representation for the synthesis steps of the CeO_2-graphene nanostructures. Reprinted from Ref.* [263].

The intercalation of CeNPs within the layers of graphene nanosheets allowed the nanosheets to maintain their high surface area and prevent reduced graphene oxide (RGO) from restacking [264]. Anchoring crystalline ceria onto RGO sheets revealed strong electrostatic interaction between the ceria NPs and the RGO. Therefore, the interaction of mobile holes and the increased density of the oxygen vacancies from Ce^{4+} to Ce^{3+} in the RGO resulted in an transforms in an n-type CeO_2 - RGO composites, suitable for applications in energy devices, batteries and sensors[265] Li et. al.[266] utilized an *in situ* growth method to synthesize a CeO_2-graphene nanocomposite, which showed a specific capacitance of 208 Fg^{-1} and a maximum power density of 18 kW kg^{-1} in supercapacitors. Dezfuli et. al.,[264] developed CeO_2-RGO nanocomposite electrodes which exhibited excellent supercapacitive behavior with high specific capacitance of (211 Fg^{-1} at 2 mVs^{-1} and 185 Fg^{-1} at 2.0 Ag^{-1}) and reversibility. Combining the redox characteristics of CeNPs with graphene is an effective approach to design materials for redox supercapacitors[266]. However, their wide band gap semiconductor (~3.4 eV), limits the use as an electronic material and photocatalyst[267]. Tuning the band structure by chemical functionalization or attachment to conducting supports is an excellent method to enable their implementation in electronic and optical applications. In particular, defects, such as oxygen vacancies, generate localized electrons on the CeO_2 surface, which may interact with the functional group in the RGO sheets, improving the properties of RGO[268]. Such composites

also show high adsorption capacities as adsorbent materials for preventing pollution of the environment with contaminants such as heavy metal ions and phosphates, enabling applications in environmental remediation[269]. To improve selectivity (towards cationic or anionic species), sorption capacity, and overcome limitations such as the leaching of the NPs or stacking of the C-sheets, the surface of these materials can be modified to enable specific applications. For example hydrous ceria modified graphene has been used as novel adsorbent for arsenic removal from aqueous solutions[270]. In other works, GO decorated with ceria showed selectivity in determination of trace metal ions and speciation for selenium. [271] Ceria-GO composites fabricated vis one-pot synthesis exhibited an almost complete (> 99.9%) and quick removal of arsenic species within 0.1 mg L^{-1} of the initial concentration[272]. Additional uses have been demonstrated for preparing ceria-carbon based catalysts for solid oxide fuel cells (SOFCs) and field effect transistors. The chemical vapor deposition (CVD) growth of single-walled carbon nanotubes (SWNTs) is normally performed at 800-1000 °C[273]. When CeO_2 , which stores oxygen, was used, the ceria-supported catalyst enabled the selective growth of SWCNTs on substrates due to the oxidative environment provided by the ceria[274].

3.2. Polymeric ceria-based hybrid materials

The combination of the metal oxide NPs with polymers is increasingly used to overcome limitations such as NP aggregation, dispersibility, lack of specificity for reactions in complex systems, and weak mechanical strength[275]. The properties of such hybrid materials depend on the nature of the guest NPs and the structure and the functional groups of the host polymer. This approach allows tuning the composition, surface functionality, and colloidal stability of the dispersed NPs. Colloidal carrier systems or so called smart carrier systems, such as thermosensitive microgels have been developed that encapsulate and stabilize the particles[276]. Polymeric materials are commonly used to stabilize CeNPs for applications in biomedicine. However, the surface charge and their surface functionalization have been found to play a critical role in their uptake mechanism and subcellular localization. Results with CeNP functionalized with different polymeric coatings (poly(acrylic acid), aminated poly(acrylic acid or dextran, *Figure 18*), endowing positive, negative or neutral changes, showed that CeNPs with a positive or neutral charge enters most cells, while those negatively charged internalizes mostly in cancer cell lines[277].

In other works, polymers like polyethylene glycol and polyvynilpyrrolidone create functionalized CeNPs with biocompatible coatings that show enhanced autophagic clearance[278]. Recent advances in the surface functionalization of ceria involves green synthesis methods using room-temperature aqueous and solvent free solutions. CeNPs prepared by metal-free organocatalyzed photoinduced electron transfer radical polymerization (O-PET-ATRP) generated zwitterion-functionalized NPs that retained shape and prevented protein adsorption. The resulting passivation of the particle surface generated higher uptake and enhanced redox properties in physiological conditions. The functionalization using this environmentally friendly approach directly enhanced intracellular delivery for cancer therapeutics[279].

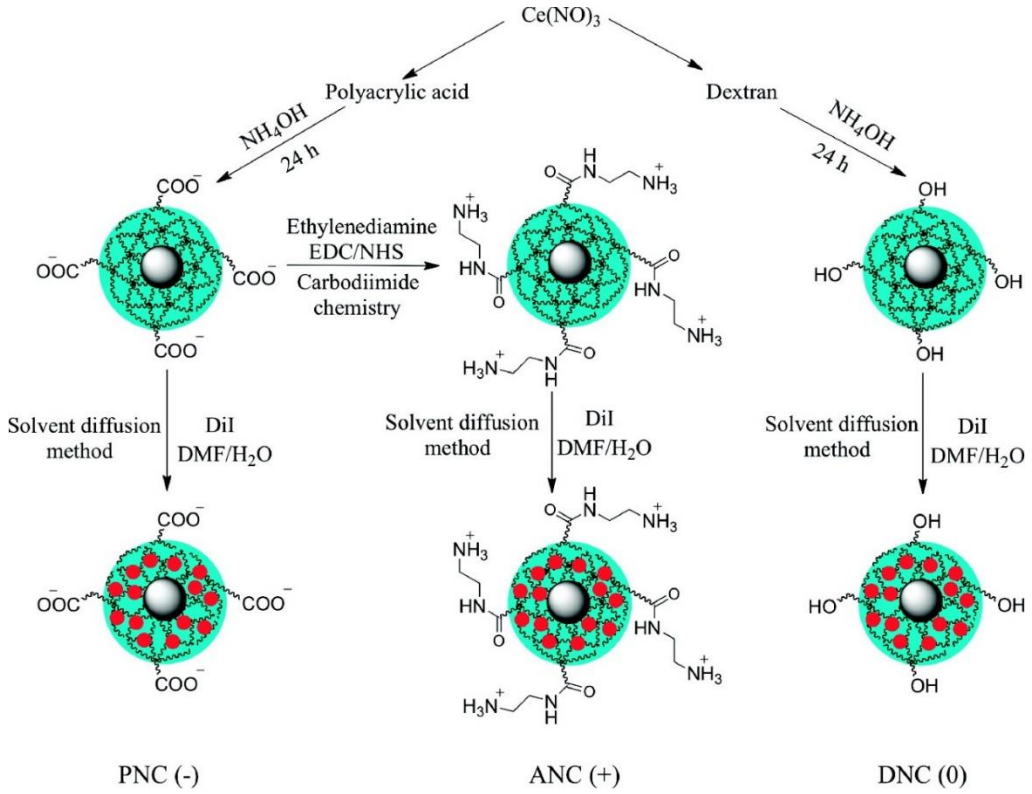

***Figure 18**. Surface functionalization of ceria NPs with different polymer coatings and surface modifications were synthesized to yield nanoparticles with negative [PNC(−)], positive [ANC(+)], and neutral [DNC(0)] charge where PNC is poly(acrylic acid), ANC is aminated poly(acrylic acid and DNC is dextran. A fluorescent dye (DiI, red circle) was encapsulated using a modified solvent diffusion method (reprinted with permission from Ref [277]. Copyright 2010 American Chemical Society).*

Polymers can also be used to fabricate hybrid CeNPs-polymer composites in which the polymer acts as a supporting material or dispersing agent. CeNPs can also be crystallized in a

controlled manner on the surface of polymer NPs[280]. Hybrid polymeric core–shell nanoparticles i.e., CeNPs/polystyrene nanocapsules containing a model fluorophore with encapsulated fluorescent dyes were developed by free radical microemulsion polymerization[281]. The use of CeNPs generated a significant enhancement of the fluorescence properties by suppressing the quenching of the encapsulated dye by molecular oxygen. Cellulose, a sustainable and renewable biopolymer was used to incorporate CeNPs to obtain transparent films with UV shielding properties[282].

Other studies have shown the use of coordination polymers employing lanthanide ions instead of *d*-block metal ions to generate supramolecular architectures with distinctive structures and accessible metal coordination sites[283, 284]. Using a sonochemical method, NPs of a Ce(III) supramolecular compound with fluorescent proepties has been synthesized as a precursor for nanoceria[285]. Polymeric materials can be used to facilitate the self-assembly of NPs and create structured supramolecular assemblies[260, 286]. The surface of CeNPs has been shown to form stable surface complexes with molecules incorporating phosphate, phosphonate, or carboxylate moiety.[287] Several reports demonstated synthesis of CeNPs using coordination polymers with tunable shell tickness and surface functions[284, 288-290].

3.3. Ceria-based Metal Organic Frameworks

Metal-organic frameworks (MOFs) have emerged as a promising class of materials for gas storage, gas purification and separations, and catalysis[291]. The large number of organic linkers and metal ions provide versatility for creating tailorable structures with open metal sites that can act as catalytic or binding sites for a variety of reactions. Stabilizing CeNPs within MOF frameworks can be used as an effective strategy to enhance their reactivity by preventing aggregation and providing high accessibility to the catalytic sites through the open channels. A cerium-MOF based on MIL-125 with open-metal sites,[292] was shown to retain porosity and enhance the overall adsorption of SO_2 and CO_2. Synthesis of Ce (IV) based UiO-66 (referred to as Ce-BDC) with different pore sizes and functionalities was reported to stabilize the $[Ce_6O_4(OH)_4]^{12+}$ cluster during MOF formation preventing metal-hydroxo precipitation[293, 294].

Several studies have been reported on introducing Ce to the MOF framework by doping to increase the number of active sites for gas adsorption. Ce-doped MOF ((Ce-UiO-66(Zr)) exhibits

over 25% increase of the amount of NO_2 adsorbed, in dry conditions, in comparison with the unmodified MOF[295]. Support materials or core shell structures have been shown to improve the catalytic activity of CeNPs[296]. Kim *et al.*[297], developed a simple method to synthesize nanoporous CeO_2 by the thermal conversion of aliphatic carboxylate ligand-based Ce-MOF into hierarchically metal oxides with nanocrystalline frameworks. It was found that the pore size of the prepared framework could be tuned providing an increase in the adsorption capacity. A 3D network CeO_2-M was prepared by a Ce-MOF-template method and K^+ doping which resulted an increased oxygen species and superior adsorption and oxygen storage capacity of ceria. [298]. The solid catalyst was evaluated for *o*-xylene oxidation at low temperature. Inspired by these studies, a new generation of porous CeNPs/Au@SiO_2 core–shell nanocatalysts have been prepared by the pyrolysis of Ce-based MOFs (**Figure 19**)[299]. The CeO_2/Au@SiO_2 catalysts possess a porous nanotube structure, resulting in high catalytic activity for the reduction of 4-nitrophenol.

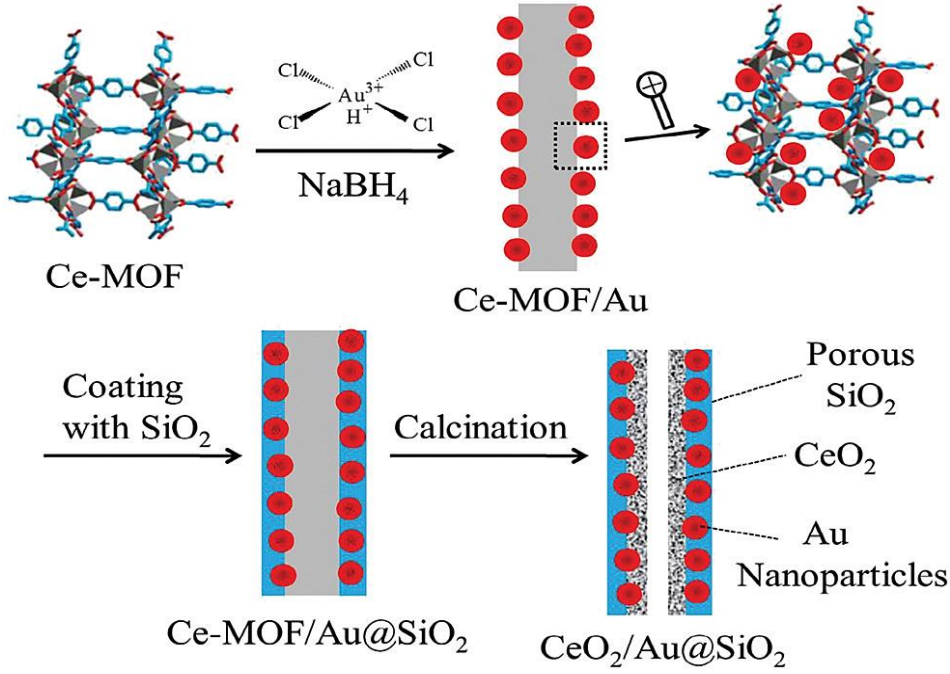

***Figure 19**. The synthesis procedure for CeO_2/Au@SiO_2 nanocomposites. Reproduced from Ref. [299] with permission from the Royal Society of Chemistry.*

Enhanced reactivity of CeNPs can be obtained by creating ultrasmall (1-2 nm) CeNPs within a Ce-MOF via in situ etching of the parent NPs (**Figure 20**). This strategy enhanced the activity of the CeNPs by preventing NP aggregation, stabilizing them in a dispersed form within the porous framework[300]. At the same time, the guest molecule has high accessibility to the active sites

through the porous network. The resulting CeNPs-MOF showed fast degradation kinetics of the nerve agent, p-nitrophenylphosphate (DMNP) providing superior activity as compared to the parent CeNPs. The ability of the CeO_2-MOF to degrade DMNP was explained by the increased abundance of Ce^{3+}/Ce^{4+} neighboring sites and oxygen vacancies, facilitating the nucleophilic attack of the hydroxyl groups of the DMNP phosphate, leading to P-O bond cleavage and further degradation. This method provides a strategy to enhance the reactivity of CeNPs making them more effective catalysts.

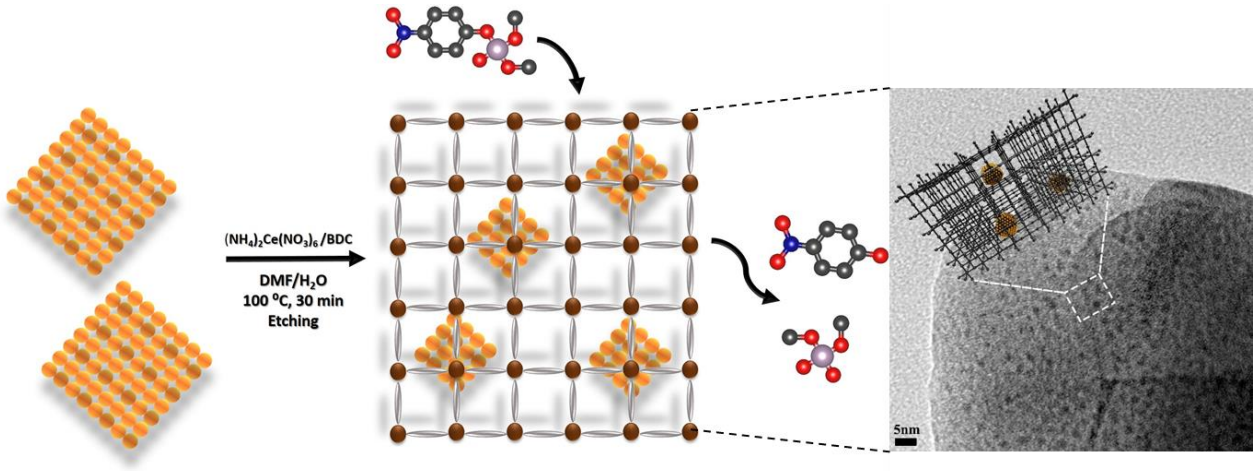

Figure 20. *Schematic of CeNPs immobilization inside Ce-MOF for DMNP degradation and the subsequent CeNP –MOF structure analysed by TEM (Reprinted with permission from Ref [300]. Copyright 2020 American Chemical Society).*

3.4. Ceria-based-metals and metal oxides heterostructures

Noble metals (M) and metal oxides (MO) can be used in conjunction with CeNPs to create hybrid materials with lower cost and superior characteristics for applications. For example, platinum-group metals, Pd, Rh and Pt, serve as active species in TWA exhaust catalysts and the price of these metals represents around 40% of the manufacturing cost of the catalysts[301]. To reduce the use of expensive Pt Pt-MO heterostructures have been explored. Enhanced activity can be obtained by encapsulating noble metals inside ceria, e.g. Pt@CeO_2 core-shell hybrid structures, or by loading the MNPs on the surface of hollow CeO_2 nanostructures. This strategy has been used to create a variety of Au, Pt, Ag@ CeO_2 hybrid nanostructures[302, 303], providing enhanced catalytic activity by stabilizing small size noble metal NPs and creating hybrid junctions at the two-phase

interface[304]. Doping CeNPs with metals has emerged as a promising approach to produce supported catalysts with atomically dispersed metals[305]. The size, morphology, stability and catalytic activity of these materials can be controlled by varying the dopant, ligand used and the reducing and oxidizing conditions. Studies to assess the effects of metal dopants on the reducibility of bulk and extended surfaces of CeNPs with have been extensively reported using both experimental and theoretical approaches[142, 158, 306, 307].

The enhanced properties provided by these hybrid materials have found unique applications in catalysis, environmental remediation, sensing and biomedicine. For example $Ag@CeO_2$ have demonstrate inactivation of *Escherichia coli* through the formation of reactive oxygen species (ROS)[308]. Similarly CeO_2-CdO binary metal oxide nanocomposites showed antibacterial activity and growth inhibition towards *P.aeruginosa*[309]. The properties of CeNPs were also integrated with the photoinduced electron transfer of quantum dots (QDs), providing materials with significantly improved optoelectronic properties. A synthesized ceria-carbon quantum dots/RGO nanohybrid showed improved photocatalytic properties enabling rapid decomposition of organic pollutants[310].

4. Applications and future directions

The unique properties of nanoscale ceria quickly inspired their translation in a variety of applications. The broad applicability and versatility is a consequence of the CeNPs's redox properties originating from the presence of oxygen vacancies and the Ce^{3+}/Ce^{4+} mixed valence states. As a result CeNPs are increasingly used in applications such as catalysis, chemical mechanical polishing, fuel cells, oxygen sensors, ultraviolet absorbents, sensing and biosensing, drug delivery and bio-medical diagnostics[311-316]. In the following sections we provide examples of representative use cases of CeNPs in catalysis, chemical mechanical polishing, chemical sensing and biosensing, and environmental remediation.

4.1. Catalysis

The thermal stability electron, high OSC and proton transfer abilities make CeNPs particualrly useful in catalysis[165, 317]. The $3^+/4^+$ reversibility and oxygen mobility, which is higher compared with other oxides such as SiO_2, Al_2O_3, and ZrO_2, enable the use of CeNPs as a catalyst in redox, CO oxidation, and acid-base reactions[3, 318, 319]among others. Main concerns related to CeNPs are related to the deterioration of the active surface area due to sintering and segregation processes resulting in loss of catalytic activity[320]. Therefore, much attention has been paid to developCeNP-based catalysts with enhanced structural characteristicsto resist degradation, such as combining binary metal oxide catalysts. For example, CeO_2-MnO_2, showed enhancxed performance for processes such as CO oxidation[321], selective catalytic reduction of NO_x with NH_3[322], and oxidation of volatile organic compounds[323]. Further optimization has been accomplished by using a Ce-based MOF to maximize the exposed active sites and enhance the porosity of the system[324]. Ceria is an excellent support for high-performance metallic catalysts, enhancing stability and catalytic performance as shown for example with PtFe nanocrystals hybridized by CeO_x, e.g. PtFe-$Pt_xFe_yCe_zO_j$.[12] A particular case is the use or mesoporous ceria, characterized by well-defined pores, typically ranging from 2 to 50 nm, and a high surface area which provides unique capabilities for catalysis,[325] gas sensing and energy storage. The high surface area provides enhanced accessibility to active sites and facilitates transport of reactants and products. Additionally, the oxygen vacancies facilitate switching between CeO_2 and CeO_{2-x}. Therefore they showed improved performance in catalytic reactions including oxidation, hydrogenation and pollutant removal. A review summarizing synthesis and catalytic applications of mesoporous ceria can be found in Refs.[325]

Doping CeNPs with transition metals or rare earth metal such as Cu, Cr, Ti, Y, and La, have been adopted as a promising approach to tune the catalytic activity of these materials[326-330]. The substitution process causes structural defects and creates more oxygen vacancies on the catalyst surface, which affects the generation and mobility of charged species such as electrons and oxygen anions. Furthermore, doped ceria can also tolerate high temperature annealing treatments due to the cooperative nature of the cations of the binary oxides[331]. The electronegativity and ionic radius of Ce^{4+}, are 1.12 and 0.97 Å, respectively. A synergetic dopant would ideally have electronegativity and ionic radius close to these numbers. For instance, samarium (Sm) has an electronegativity and ionic radius of 1.17 and 1.07 Å, respectively. It is also soluble in the ceria sublattice and can stabilize the fluorite structure of ceria at low dopant concentration. A

nanocrystalline CeO_2–Sm_2O_3 (CS) solid solution, has been easily synthesized yielding a promising catalyst for the oxidation of CO at lower temperatures owing to the large number of lattice defects, high OSC and improved redox properties[331]. Sm-doped CeO_2 nanopostructures have been widely used as a catalyst in methane selective oxidation[332], allylic oxidation[333] and fuel cells applications[334], while Gd-doped CeO_2 was used for gas sensing applications[335]. The Gd-doped CeO_2 gas sensor had better sensitivity, good stability and lower operating temperature over nondoped one with a detection concentration of 800 ppm CO_2 gas. In addition, Ni-doped CeNPs have been hydrothermally prepared and showed an increased magnetization and electrical conductivity with increasing the dopant concentration[336].

As diesel emission produces soot which have grown concerns on human health and the environment, several emission control strategies have been implemented to reduce environmental impact[337]. For example, over 90% of the soot can be trapped and then be continuously or periodically combusted to CO_2 using the diesel particulate filter (DPF) technology. However, the periodic regeneration of DPF is not passive, which makes it complex and expensive. Ceria-based materials have been developed to decrease the soot combustion temperature (~600 °C compared to diesel exhaust temperature (~175–400 °C)) and have been extensively studied as catalysts and catalysts promoter in this research area[338]. Nascimento *et al.*[339] studied the performance of binary oxides CeO_x/FeO_y catalysts modified with AgNPs for the control of diesel soot combustion. Catalytic tests showed a significant reduction of about 300 °C in the soot oxidation temperature with CeO_x/FeO_y compared to the CeO_2. Shen et al.[340] also investigated the catalytic performances of Fe-doped ceria catalysts with diffeent Fe contents for the soot oxidation reaction with O_2 or O_2/NO gases. They demonstrated that the addition of iron increased the number of oxygen vacancies on the surface, and therefore the catalytic activities for NO oxidation and NO_2-assisted soot combustion.

Uniform anchoring/decoration of CeNPs on the surface of graphene sheets improves the photocatalytic and photocapacitive performance of the nanostructures for effective charge transfer and catalytic degradation processes [263]. For example, the photocatalytic activity was examined by monitoring their ability to degrade Congo red ~94.5% and methylene blue dye ~98% under visible light irradiation. These developments indicate the borad applicability of CeNPs-based nanostructures for future energy and environment-related applications.

4.2. Chemical mechanical planarization (CMP)

CMP is a surface smoothing process that is used in semiconductors fabrication process and in a number of other manufacturing processes. It has become a critical and enabling process for the multilevel metallization necessary for interconnecting the immense number of active devices created on silicon substrates and in the device fabrication process sequence at the gate level[312, 341]. Silicon dioxide CMP, or simply oxide CMP, in which a colloidal slurry consisting of ceria abrasives is commonly used, is one of the many critical processes in the fabrication of integrated circuits (ICs)[341-344]. CeNPs are widely used as abrasives for oxide CMP since they interact strongly with the oxide leading to high removal rates (RRs). With appropriate additives to ceria slurry, it is possible to achieve a highly selective polishing of the oxide with respect to the underlying silicon nitride films as required in the planarization of shallow trench isolation structures[344-346]. Ce^{3+} species present on the surface of CeNPs particles react with the hydrated oxide surface ($Si\text{-}O^-$) forming strong Ce-O-Si bonds and ultimately rupturing the underlying and weaker bonds in the oxide film leading to its continual removal[344, 347, 348]. There are extensive discussions of the reaction mechanisms involved in the polishing of oxide and nitride films[344, 349, 350].

Two methods, namely solid-state displacement and solution-growth, are commonly used for the preparation of CeNPs particles for CMP applications[341, 351]. In the solid-state displacement method, particles are prepared by calcining cerium carbonate at more than 600 ^oC under controlled air flow conditions, which is subsequently wet milled to obtain the desired particle size [352]. CeNPs with less than 100 nm size can be obtained by controlling the pre-treatment of cerium salt, calcination temperature, air flow conditions, and bead size of the milling process[352-354]. However, the particles produced by this method are faceted and have sharp edges, corners, and apexes as well as a very wide size distribution (**Figure 21a**). These features tend to scratch the films during polishing and generate many unacceptable defects. Consequently, the usage of these types of particles is being avoided, while the solution-grown CeO_2 particles, despite of their higher cost and potential for contamination, have gained wider acceptance[87, 355, 356].

In the solution growth method, cerium hydroxide ($Ce(OH)_3$) is precipitated from a solution of cerium nitrate mixed with ammonium hydroxide, and transformed to CeO_2 in the presence of oxygen ($Ce(OH)_3 + 1/2O_2 \rightarrow CeO_2(s) + 3H_2O$). These particles are separated and washed repeatedly for removing residual precursors until the desired conductivity of the suspension is

obtained[357, 358]. Particles with a very narrow size distribution can be produced by this method as shown in **Figure 21b**. These relatively uniform-sized CeNP abrasives have polyhedral and nearly spherical shape that is expected to minimize the generation of scratches because of fewer sharp edges and corners.

Coating ceria abrasives with a layer of different materials and chemical compositions makes it is possible to change the physicochemical properties of the core abrasive, including shape, surface chemistry, surface charge, porosity, and hardness and can be tailored to increase their reactivity with films. To benefit from this strategy, core/shell type CeO_2 abrasives have been investigated and showed increased removal rates as well as improved surface roughness of polished oxide films. Core/shell structured composite particles, comprising of mesoporous silica[359, 360], dendritic silica[361], polymethylmethacrylate (PMMA)[362], and polystyrene (PS)[363] as core materials with metal-doped CeO_2 particles making up the shell, generated relatively high oxide removal rates with low surface scratch and roughness values. This was ascribed to the resilient spring-like effect of the softer core silica during polishing. Also, since smaller particles tend to produce a higher quality surface finish, coating of core CeO_2 particles (~100 nm) with a layer of smaller (5 nm or so) CeO_2 shell has been proposed and was shown to achieve high oxide polish rates (**Figure 21c**)[364]. In principle, these types of composite abrasives can result in significant cost savings for high volume manufacturing due to higher throughput, lower abrasive concentrations, and lower waste treatment cost. However, all these composite ceria abrasives are prone to form broken particles as well as peeling-off and/or brittle collapse of the shells. Therefore, further advancements in the field are necessary to avoid these issues. Various types and shapes of pure and composite CeO_2 particles used in most CMP slurry formulations are summarized in **Figure 21d**.

As NAND technology has evolved from 2D planar to 3D vertical, new CMP steps with higher planarization efficiencies and much higher oxide polish rates have become necessary. This is due to the larger initial step heights and much thicker dielectric layers than in conventional ILD or STI CMP[365-367]. To meet these challenges, CeNPs based slurries having the necessary very high oxide polish rates need to be developed. One of the current development approaches is to prepare Ce^{3+}-rich CeO_2 particles through either metal-doping or coating. Doping with lanthanide (La, Sm, Gd, Nd, and Yb) elements increases Ce^{3+} concentration by increasing oxygen vacancies at the surface, thus enhancing the removal rates of the oxide film[368-370]. Praveen et al. reported that La-

doped CeO_2 particles showed ~20 % higher removal rates of SiO_2 films when compared to the non-doped CeO_2 particles[368]. Similarly, Cheng et al. showed that Nd doping increases Ce^{3+} concentration on the particles surface and thus produced ~30 % higher removal rates of the oxide film at pH 9.5[369]. The removal rates of oxide films were well correlated with Ce^{3+} concentrations in metal-doped particles. For example, Feng et al. prepared single-crystal Ti-doped CeNPs spheres with a size distribution of 50-150 nm through liquid-phase flame spray pyrolysis of solutions of cerium and titanium precursors[371]. The CeO_2 core of the particles were encapsulated by a 1-2 nm shell of TiO_2 to minimize the surface energy, resulting in a nearly spherical morphology (**Figures 21e-g**). The polishing results showed that these particles reduced the CMP-caused defects by 80 % and increased the removal rates of the oxide film by 50 %[371].

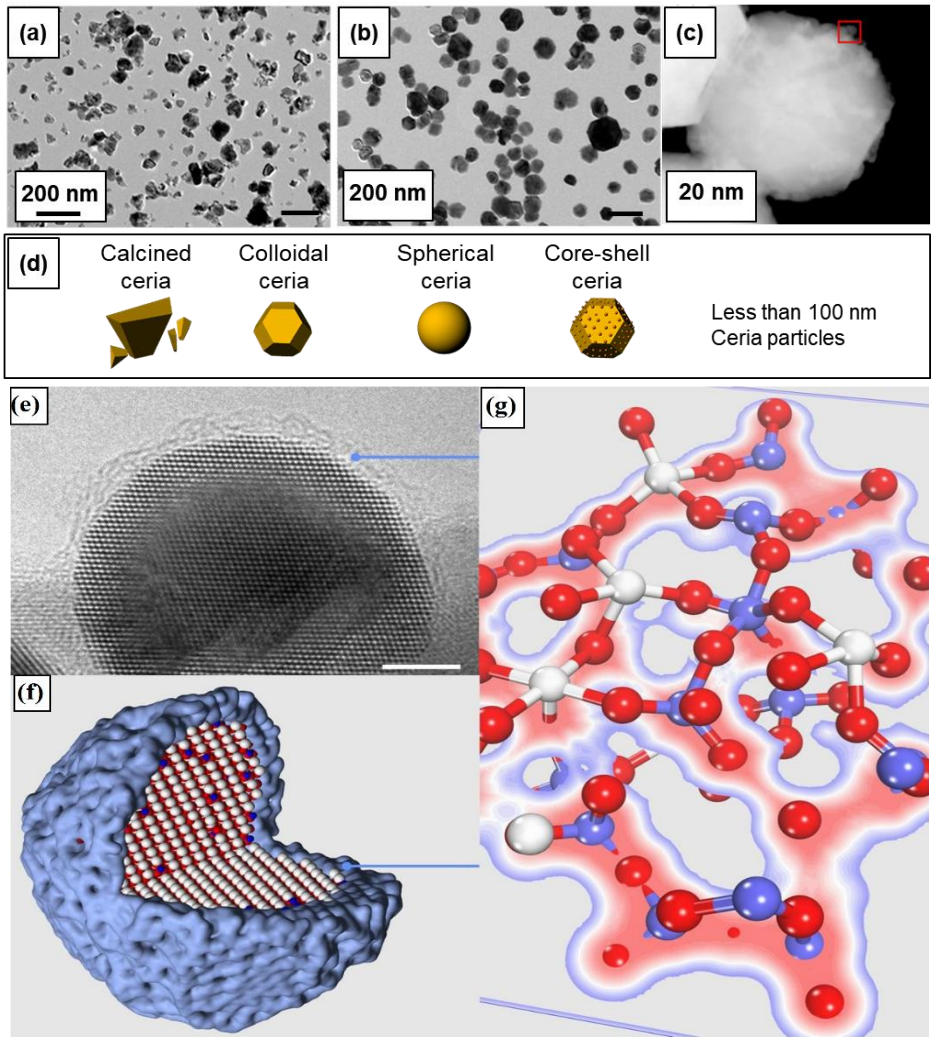

Figure 21. *Different types of CeNPs used in recent CMP slurries; (a) calcined ceria, (b) colloidal ceria, and (c) core/shell ceria particle, and (d) their schematic illustration. HRTEM image of Ti-doped ceria single-crystalline nanoparticle (e), model of a Ti-doped CeO_2 sphere (f), and a molecular model of the TiO_2 amorphous shell on the nanoparticle (g). (a) and (b) reprinted with permission from Ref [351].Copyright 2014 American Chemical Society.(c) reprinted with permission from Ref [364].(e-f) reprinted with permission from Ref [371].*

4.3. Chemical and biological sensing

The field of chemical sensors and biosensors has witnessed a radical transformation due to the rapid advancement and innovations in functional materials and biomaterials. Metal oxide nanomaterials can serve for both recognition and transduction purposes,[372] alone or in conjunction with biomolecules such as DNA or enzymes. Enzyme-based sensors are considered to be one of

the most reliable sensing techniques due to their high sensitivity, selectivity and fast response[373-375]. However, enzyme's stability can be severely compromised with temperature and pH changes. For these reasons, researchers have focused on using nanotechnology tools to develop more robust sensors by engineering materials that mimic the function and complexities of natural enzymes[376-379]. Metals and metal oxides NPs and nanocomposites[374, 380, 381], metal organic frameworks[382, 383], and carbon-based nanomaterials[384-386] have demonstrated promising potential as artificial nanoenzymes[195] with peroxidase or oxidase-like mimetic activity, that could be used as receptors or transduction materials for sensing.

CeNPs have emerged as a promising enzyme-mimetic material that possesses intrinsic oxidase or peroxidase-like properties, due to the mixed oxidation states (Ce^{3+}/Ce^{4+}), which provides the ability to catalyze many chemical and biologically relevant reactions [375]. Upon reduction of Ce^{4+} to Ce^{3+}, the CeNPs mimics catalase activity by inducing H_2O_2 oxidation, generating molecular O_2. On the reverse, oxidation of Ce^{3+} to Ce^{4+} mimics superoxide dismutase (SOD) activity by reducing $O_2^-$to H_2O_2. The efficiency of CeNPs as a peroxidase mimic is strongly dependent on the low ratio of (Ce^{3+}/Ce^{4+})[387]. The high catalytic activity, oxygen rich surface and low toxicity[175] make them excellent candidates for enzyme-mimetic and enzyme immobilization purposes.[229, 388] Furthermore, CeNPs have been used as a material with therapeutic potential to reduce harmful ROS/RNS due to the unique regenerative ability to scavenge ROS/RNS species[200, 389]. The combination of sensing and therapeutic functions makes CeNPs a powerful theranostic platform for biomedical applications.[26, 390] A ROS-scavenging tissue adhesive nanocomposite was synthesized by immobilizing ultrasmall ceria nanocrystals on the surface of uniform mesoporous silica (MSN)[391]. The ceria nanocrystals decorated MSN does not only have a strong tissue adhesion strength, but they also help minimizing the ROS-mediated deleterious effects efficiently accelerating the wound healing process as evidenced by marked skin appendage morphogenesis and limited scar formation.

Various studies have shown the ability of CeNPs to reduce symptoms of oxidative stress-related diseases, such as chronic inflammation[392], endometriosis[393], cancer[394, 395], and diabetes[396, 397]. However, with the diversity of methods and synthetic procedures used to synthesize these particles, each producing different types, shapes, sizes, coatings and Ce^{4+}/Ce^{3+} ratios, the antioxidant effects can vary significantly. Controlling the surface chemistry to efficiently regulate reducing and oxidizing efficiency (e.g. antioxidant *vs* pro-oxidant) in biological systems remains

a challenge, as is the tendency of CeNPs to agglomerate in biological fluids [170]. In some cases, CeNPs have been found toxic, but the mechanism responsible for CeNPs toxicity - if present - is still inclear and subject to debate[11]. Therefore, it is important to develop new kinds of CeNPs with highdispersibility and enhanced catalytic activity that are able to maintain their redox properties in biological fluids. Several strategies have been reported in literature to improve these properties. For example, CeNPs have been coupled with materials such as Cu_2O[398], TiO_2[399], and Eu[400, 401] to enhance catalytic and enzyme mimetic properties. The use of CeNPs in conjunction with TiO_2 nanotubes increased the peroxidase mimetic activity.[402] In another study, adding Eu to the nanocrystal structure imparted fluorescence and increased the oxidase-like activity of ultra-small (2-5 nm diameter) CeNPs[400]. Decoration of graphene sheets with metal oxide NPs such as CeNPs have improved the mechanical, electrical and thermal properties of both materials. In this hybrid structure, CeNPs have a wide band gap (3.4 eV) with a high isoelectric point (IEP, 9.0) and excellent enzyme binding ability [403], while graphene has high electrical conductivity. Therefore, CeNP-graphene composites that synergistically combine the electrical conductivity of graphene with the catalytic properties of CeNPs are excellent materials for electrochemical biosensors. CeNP-reduced graphene oxide (CeO_2-rGO) composite prepared by a facile one-pot hydrothermal method used in combination with horseradish peroxidase (HRP) enabled detection of H_2O_2 at very low levels. The CeNPs-rGO composite provided a well-defined micro-environment for HRP immobilization and enhanced the direct electron transfer (DET) between the enzyme and the CeO_2-rGO at the electrode surface, significantly improving performance for H_2O_2 detection. Other works reported a 100-fold increase in the oxidase mimicking activity of naked CeNPs particles by fluoride capping. This mechanism has been used for ultrasensitive sensing of fluoride (0.64 μM).[404]

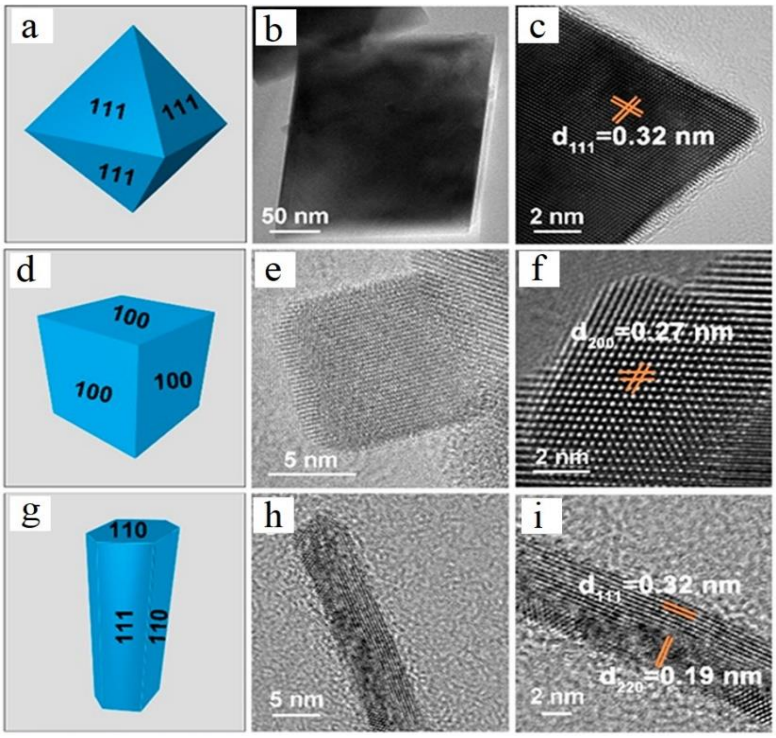

***Figure 22**. CeO_2 with different shapes and exposed facets (a-i), and H_2O_2 detection scheme using HRP/CeO_2-rGO modified glassy carbon electrode (j). Reprinted with permission from Ref [405]. Copyright 2022 American Chemical Society.*

Hybrid nanomaterials offer several advantages for chemical sensing and biosensing due to their ability to provide synergistic catalytic functions due to formation of hybrid junctions associated with rich redox reactions, enhancing their catalytic performance[373]. Artificial intelligence and machine learning, through the use of computer-aided designs of the CeNPs, could in the future be used to screen and rationally design particles with the desired properties for applications[406, 407]. Using these tools, it is now possible to predict the optimal CeNP shape that delivers the best catalytic performance in some specific reactions[406]. For instance, facet engineering of CeNPs with the help of computational calculations made it possible to understand the crystal facet effect that plays a crucial role in determining the surface energy and reactivity[408]. CeO_2 nanorods with a dominant (110) facet showed the highest peroxidase-mimetic activity due to the rich defect chemistry on their surface (**Figure 22**). These studies provided an increased understanding of the fundamental CeNPs properties that drive their unique reactivity. This knowledge is essential to rationally design and tailor their activity.

Several types of chemical and biological sensing systems where CeNPs have been used as receptors for gases, enzyme mimetic materials, co-catalyst or as a label for quantifying affinity

recognition reactions have been developed (**Figure 23**). Applications include gas, biomimetic or enzyme-based sensors, immuno, aptamer and DNA based sensors. Examples for each of these classes are discussed in the section below.

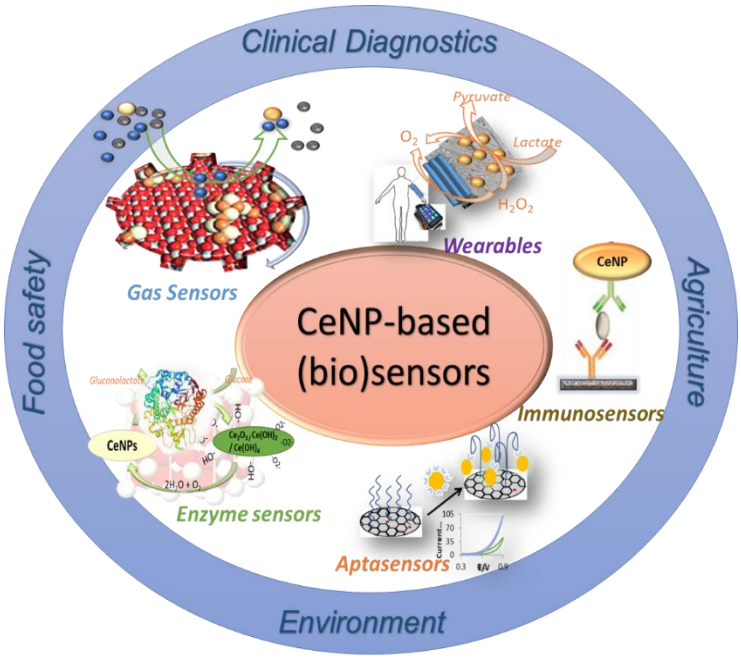

***Figure 23**. Summary of chemical sensing and biosensing involving CeNPs-based materials and their applications.*

4.3.1 Gas sensing

Semiconductor metal oxides are well known candidates for gas-sensing applications due to their high sensitivity for the adsorption of gases[409]. The gas-sensing mechanism is based on the adsorption of target molecules, generating changes on the material's conductivity at the oxide surface, though a dynamic process mediated by oxygen vacancies and subsurface defects[410]. In many such applications, the CeNPs are typically used as a support for metals like Pt or Au. CeNPs-based sensors have been designed for detection of carbon dioxide[411], acetone[412], nitrogen dioxide and sulfur dioxide[413]. Because the electrical conductivity of CeNPs is a function of the oxygen partial pressure, ceria-based NPs, nanostructures and thin films can be used as oxygen sensors.[414] Nanostructured ceria also showed response towards different humidity levels and therefore can be used to fabricate humidity sensors, by measuring the resistance variation upon exposure to moisture[415]. High surface area truncated octahedral CeNPs with a higher level of Ce^{4+} ions exhibited the highest humidity sensing with a response time of 10s.

Highly porous yolk-shell CeNP nanospheres prepared by microwave assisted solvothermal synthesis showed a two times increase in sensitivity for CO_2 detection as compared to commercial CeNPs (**Figure 24**) due to increased porosity and permeability for gas adsorption though the hollow structure[411]. Similar structures were used to build sensors for acetone, with detection in the ppm concentration range, and a response and recovery time of 6 and 11 s, respectively[412]. Doping of CeNPs with lanthanum was shown to strongly influence the redox (Ce^{3+}/Ce^{4+}) ratio and gas adsorption properties for CO. In optimized conditions the sensor provided fast response at a temperature of 380 ^{0}C under CO exposure associated with Ce^{4+} reduction and vacancy generation[416].

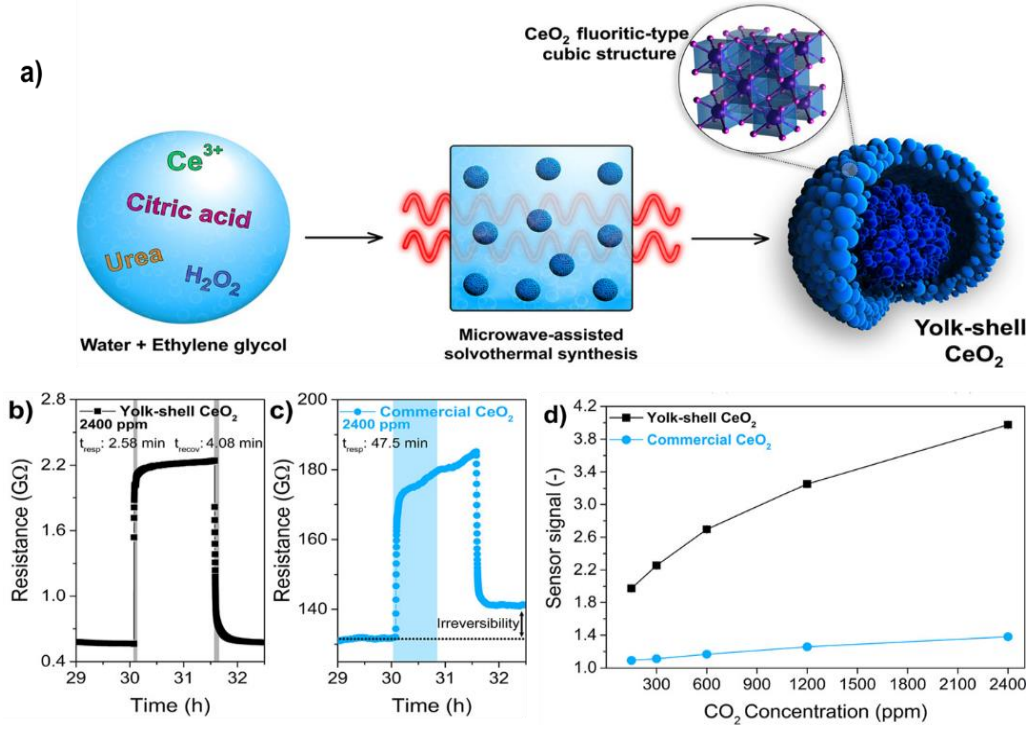

***Figure 24**. Microwave-assisted solvothermal synthesis of yolk-shell CeNPs (a), response and recovery times to 2400 ppm of the sensor prepaid with yolk-shell CeNPs (b) as compared to the commercial CeNPs (c), and comparative sensor signal in response to CO_2 concentrations (d) (Reprinted with permission from Ref [411].Copyright 2020 American Chemical Society).*

4.3.2 Enzyme mimetics and enzymatic biosensors

CeNPs have been widely investigated to fabricate enzyme mimetic and enzyme-CeNPs-based biosensors with colorimetric or electrochemical detection[224, 417]. These sensors are using CeNPs either as an enzyme mimetic (e.g. as a synthetic replacement of a natural enzyme)[418], or co-immobilized with a natural enzyme to catalytically amplify enzymatic reactions[419] and therefore

enhance their detection sensitivity. As compared to systems based solely on biocatalytic enzymes (e.g. oxidases or peroxidases), sensors based on CeNPs are more robust, inexpensive and not susceptible to denaturation.

Sensors with optical detection measure changes in optical properties associated with redox processes at the CeNPs surface. It is known that CeNPs form charge transfer complexes with H_2O_2,[224] and catecholate compounds,[420] generating a distinctive concentration-dependent optical response. Based on these principles, a variety of colorimetric sensors have been reported using CeNPs as color-generating probes (e.g. as a replacement to commonly used soluble dyes) or to enhance the colorimetric signals of redox dyes such as 3,3',5,5,-tetramethylbenzidine (TMB) or azino-bis(3-ethylbenzothiazoline-6-sulfonic acid) (ABTS). The high stability and rich surface functionalities of the CeNPs makes them amenable to patterning on solid surfaces, providing opportunities for the development of portable and inexpensive sensors.

One of the first demonstration of CeNPs as colorimetric probes was reported in 2011 for detection of H_2O_2 and oxidase enzyme substrates such as glucose.[224] The advantage of this system over conventional colorimetric assays is evident when comparing the two types of assays in **Figure 25AB**. When CeNPs is used as a color probe and peroxidase mimetic, in the presence of H_2O_2, the while/yellowish color of the CeNPs changes into bright yellow/orange, due to the oxidation of Ce^{3+} to Ce^{4+} and formation of peroxide-Ce complexes at the NP surface, producing a unique concentration-dependent response[224]. When CeNPs are co-immobilized with glucose oxidase on filter paper, H_2O_2 is generated on exposure to glucose, and the enzymatically generated H_2O_2 is then measured as a color change. Conventional enzyme based colorimetric assays for oxidase enzymes involve the use of two enzymes, one for the conversion of substrate to H_2O_2 (e.g. glucoseoxidase), and one for the conversion of the enzymatically generated H_2O_2, typically a peroxidase, and a soluble redox dye. Because these reagents are soluble, they are generally used in solution or stored on specially designed reservoirs with reactions being accomplished though microfluidic channels. Conventional dyes are expensive and maintaining their stability is a challenge. Since CeNPs is a stable inorganic material that can replace both the peroxidase enzyme and the organic dye, they can be easily affixed to a solid platform such as paper, plastic or textiles for creating stand-alone portable sensors. Such reagentless sensors have significantly enhanced stability, portability low cost as compared to solution-based assays (**Figure 25C)**. A CeNP-based biosensor for glucose developed on filter paper for example displayed a limit of detection of

0.5 mM with a linear range up to 100 mM glucose. This concept can be extended as a general platform for any oxidase enzyme system that involves generation of H_2O_2 as a reaction product, such as lactate, glutamate, cholesterol, uric acid, ethanol and hypoxhantine (**Figure 25D)**.

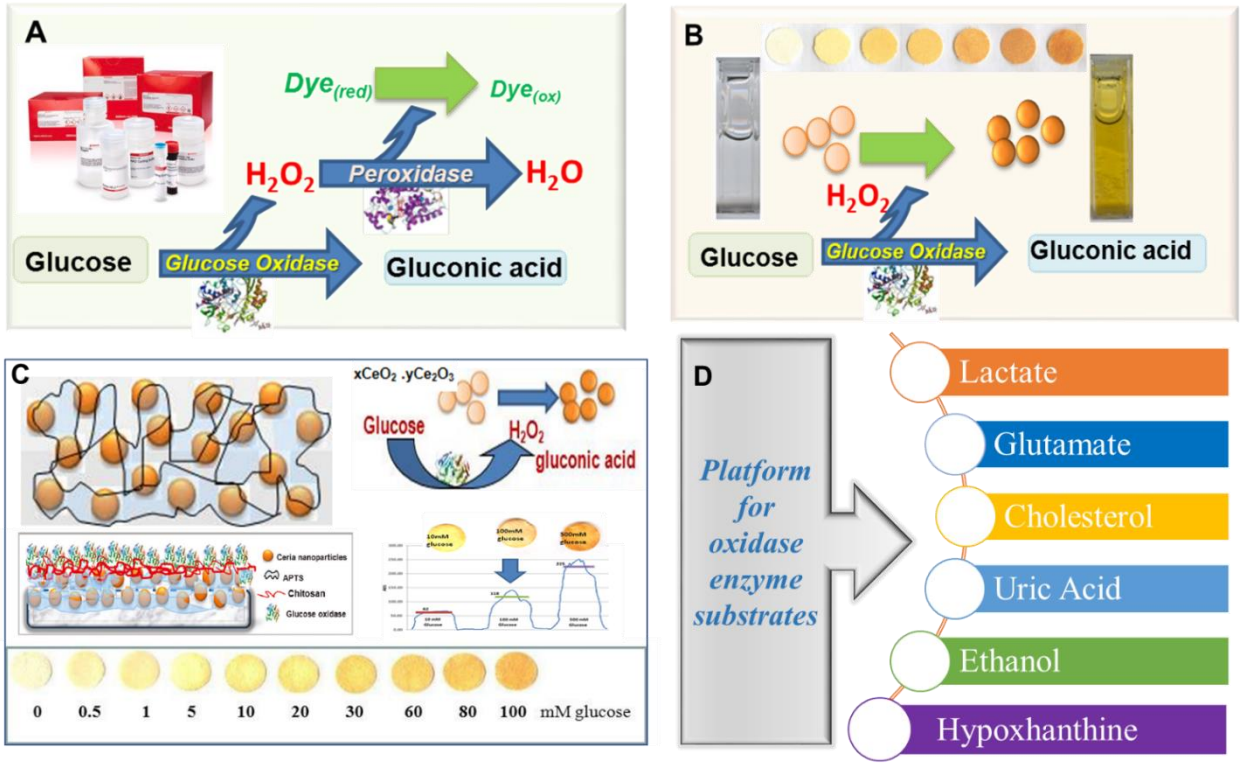

Figure 25*. Detection of glucose using glucose oxidase (GOx) enzyme by conventional colorimetric assay with GOx, peroxidase and a redox dye (A) and the CeNP-based sensor (B). Immobilization of CeNPs on paper using 3-aminopropyltriethoxysilane (APTS) and chitosan biopolymer and image G quantification of biosensor response (C) with examples of biosensor targets developed based on CeNPs used as colorimetric probes (A, B reproduced with permission from Ref [224]. Copyright 2011 American Chemical Society.).*

Similar types of colorimetric sensors based on CeNPs have been designed to detect enzyme activities, such as alkaline phosphatase (ALP). For example, a CeNPs-based sensor was developed based on color changes of CeNPs reacting with hydrolytic products of ALP-catalyzed reactions, from substrates such as catechol monophosphate, ascorbic 2-phosphate and hydroquinone diphosphate. The method, adapted to a paper-based platform, had a detection limit of 0.04 U/L ALP with a linear range up to 2 U/L when ascorbic 2-phosphate was used as substrate.[421] More recently, the activity of beta-galactosidase (beta-Gal) was determined using a procedure involving CeNP-induced oxidation of 4-aminophenol (4-AP) produced in the hydrolysis of the 4-

aminophenyl-beta-d-galactopyranoside substrate (4-APG) by beta-Gal. The approach enhanced the detection sensitivity and enabled beta-Gal measurements in the visible range, reaching up a detection limit of 0.06 U/L and a linear range up to 2.0 U/L. A 30-fold amplification as compared to a commercially available beta-Gal assay was reported using the CeNP assay.[422] In addition to colorimetric sensors, opportunities exist to design CeNP-based fluoresce and imaging assays by doping the CeNPs with Eu. For example, Eu-doped CeNPs (5 nm diameter doped with 2% Eu) exhibit bright and stable fluorescence in aqueous media (**Figure 26**). Their combined catalysis and fluorescent properties can serve as a universal concept to design fluorescent assays with the ability to monitor enzymatic reactions, and quantify enzymatic activity and substrates such as AlP activity, dopamine, glucose and lactate with increased selectivity and sensitivity.[400]

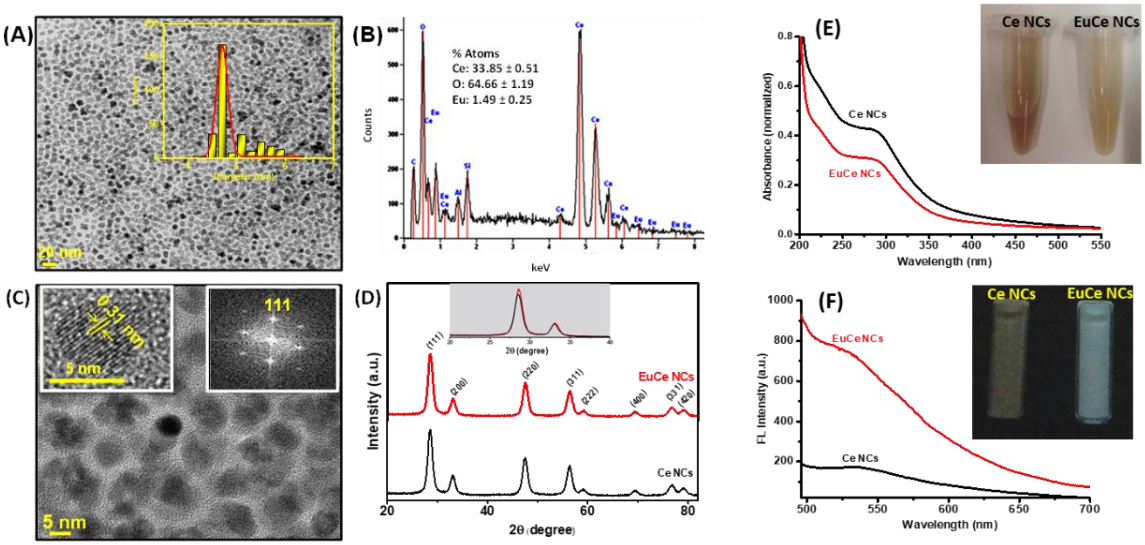

Figure 26*. Morphological, structural and catalytic activity characterization of Eu-doped CeNPs,* ***(A)*** *The HR-TEM (inset: particle size distribution).* ***(B)*** *EDX,* ***(C)*** *HR-TEM at high magnification (inset: dimension of single spherical particle (left) and electron diffraction (right),* ***(D)*** *XRD patterns of CeNPs and Eu-CeNPs. And* ***(E)*** *UV-vis spectra of CeNPs and Eu-CeNPs showing* ***e****mission at* $\lambda_{ex,}$ *466 nm, and* λ_{em} *522 nm, inset: photographs of Eu-CeNPs under UV (365 nm). (Reprinted with permission from Ref* [400]*. Copyright 2018 American Chemical Society).*

The distinctive changes in optical properties of the CeNPs reacting with compounds with phenolic or catecholoamine moieties were used to develop paper based sensors for the detection of phenolic antioxidants, with reported detection limits between 20-400 μM depending on the structure of the compound. These sensors have the capability to provide a unique optical signature generated when CeNPs interact with a single or a mixture of antioxidants. The method enabled

field assessment and classification of the antioxidant capacity in tea,[423] wine,[424] medical mushrooms[425] and cosmetic products[426]. For these measurements, the CeNPs stabilized onto a paper platform form the actual sensing platform (e.g. sensing spot or label), enabling portability and reagentless operation. Similar to a pH paper, analysis is performed by adding the sample to the sensor; the antioxidants in the sample produce an immediate color change that is visible to the naked eye. Quantification is achieved by comparison with a pre-calibrated detection scheme. For more precise quantification, analysis can be performed with a color reader such as a cell phone with a color reading app; no additional reagents are needed (other than the sample). In comparison with other assays for antioxidant analysis, the CeNPs sensors have very low cost and are stable at room temperature and field deployable. Finally, biosensing systems based on CeNPs have practical utility as demonstrated by the development of several standalone devices for detection of ethanol in breath,[427] phenolic antioxidants for evaluating antioxidant activity in teas and wines,[425] and measuring the hypoxanthine content to assess freshness of fish and meat[428], summarized in **Figure 27**.

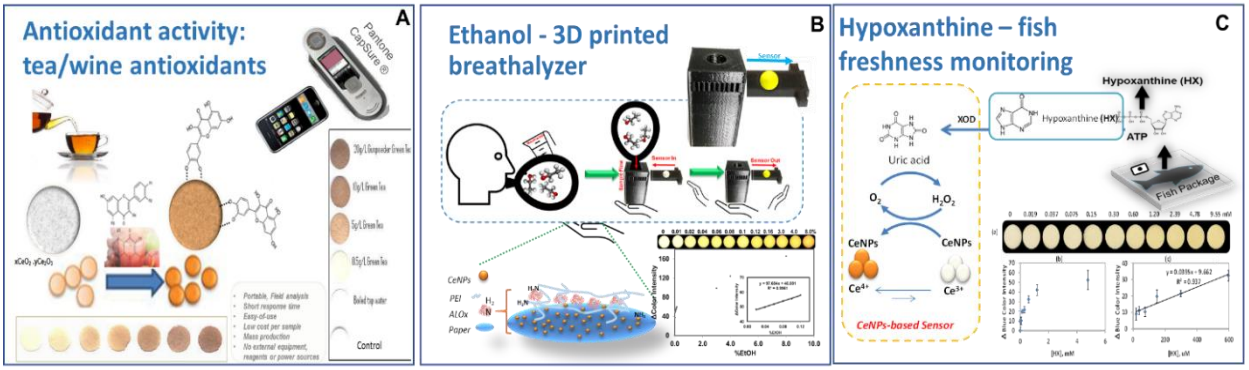

Figure 27*. Examples of practical CeNP-based paper sensors for the detection of antioxidant activity in tea (A), ethanol in breath using a 3D printed device (B) and hypoxhantine to assess the freshness of fish (C). Reprinted with permission from Refs for (A)[425], (B)[427] and (C)[428]. Copyright 2021 American Chemical Society.*

Several hybrid configurations of CeNPs-based enzyme biosensors have been developed in which the CeNPs are used in conjunction with oxidase enzymes to catalytically amplify the enzymatic reaction, or the product of an enzymatic reaction, significantly enhancing the sensitivity of the biosensor. Moreover, the ability of the CeNPs to store and release oxygen has been used as an oxygen reservoir to fuel oxygen to oxidase enzymes, enabling them to operate in oxygen-restrictive environments such as tissue hypoxia. This principles has been demonstrated effectively

for improving sensitivity of implantable electrochemical microbiosensors fabricated by co-immobilizing the enzyme with the CeNPs at the surface of a microelectrode, typically a Pt wire or a carbon fiber brush, with diameters ranging from 100 to 150 μm. Successful developments have been demonstrated with CeNPs-based biosensors for the detection of dopamine,[429] glutamate,[430] lactate[431] and glucose[432]. Enhanced selectivity has been obtained with Pt-doped CeNPs, which imparts conductivity and amplifies the electrocatalytic signal for H_2O_2 oxidation, as shown in **Figure 28A** for glucose detection. The lactate biosensor for example had a detection limit of 37 μM in implantable conditions and was able to quantify the real time release of lactate *in vivo* during cerebral ischemia and reperfusion (**Figure 28B)**.[431] This lactate biosensor operated in a continuous mode due to the ability of the enzymatically generated H_2O_2 to react with the CeNPs producing oxygen in the process. This released oxygen is then utilized by the enzyme, facilitating its functionality in the hypoxic medium. Notable, the biosensors without CeNPs do not provide any quantifiable response due to the lack of oxygen, a necessary cofactor for ensuring enzyme function. Other possibilities to enhance conductivity for electrochemical biosensors are to use the CeNP in conjunction with graphene oxide and PtNPs [433], conductive polymers such as polyaniline [434], or mesoporous carbon [435], leading to enhanced sensitivities. CeNPs can also be designed in the form of a dual-tethered nanosystem in conjunction with fullerene, which combines the properties of the two materials, leading to hybrid structures with high antioxidant and UV-shielding properties[436].

Lastly, significant improvements can be achieved by interfacing CeNPs with high surface area materials such as 2D layered MXenes producing catalytically active materials that can be used in a variety of applications. In a recent work **(Figure 28C)**, MXene decorated with CeNPs enabled the development of an electrochemical biosensor platform broadly applied to a variety of enzymes and enzyme substrates, achieving detection limits of 0.8 μM H_2O_2, 0.49 μM glucose, 3.6 μM lactate and 1.7 μM hypoxanthine.[437] These materials can be integrated within flexible platforms such as carbon cloth and be used to construct wearable devices, as demonstrated for lactate monitoring in sweat.[437]

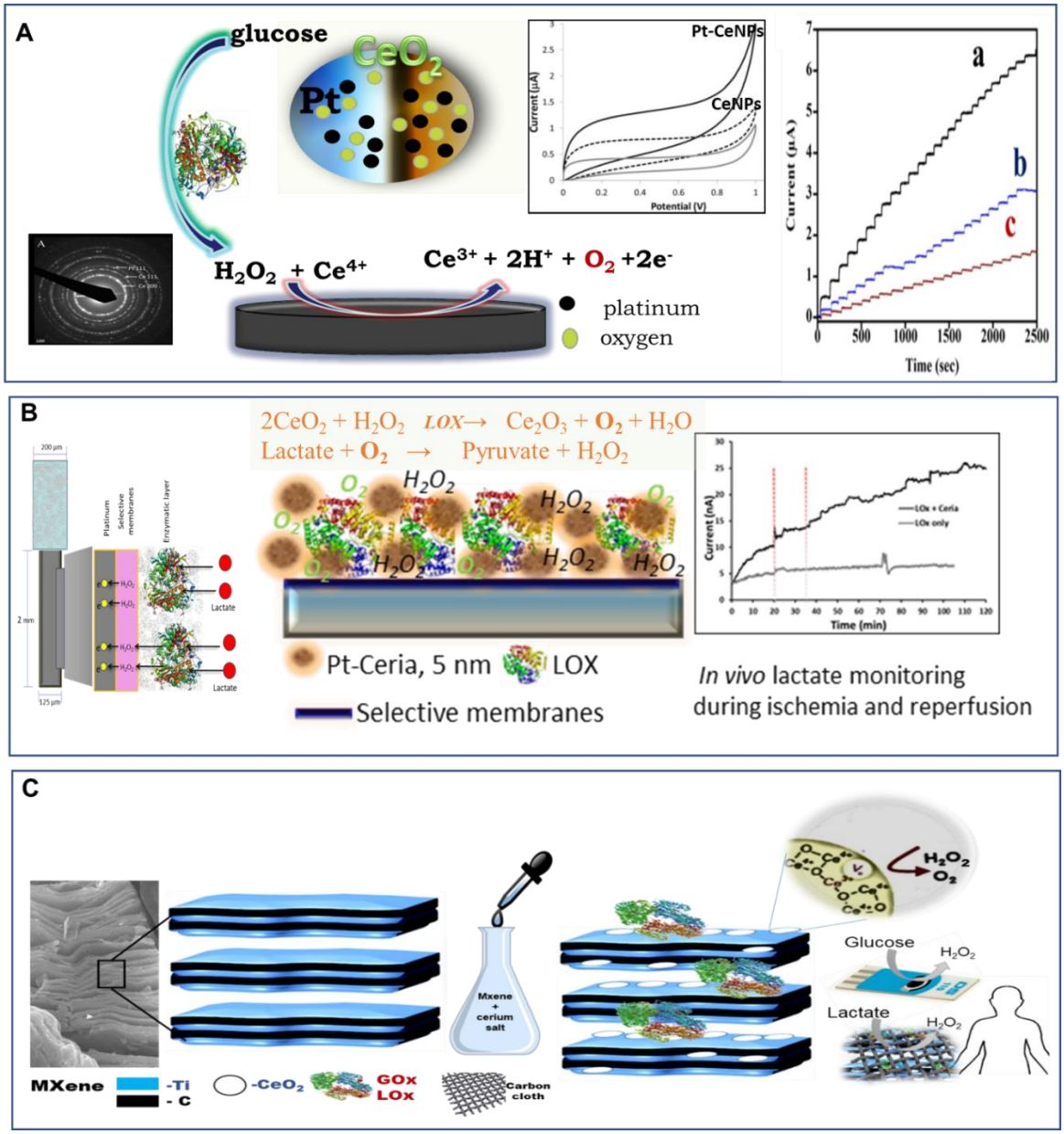

Figure 28. *A) Electrochemical CeNP-based implantable microbiosensors using Pt-doped CeNP (5 nm) which electrocatalyzes H_2O_2 oxidation, further enhancing glucose detection; significantly enhanced responses were obtained when Pt-CeNPs were used (a) as compared to bare CeNPs,(b) or no CeNPs (c) (with permission from Ref [432]); B) Implantable microbiosensor configuration for lactate detection during ischemia and reperfusion showing quantifiable responses when Pt-doped CeNPs were immobilized with lactate oxidase (Reprinted with permission from Ref [431]. Copyright 2015 American Chemical Society.); C) Catalytic MXene-CeNPs biosensing platform for wearable biosensors (with permission from Ref [437]).*

4.3.3 Affinity-based biosensors

CeNPs have been widely used to create affinity biosensors based on interactions of immuno, DNA or aptamer receptors and their targets at the CeNPs surface, or by using CeNPs as an enzyme-mimetic label, in solution or deposited on electrode surfaces. Examples of general strategies of CeNP-based affinity sensors are shown in **Figure 29**. Colorimetric assays are using the enzyme-mimicking activity of the CeNPs and their ability to react with dyes such as TMB to quantify affinity binding interactions. For example, the CeNPs's oxidase-like activity enabled electrochemical detection of DNA amplicons, by taking advantage of the electrostatic interaction between DNA with CeNPs, quantified using TMB. The adsorption of the amplicons to the CeNP surface blocks the CeNP's catalytic activity, thus decreasing the biosensor response, proportionally to the concentration of the PCR products **Figure 29B**. The method enabled determination of DNA amplicons derived from E. Coli with an assay time of 6 min.[438] Recently, it was shown that such interactions can be conveniently monitored with a low cost personal glucose meter, making it amenable to point-of-care testing.[439] Detection was accomplished by monitoring CeNPs aggregation induced by DNA amplicons produced by PCR, and quantifying the reduced ability to catalyze glucose oxidation in the presence of target due to electrostatic binding of the amplicons to the CeNPs. The assay time was 5 min and the target genomic DNA derived from E. Coli was determined down to 10 copies, indicating promise of this method for low cost PCR amplification. In another work, a CeNPs-based aptasensing platform was reported using the ability of the CeNPs to interact electrostatically with ssDNA aptamers (**Figure 29A)**. Target binding was quantified by measuring changes in the CeNP's catalytic activity (e.g. with TMB) before and upon target binding. Target binding was found to induce conformational changes of the aptamer at the CeNPs surface, changing the surface coverage and resulting in a decrease response proportionally with the increase in target concentration, measured by reaction with TMB[440]. The method enabled detection of ochratoxin A, a toxin produced by fungi, down to 0.15 nM.

Another interesting application is to use CeNPs as a replacement of the enzyme label in conventional affinity assays (e.g. ELISA) in lieu of oxidase or peroxidase enzymes. One of the first reports suggesting that polymer (polyacrylic acid) coated CeNPs can be used as an oxidase enzyme label in immunoassayas was published by Asati *et al*, in 2009 who demonstated that conjugation of CeNPs with targetting ligands can be used as a nanocatalyst with dual function, as target binding and catalytic detector via oxidation of colorimetric dyes, TMB (**Figure 29C)** [441].

Enhanced detection for electrochemical aptasensors has been achieved by immobilizing the aptamer on a graphene –modified screen printed electrode[442]. The target was captured by the immobilized aptamer and determined via a competitive mechanism between the free and the CeNPs labelled target by monitoring the H_2O_2 oxidation, amplifyed by the CeNP tag. Detection limits in the low nM range (0.1 nM), with a linearity range up to 180 nM were obtained for detection of a mycotoxin, ochratoxin A. Such strategies can be successfully implemented in point-of-care diagnostic devices.[443]

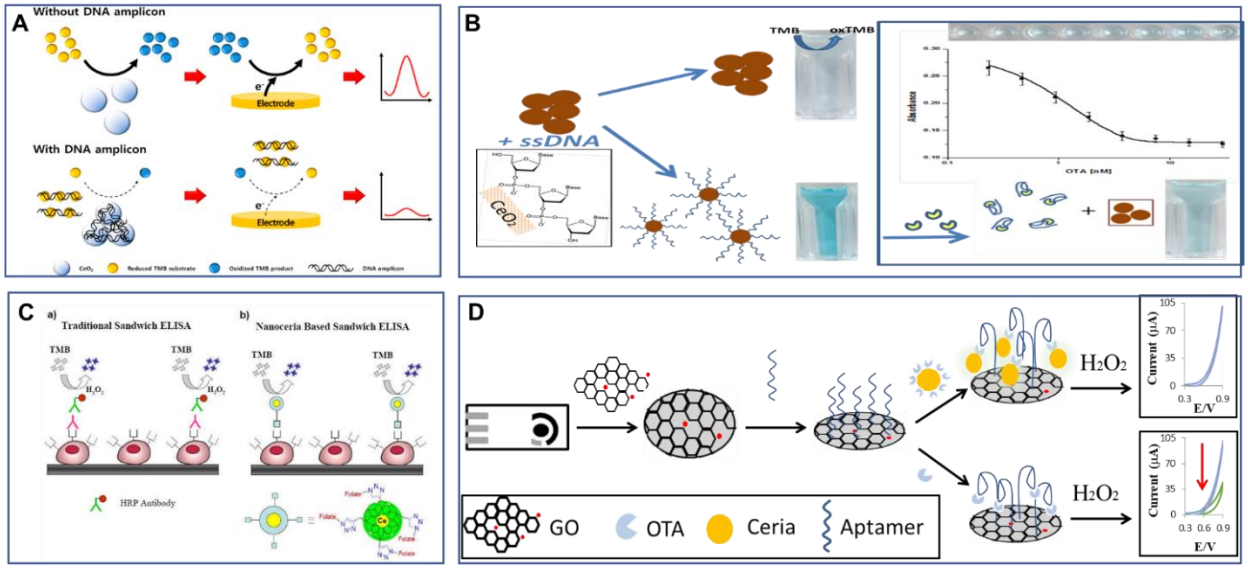

Figure 29*. Examples of bioaffinity interactions with CeNPs as enzyme-mimetic nanocatalyst with electrochemical (A and D) and colorimetric (B and C) detection: A) electrochemical detection of DNA amplicons by quantifying the catalytic activity of CeNPs using TMB (Reprinted with permission from Ref [438]), B) colorimetric detection of target binding to DNA-aptamer modified CeNPs with detection of target induced conformational changes and aggregation (with permission from Ref [440]), (C) comparison between traditional immunoassay (ELISA, a) and CeNPs-based sandwich assay with CeNP labels mimicking the activity of oxidase enzyme. (Reprinted with permission from Ref [441]), and D) electrochemical sensor using CeNP tag and graphene oxide for detection of aptamer targets through measurement of the CeNP's- catalyzed H_2O_2 oxidation with and without target (Reprinted from Ref [442] with permission from the Royal Society of Chemistry).*

DNA-functionalized CeNPs can be used for a variety of biosensing applications such as to probe oxidation of phosphorous compounds[444] and H_2O_2.[445] Modifications of the CNP surface can be made to enhance the oxidase-like activity and enable detection of ions such as fluoride, quantified indirectly using ABTS dye.[404] Moreover, the CeNP's surface chemistry and surface ligand can be

modulated to immobilize or displace DNA from the CeNPs' surface for detection of substrates such as H_2O_2 and glucose in serum.[445] When CeNPs was coupled with glucose oxidase, a detection limit of 8.9 mM glucose was obtained. More recently, an integrated system of CeNPs / glucose oxidase was used to produce bio-nanoenzyme catalytic cascades with oxidase-like activity[446]. Inhibition of the oxidase-like activity of CeNPs by ions such as arsenate and arsenite[447] or phosphate due to blocking of Ce^{3+} sites[448] was also reported, opening up new avenues for the development of biomimetic CeNPs inhibition-based sensors. Such engineering designs of the CeNPs surface could increase performance of CeNPs, making them powerful nanoenzymes for many practical applications.

More recently, hybrid materials and supramolecular structures such as Ce-based MOFs, traditionally known for their electrolytic performances[449, 450] have begun to be explored in biosensing. A bimetallic Ce/Cu-MOF (CeO_2/CuOx@mC) aptamer nanocomposite was prepared for the detection of trace tobramycin (TOB) in human serum and milk[451]. Similarly, a nanohybrid of covalent organic framework (COF) and Ce-based (Ce-MOF@COF) nanostructure showed high binding affinity toward the oxytetracycline (OTC)-targeted aptamer[452]. The aptasensor displayed good reproducibility, selectivity, stability, and acceptable applicability for detecting OTC in various samples, including milk, wastewater, and urine. Future development of Ce-based mesoporous materials such as Ce-MOFs, which possess high porosity could lead to the development of enhanced catalysts for next generation sensing.

4.4. Environmental remediation

The presence of contaminants, such as metals, organic dyes, pesticides, nutrients and toxins is a worldwide concern due to their long-term environmental effects[396]. Because of its thermal stability, optical properties, and oxygen transport capacity, CeNP-based materials can be used as sorbents in environmental remediation for water and wastewater treatment[453-455]. CeNPs can be used alone, in binary mixtures or deposited on various supports such as activated carbon, graphene, polymeric nanofibers, or mesoporous structures (**Figure 30**). Their removal properties are attributed to the high surface charge density,[456] hydroxilated surface and rich surface defects that facilitate the rapid complexation of oxyanions such as phosphates and arsenates.[5, 457] To improve handling, CeNPs has been added to conventional adsorbents such as activated carbon or carbon

cryogel[458], patterned on surfaces, or used in conjunction with porous materials such as mesoporous silica[459], hierarchical porous CeO_2-ZrO_2 nanospheres[460], or MOFs[300, 457].

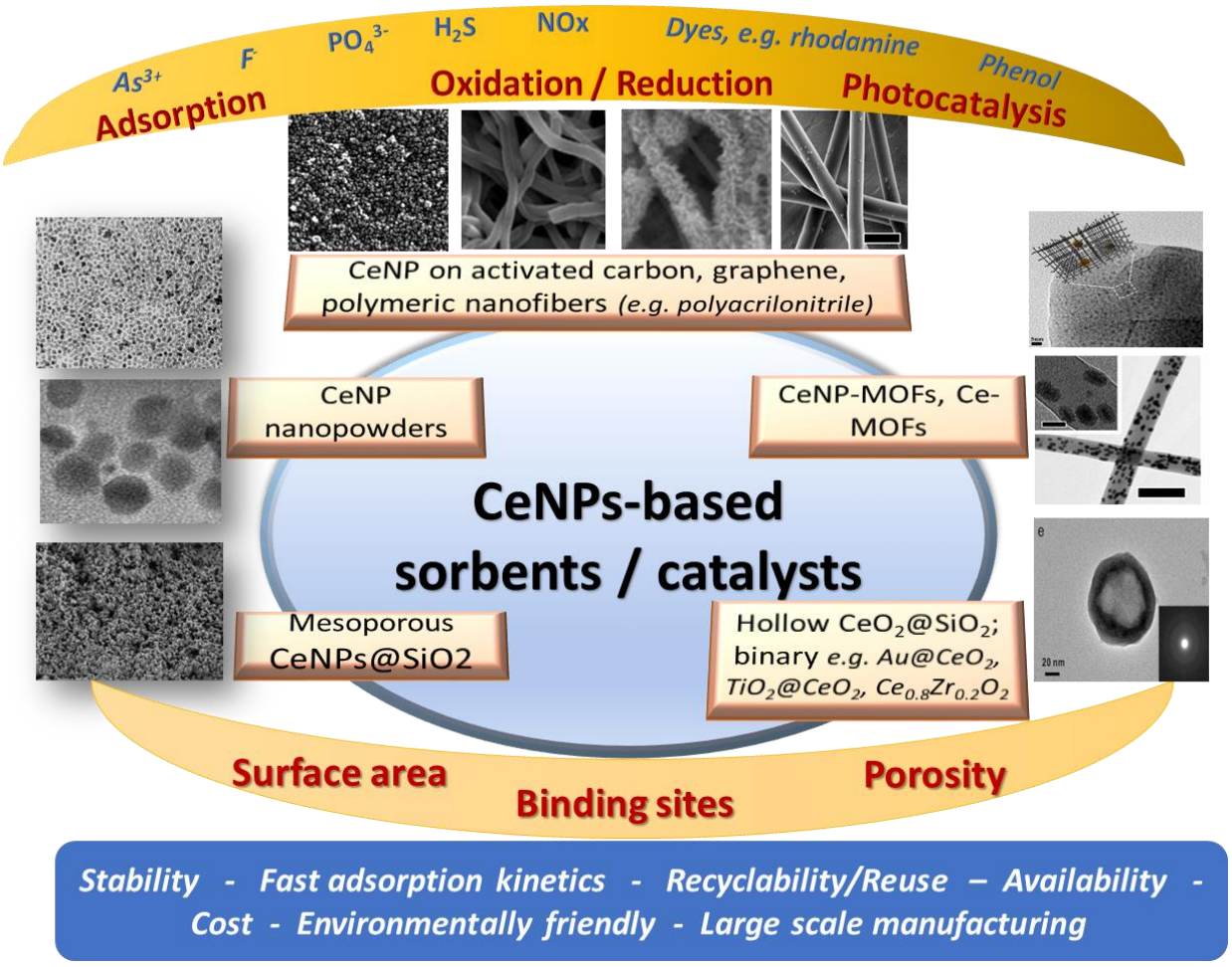

***Figure 30**. Summary of CeNPs-based materials for environmental remediation.*

Ceria coated activated carbon was synthesized in a single step and used in water purification where it demonstrated high efficiency for the removal of As(III) and As(V)[461]. Additionally, a nanocomposite prepared from graphene nanosheets and CeNPs (G/CeO_2) was used for the extraction of Se(IV), As(V), As(III), Cu(II) and Pb(II) from water[462]. The maximum adsorption capacity of G/CeO_2 was extrapolated from the Langmuir model and found to be 8.4 for As(V), 14.1 for Se(IV), 50.0 for Cu(II) and 75.6 for Pb(II) (expressed in $mg \cdot g^{-1}$). These also showed good selectivity towards Se(IV) in the presence of Se(VI). CeNP-based materials were also used for ultratrace metal ions detection and speciation via electrochemistry[271]. Enhaced arsenic removal

was achieved using porous CeO_2-ZrO_2 hollow nanospheres due to the high sorption capacity and selectivity for As; adsorption capacities of 110.7 and 145.3 $mg.g^{-1}$ were reported for As^{3+} and As^{5+} respectively [460]. As a dual Ce^{3+}/Ce^{4+} oxidation state material, CeNPs can participate in electron exchange reactions with As^{3+} ions present in solution. The mechanism of As adsorption and redox processes occurring between the surface Ce^{3+}/Ce^{4+} and As^{3+} at different pH conditions was demonstarted at single particle levels using nanoscale electrochemistry by monitoring the oxidation of As^{3+} to As^{5+} at 0.8V *vs.* Ag/AgCl or the reduction of As^{3+} to As^0 at -0.3V (*vs.* Ag/AgCl) [463]. The highest sorption capacity was observed at pH 8. In acidic environments (pH<4), a small fraction of As^{3+} was oxidized to As^{5+} by surface Ce^{4+} and further adsorbed onto the CeO_2 surface as a As^{5+} bidentate complex (**Figure 31**). Adsorption was common in basic conditions, confirming strong adsorption of As^{3+}onto CeNPs. These findings pave the way for rationally selecting the optimal material structure and conditions to increase sorption capacity for environmental sensing and remediation applications.

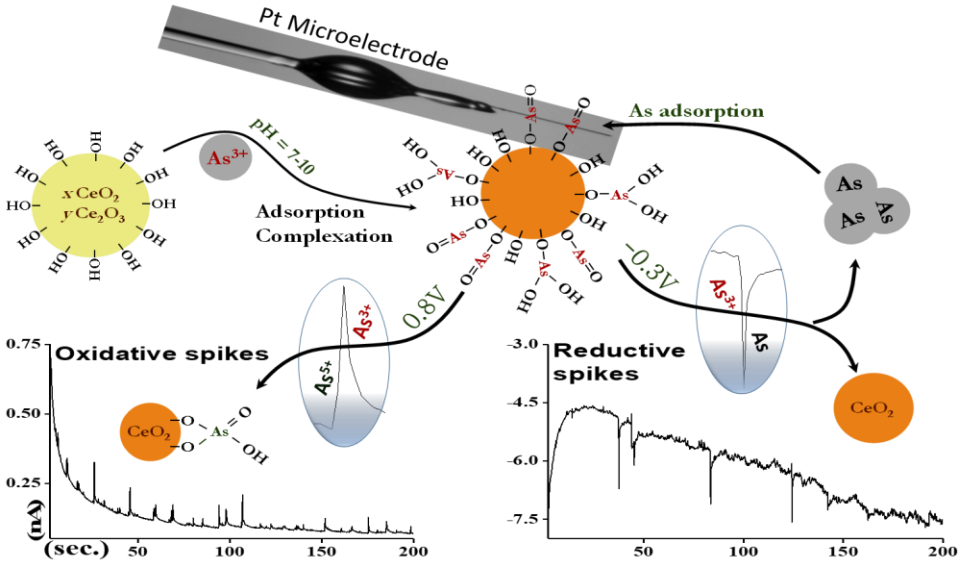

Figure 31. *Mechanism of As^{3+} adsorption on CeNPs quantified by nanoscale electrochemistry by measuring current transients measured in reductive (-0.3 V) and oxidative (0.8 V vs Ag/AgCl) conditions in PB at pH 8. Reproduced with permission from refs [463]. Copyright © 2019, American Chemical Society.*

CeNPs exhibit high selectivity for fluoride (F^-) adsorption and can be used as adsorbent for F^- removal from water. F is one of the essential elements in the human body for the formation of dental enamel and normal mineralization of bones[464]. However, the excessive intake of F^- is harmful to the body and can lead to various health issues ranging from mild dental fluorosis to

crippling skeletal fluorosis. While CeNPs are effective adsorbents and could be used in large scale column purification technologies for water defluoridation, their small size is impractical as it could cause column blockage, high pressure drop, and low flow rate. To overcome these limitations, binary oxides and hydroxides such as CeO_2–ZrO_2 nanocages[465] and Ce–La binary hydroxide[466] were explored as alternative sorbents with good F^- uptake, but slow adsorption rate. Further improvements were achieved using CeNPs incorporated on active supports like silica and organic polymers which provide a large specific surface, fast diffusion kinetics, low cost, high mechanical strength and low pressure drop in a packed adsorption column[467-470]. F^- adsorption onto a cubical ceria nanoadsorbent has shown pH-responsive behavior during the adsorption process[471]. At lower solution pH, a release of OH^- was observed during the adsorption of fluoride by inner-sphere complex formation. At higher solution pH, the pH was found to decrease due to the exchange of Na^+ added in the form of NaOH by outer-sphere complex formation with H^+ ions adsorbed electrostatically on the adsorbent surface[471].

Other environmental applications of CeNPs are as catalysts to remove exhaust emission,[472] volatile organic chemicals (VOCs) and degrade organic pollutants from the environment. For example, CeNPs have shown high performance towards the reduction of NO_x and the catalytic oxidation of NH_3 from engine exhaust.[473] Owning to their oxygen storage/release and the Ce^{4+}/Ce^{3+} redox cycle, CeO_2-based catalysts are excellent candidates for the selective catalytic reduction of nitrogen oxides (NO_x) and carbon monoxide (CO) which contribute to acid rain and photochemical smog. In a typical catalytic convertor, ceria acts as a buffer adsorbing and releasing oxygen species depending on the operating conditions and temperature. It was reported that the use of CeNPs (30 nm) as an additive to fuel resulted in reduced fuel consumption by 2.5%, as well as reduction in NOx emission by 15.7% and smoke opacity by 34.7% compared to the additive-free fuel[474]. Enhanced catalytic performance for selective NOx reduction by NH_3 was obtained with the CeNP-based catalysis on oxide supports such as Al_2O_2, TiO_2 and WO_3 with the highest activation ability for Ce-O-W through rich Bronsted acid sites, redox ability and strong electronic CeO_2-support interactions.[475] NPs of CeO_2, CuO/CeO_2 and $Pt\text{-}MnO_2/CeO_2$ have shown high activity for the oxidation of phenol intermediates.[476-478] Nanocomposites of TiO_2/CeO_2 on carbon nanotubes have demonstrated photo-oxidation capabilities for the degradation of organic content in agricultural wastewaters.[479] Pd/CeO_2 with carefully designed morphology and optimized shapes were effective catalysts for methanol decomposition to syngas with excellent activity at low

temperatures[480]. Mn-doped CeNPs prepared by hydrothermal synthesis have shown a drastic increase in their capacity to adsorb oxygen due to intercalation of Mn^{3+} and the decrease in the $Ce^{3+}/ (Ce^{3+} + Ce^{4+})$ content in the doped samples, by replacement with Mn^{3+}. The doped samples had a significantly higher activity for toluene oxidation[481].

CeNPs have been also studied for the photocatalytic degradation of reactive dyes at which more than 95% of the dyes were destroyed under solar irradiation[482]. Recent work showed the ability of CeNPs to effectively degrade organic dyes such as fluorescein, rhodamine B, brilliant blue and coomassie blue, with enhanced degradability in the presence of fluoride at ambient temperature[483]. The enhanced degradability in the presence of fluoride was attributed to the increased oxygen vacancy and the strong acidic environment. Hybrid CeNPs -lanthanide oxides demonstrated H_2S adsorption and dissociation with subsequent oxygen vacancy regeneration, enabling their use for the desulfurization of biomass effluents.[484] It was demonstrated that adding Ce to metal oxide catalysts enhanced the catalytic activity and SO_2 resistance of Mn/Ti catalysts for the NO reduction with NH_3 by inhibiting the accumulation of ammoniom sulfates and preventing sulfidation. [485] Addition of a small amount of Ce (Ce/Ti = 0.05) was shown to improve the oxygen storage/release of the MnOx-CeO_2/TiO_2, enhancing activity. Binary nanofibrous structures based on anisotropic Au/CeNPs embedded in poly(vinyl alcohol) (PVA) have shown potential as photocatalytic materials, promoting both oxidation and reduction of model waste products for environmental remediation processes such as the catalytic reduction of 4-nitrophenol to 4-aminophenol and of phenol red to bromophenol as well as the degradation rhodamine B in a flow-through reactor (**Figure 32**). [486]

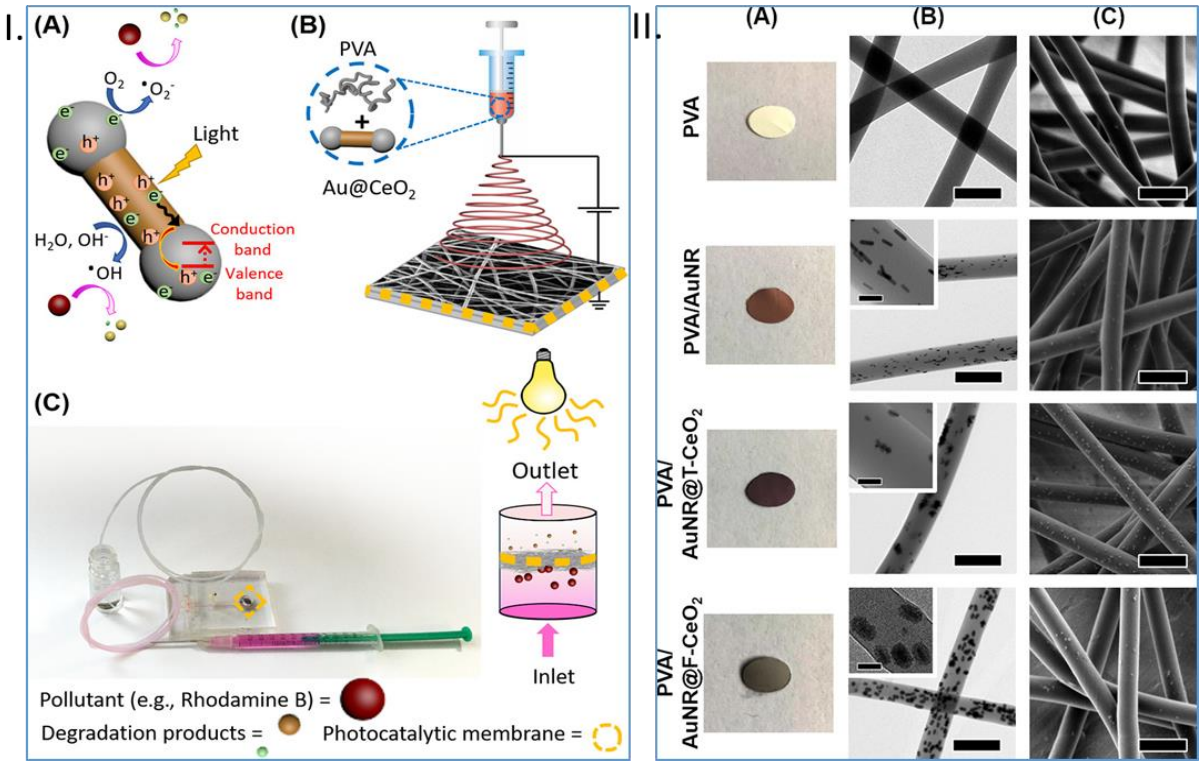

Figure 32. *I) Photocatalytic membranes prepared by colloidal electrospinning of a suspension of poly(vinyl alcohol) (PVA) and Au-CeNPs for use in a flow-through fluidic reactor showing (A) photocatalytic process, (B) Preparation of Au@CeO2/PVA nanofibers by electrospinning, and C) photo catalysis with the flow-through reactor containing the nanofibrous membrane; and II) Images (A), TEM (B) and SEM (C) of electrospun hybrid membranes made with PVA, PVA/AuNR, PVA/T-AuNR@CeO_2, and PVA/F-AuNR@CeO_2. Reprinted with permission from Ref [486]. Copyright 2019 American Chemical Society.*

In other environemental applications, CeNPs have shown tremendous potential as sorbents for the removal of phosphorus to prevent water eutrophication. Eutrophication has become a global environmental problem due to unnatural enrichment of water bodies with phosphorus (P) and nitrogen (N) which leads to the excessive growth of harmful algae blooms, and depletion of dissolved oxygen levels creating dead zones[269, 457]. Thus, removing the excess P and N is essential for prevening the negative consequences of eutrophication[269, 487]. CeO_2-coated nanofibers have shown high adsorption capacity for the removal of P from aqueous solutions[488] with an adsorption capacity of 17 and 12 mmol/g at low pH (2–6) and neutral pH. The removal process involved the formation of $CePO_4$ on the nanofiber surface. In other works, a recyclable adsorbent based on CeNPs grafted on mesoporous silica beads (CeO_2-SiO_2) has shown reversible adsorption behavior for P, demonstrating potential for both the removal and recovery of this important nutrient from

eutrophic waters (**Figure 33**)[459]. The adsorption mechanism involved binding of PO_4^{3-} through ion exchange and Lewis-acid based interactions, which provided a sorption/desorption capacity of 110 $mg.g^{-1}$ with 99% removal within 60 min, significantly higher as compared to other sorbents. In follow up work with this system, ultrafast removal was achieved by using a Ce(IV)-based MOF, the Ce(IV) UiO-ss, Xe 1,4-benzenedicarboxylate (Ce-BDC) which provide high surface area due to the open pores and high binding affinity of its open metal sites for phosphate. A removal capacity of 179 $mg.g^{-1}$ within 4 min, and ermoval capacity ina broad range of pH (2-12) was reported.[457] Other enhancements have been obtained using binary oxides with properly designed ratios[489, 490], optimized to enhance surface defects and facilitate complexation, thus increasing adsorption capacity as compared to the single bare oxide. Su *et al*., developed a solvothermal process to synthesize a series of Ce/Zr binary oxide nanoadsorbents. A sorption capacity of 112.2 $mg.g^{-1}$ was reported with an optimized oxides ratio of $Ce_{0.8}Zr_{0.2}O_2$[491]. In order to facilitate the recovery of the adorbents after the treatment, core-shell CeNPs (Fe_3O_4@SiO_2-CeO_2)[492] and (Fe_3O_4@SiO_2@*m*CeO_2)[493] were designed to magnetically separate and remove of these sorbents from the water environment. These structures can be utilized in a variety of applications such as membranes for phosphate separation and purification, sorbents for solid phase extraction or as P-selective materials for environmental sensing. Recently, it was shown that the use of Ce-metal nodes in the UiO-66-NH_2 MOF structure enable the fluorimetric sensing of phosphate, with a detection limit of 4.5 μM in a single step measurement procedure.[494]

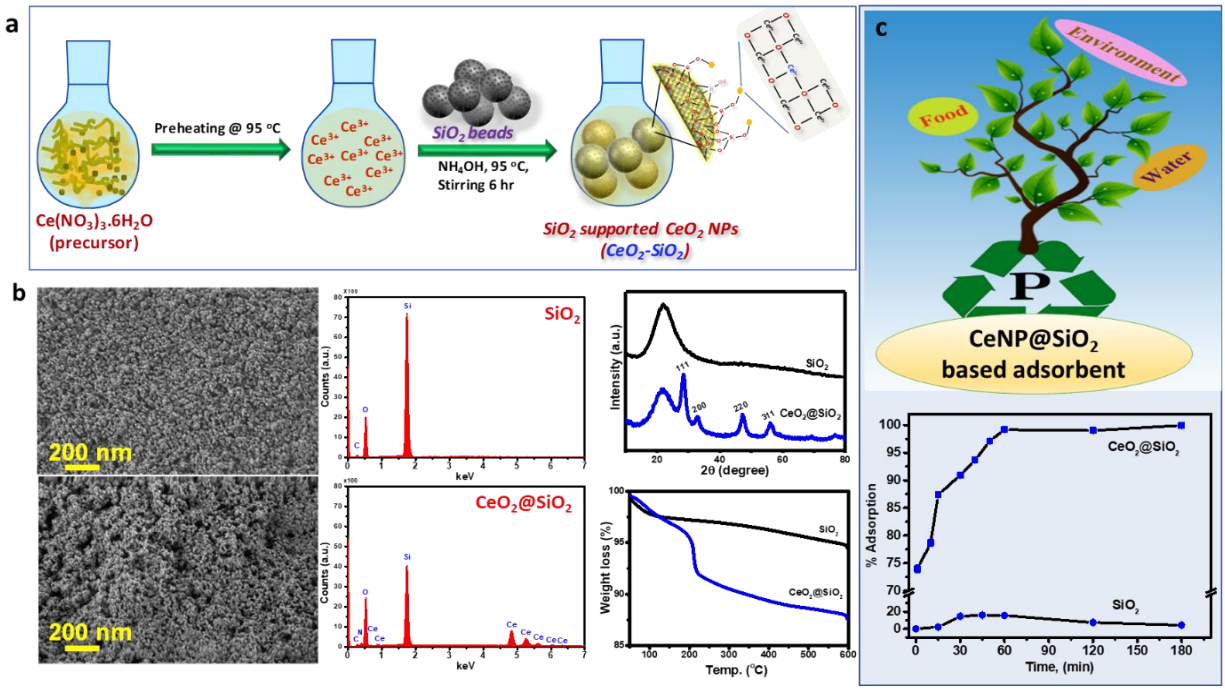

Figure 33*. Synthesis of CeO_2@SiO_2 adsorbent (a) with SEM, XRD and TGA characterization (b) and adsorption isotherms for the removal of phosphate (c) showing significantly enhanced adsorption capacity of the for CeO_2@SiO_2 as compared to SiO_2 (Reprinted with permission from Refs [459]. Copyright 2019 American Chemical Society.).*

While the properties of CeNPs are vastly explored, their potential environmental and toxicological effects are still under investigation. The release of CeNPs into the environment is expected to increase as they start to be implemented in real-world applications[493, 495]. Their use as polishers in the semiconducting industry[496] and as diesel fuel additives for catalytic convertors to control auto exhaust emission[497] are just two examples that can the result in release and accumulation of CeNPs in the environment. Toxicology studied suggest that CeNPs by themselves are not particularly toxic; however, they can become toxic by adsorbtion of toxic ions (e.g. As^{3+}) or organics to their surface.[463] Therefore understanding the fate, transport, and toxicity of these NPs exposed to contaminants is becoming increasingly important and will be critical in further studies to examine their environmental and health impacts[5, 498]. Green synthesis of CeNPs can provide alternative routes to prepare CeNP-based materials without the need of using environmentally harmful reagents. For example, CeNPs were synthesized using plant-mediated synthesis at which different plants such as *Gloriosa superba*, *Acalypha indica* and *Aloe vera* were used[499-501]. Additionally, honey, egg white and fungus-mediated synthesis were also used[502-504]. These plant extracts and natural components act as capping and reducing agents to produce

nanocrystalline CeNPs in different sizes and morphology. These methods also offer advantages such as the low cost, large-scale production, and more importantly their environmentally friendly nature, making them interesting candidates for use in biomedicine and pharmaceutical applications. A detailed review on the green synthesis of CeNPs and their biological applications has been published[505].

4.5. Biomedical applications

The ability of CeNPs to catalyze the detoxification of free radicals and act as artificial antioxidants provides a broad range of opportunities for using this system in biomedicine, particularly for treating disease conditions in which excess free radical formation is thought to play a role.[506] These range from relatively rare diseases, such as Amyotrophic lateral Sclerosis (ALS), to more common conditions, such as stroke, cancer,[507] traumatic brain injury, Parkinson's and Alzheimer's Disease to the ubiquitous normal processes of aging. CeNPs possess a number of advantages over other antioxidants. CeNPs have been shown to provide antioxidant, immunomodulatory, antimicrobial and antiviral, and anticancer properties, and their ability to be used as theranostic probes.[8] When administered systemically, CeNPs appear to cross the blood brain barrier.[508]

Their properties can be enhanced by modification with other drugs as demonstrated with edaravone attached using poly(ethylene glycol); the combined effect provided enhanced neuroprotective action for stroke treatment through the inactivation of ROS and enhanced accessibility to cross the blood brain barrier.[509] The regenerative behavior of the CeNPs, enabling them to regain the antioxidant activity upon interaction with ROS, provide additional opportunities for these particles to remain active for long periods of time, and be used in tissue engineering to support neural survival and growth.[510] Thus, they could be administered preventatively or early in a chronic disease process. Other applications include utilization in spinal cord repair as neuroprotective agents,[511, 512] support cell survival[513, 514] and scavenging ROS in the eye to prevent degenerative retinal disorders.[513] When cells were exposed to H_2O_2, CeNPs reduced oxidative damage by over 60%.[9, 511, 512]

CeNPs holds potential as a drug delivery platform for targeted therapy. For example, they can be conjugated with other therapeutically-effective molecules to improve drug delivery[515] or modified with specific receptors and biomolecules for targeted delivery [516] and wound healing.[517]

The tunable surface and large surface to volume ration facilitate enhanced loading and potential for release, making them a versatile platform for personalized medicine.[518] They can also be incorporated in hydrogels or other biomaterial matrices and used to support cell adhesion and proliferation, and promote wound healing.[519] The tunable catalytic activity of the CeNPs has been shown to be effective in preventing chemotherapy-induced acute kidney injury and restore redox homeosthasis.[520] Biomedical imaging is another area in which CeNPs can find exciting emerging applications such as contrast agents and imaging modalities for magnetic resonance imaging (MRI) and computed tomography. This can be achieved by surface modification of the CeNPs with dyes or other imaging agents or by doping with Eu or Gd, enabling visualization of biological processes and monitoring of therapeutic response, thus facilitating early detection and monitoring of diseases.[521, 522] While biomedical applications of the CeNPs are rapidly emerging, rational design and better control of the structure, properties and dose response is still needed to establish conditions that can effectively reduce the level of free radicals without impairing the normal physiological functions. Several reviews expanding on the biomedical and theranostic applications of the CeNPs can be found in literature.[8 169, 171, 523]

5. Summary and Outlook

The unique structure, tunable reactivity and rich surface chemistry make CeNP an extremely versatile material for a wide variety of applications. Here, we have comprehensively reviewed progress made in the development of CeNPs's based materials, their structure, properties and emerging applications over the past two decades. The synthesis and control of surface properties represent key strategies for customizing the physicochemical characteristics of these materials to meet the requirements of diverse applications. Continued research in this area is essential for unlocking the full potential of the CeNPs in addressing current technological challenges and advancing new products and innovations. Understanding the structural properties at the atomic levels provides the fundamental knowledge necessary to engineer structures with controlled reactivity and surface functions. Such studies are still needed to identify key parameters in the synthetic design that can be used to predict reactivity and generate CeNP-based materials and devices with the desired properties for a given target. Further improvements in the synthesis, surface functionalization and the use of in situ characterization techniques will help achieve better

control of the CeNPs properties (e.g. antioxidant *vs* pro-oxidant), and develop predictable structures with tailored reactivity and surface binding characteristics. Moving forward we see development in the following areas.

- First, fundamental work is still needed to identify the origin of CeNP reactivity (surface defects, complexation, Ce^{3+}/Ce^{4+} ratio, size, shape and surface ligand effects) and how these relate to the physicochemical properties and reactivity of the materials. Considerable progress is expected in modulating the surface chemistry and developing structure/function relations, some of which may require computational design for understanding the complex CeNPs chemistry and predicting activity and selectivity for a given target.
- Secondly, recent work has shown that combining two or more materials and creating hybrid and composite structures can significantly enhance properties and yield diversified high-performance materials. Understanding the effect of interfacial structures and interactions between the two or more types of materials (chemical bonds, surface energy, interface mechanics, etc.) is needed to more rationally design structures that take advantage of the synergistic effects and complementarity of their mixed components. Examples include noble metals (Pt, Au) -CeNPs, polymeric materials - CeNPs, metal oxides- CeNPs, in particular those with catalytic and magnetic properties (TiO_2, ZnO, Fe_2O_3); as well bio-interfaces by conjugating CeNPs with enzymes, aptamers, DNA, antibodies, etc. for obtaining improved catalytic and sensing functions.
- Third, as applications of these materials continue to grow, the manufacturing and integration of CeNPs in devices, membranes and coatings will constitute an area of intensive research. The use of smart technologies and advanced manufacturing practices such as 2D and 3D printing are of great interest to produce low-cost high throughput structures. Moreover, integrating CeNPs into functional and practical devices will be needed to effectivelly translate these innovations into the practice and consumer applications.
- Forth, as more CeNPs are implemented into consumer products, understanding their environmental transformation, fate, transport and toxicity of the CeNPs and their transformed products will be needed, particularly in areas where there is a risk of exposure such as semiconducting manufaring plants where large amounts of CeNPs-containing waste is generated, or in high trafic areas were small CeNPs additives could be released from diesel engine emissions. Tailoring the surface to minimize potential harmful effects is also needed to prevent toxicity on the natural environment and humans. Given their reactivity, the use of CeNPs should be considered

with a full understanding of their unique properties in order to reduce potential risks and ensure their safe utilization and implementation into the practice.

- Finally, we expect exciting developments in several areas, highlighting versatility of these materials in addressing many societal challenges ranging from semiconducting industries to healthcare, environmental remediation and consumer products. Among those, new generations of CeNPs with controlled morphology and surface chemistry will be needed to be used as polishers in CMP to address the needs for smaller and greener semiconducting manufacturing processes. CeNP-based photocatalysts and sorbents will continue to attract interest for environmental remediation and energy conversion. Particularly, the tunable redox chemistry and electrochemical stability make them interesting candidates for electrode materials, electrolytes and catalysis, while the catalytic activity towards pollutants such as VOCs, NOx, metals and organics make them well suited for promoting detoxification and removing contaminants through redox and surface adsorption reactions. An array of products and applications are expected to emerge from the exploration of the antioxidant activity and ability to protect cells from oxidative damage, with impact in drug delivery, biomedical imaging, neuroprotection and the cosmetic industry as anti-aging and UV-protection agents in skin-care. Continued research and development will be needed to explore and optimize the performance of CeNPs in these diverse applications.

In summary, it is increasingly clear that CeNPs have huge potential as demonstrated by an already increasing number of applications in many areas of science and technology and industries such as catalysis, sensing, semiconductor and environment. The review has tried to provide in a systematic and comprehensive manner the most significant advancements to date. Scientists and engineers can use this overview as a starting point to explore this material's unique and unusual properties and pursue new avenues into the future.

6. Acknowledgments

This material is based upon work supported by the National Science Foundation under Grants 20425544, 1336493, 0954919. Any opinions, findings, and conclusions or recommendations expressed in this material are those of the author(s) and do not necessarily reflect the views of the National Science Foundation. SA acknowledges all past and present members of Andreescu's group for their contribution to the study of various aspects of ceria chemistry.

References

1. J. Paier, C. Penschke and J. Sauer, *Chemical Reviews*, 2013, **113**, 3949-3985.
2. R. Schmitt, A. Nenning, O. Kraynis, R. Korobko, A. I. Frenkel, I. Lubomirsky, S. M. Haile and J. L. M. Rupp, *Chem Soc Rev*, 2020, **49**, 554-592.
3. T. Montini, M. Melchionna, M. Monai and P. Fornasiero, *Chemical Reviews*, 2016, **116**, 5987-6041.
4. E. Ozkan, P. Cop, F. Benfer, A. Hofmann, M. Votsmeier, J. M. Guerra, M. Giar, C. Heiliger, H. Over and B. M. Smarsly, *J Phys Chem C*, 2020, **124**, 8736-8748.
5. D. Andreescu, G. Bulbul, R. E. Ozel, A. Hayat, N. Sardesai and S. Andreescu, *Environ-Sci Nano*, 2014, **1**, 445-458.
6. J. Zhou, R. T. Guo, X. F. Zhang, Y. Z. Liu, C. P. Duan, G. L. Wu and W. G. Pan, *Energ Fuel*, 2021, **35**, 2981-2998.
7. E. Grulke, K. Reed, M. Beck, X. Huang, A. Cormack and S. Seal, *Environ Sci-Nano*, 2014, **1**, 429-444.
8. S. Banavar, A. Deshpande, S. Sur and S. Andreescu, *J Phys-Mater*, 2021, **4**.
9. M. A. Saifi, S. Seal and C. Godugu, *J Control Release*, 2021, **338**, 164-189.
10. A. Hayat, D. Andreescu, G. Bulbul and S. Andreescu, *J Colloid Interf Sci*, 2014, **418**, 240-245.
11. R. A. Yokel, S. Hussain, S. Garantziotis, P. Demokritou, V. Castranova and F. R. Cassee, *Environ Sci-Nano*, 2014, **1**, 406-428.
12. J. Ma, X. Tong, J. Wang, G. Zhang, Y. Lv, Y. Zhu, S. Sun, Y.-C. Yang and Y. Song, *Electrochimica Acta*, 2019, **229**, 80-88.
13. A. Trovarelli, *Catalysis by Ceria and Related Materials*, World Scientific Publishing Co Pte Ltd, 2002.
14. E. Mamontov and T. Egami, *Journal of Physics and Chemistry of Solids*, 2000, **61**, 1345-1356.
15. T. S. Sakthivel, D. L. Reid, U. M. Bhatta, G. Möbus, D. C. Sayle and S. Seal, *Nanoscale*, 2015, **7**, 5169-5177.
16. B. Choudhury and A. Choudhury, *Materials Chemistry and Physics*, 2012, **131**, 666-671.
17. S. Deshpande, S. Patil, S. V. Kuchibhatla and S. Seal, *Applied Physics Letters*, 2005, **87**, 133113.
18. S. Tsunekawa, R. Sivamohan, S. Ito, A. Kasuya and T. Fukuda, *Nanostructured materials*, 1999, **11**, 141-147.
19. S. Tsunekawa, R. Sahara, Y. Kawazoe and K. Ishikawa, *Applied surface science*, 1999, **152**, 53-56.
20. V. K. Paidi, L. Savereide, D. J. Childers, J. M. Notestein, C. A. Roberts and J. Van Lierop, *ACS applied materials & interfaces*, 2017, **9**, 30670-30678.
21. H.-Y. Li, H.-F. Wang, X.-Q. Gong, Y.-L. Guo, Y. Guo, G. Lu and P. Hu, *Physical Review B*, 2009, **79**, 193401.
22. M. Nolan, *Chemical Physics Letters*, 2010, **499**, 126-130.
23. M. Nolan, S. Grigoleit, D. C. Sayle, S. C. Parker and G. W. Watson, *Surface Science*, 2005, **576**, 217-229.
24. F. Esch, S. Fabris, L. Zhou, T. Montini, C. Africh, P. Fornasiero, G. Comelli and R. Rosei, *Science*, 2005, **309**, 752.
25. C. Zhang, A. Michaelides, D. A. King and S. J. Jenkins, *Physical Review B*, 2009, **79**, 075433.
26. S. C. Shirbhate, A. K. Yadav and S. A. Acharya, *Applied Physics Letters*, 2016, **108**, 143501.
27. Z. Yang, T. K. Woo, M. Baudin and K. Hermansson, *The Journal of chemical physics*, 2004, **120**, 7741-7749.
28. J. Kullgren, M. J. Wolf, C. Castleton, P. Mitev, W. J. Briels and K. Hermansson, *Physical review letters*, 2014, **112**, 156102.
29. S. Torbrügge, M. Reichling, A. Ishiyama, S. Morita and Ó. Custance, *Physical Review Letters*, 2007, **99**, 056101.
30. H. Nörenberg and G. A. D. Briggs, *Surface Science*, 1999, **424**, L352-L355.
31. Y. Namai, K.-i. Fukui and Y. Iwasawa, *The Journal of Physical Chemistry B*, 2003, **107**, 11666-11673.

32. G.-y. Adachi and N. Imanaka, *Chem Rev*, 1998, **98**, 1479-1514.
33. P. Knappe and L. Eyring, *Journal of Solid State Chemistry*, 1985, **58**, 312-324.
34. M. Yashima, D. Ishimura, Y. Yamaguchi, K. Ohoyama and K. Kawachi, *Chemical physics letters*, 2003, **372**, 784-787.
35. M. Zinkevich, D. Djurovic and F. Aldinger, *Solid State Ionics*, 2006, **177**, 989-1001.
36. O. T. Sørensen, *Journal of Solid State Chemistry*, 1976, **18**, 217-233.
37. E. Kümmerle and G. Heger, *Journal of Solid State Chemistry*, 1999, **147**, 485-500.
38. S. Ray and D. Cox, *Journal of Solid State Chemistry*, 1975, **15**, 333-343.
39. Y. Cao, L. Zhao, T. Gutmann, Y. Xu, L. Dong, G. Buntkowsky and F. Gao, *The Journal of Physical Chemistry C*, 2018, **122**, 20402-20409.
40. A. Trovarelli and J. Llorca, *ACS catalysis*, 2017, **7**, 4716-4735.
41. W. Wei-Wei, Y. Wen-Zhu, D. Pei-Pei, X. Hui, J. Zhao, S. Rui, M. Chao, S. Shuo, J. Chun-Jiang and Y. Chun-Hua, *Crystal Plane Effect of Ceria on Supported Copper Oxide Cluster Catalyst for CO Oxidation: Importance of Metal–Support Interaction*, 2017.
42. J. Conesa, *Surface Science*, 1995, **339**, 337-352.
43. M. M. Branda, R. M. Ferullo, M. Causa and F. Illas, *The Journal of Physical Chemistry C*, 2011, **115**, 3716-3721.
44. M. V. Ganduglia-Pirovano, A. Hofmann and J. Sauer, *Surface science reports*, 2007, **62**, 219-270.
45. D. R. Mullins, *Surface science reports*, 2015, **70**, 42-85.
46. D. R. Mullins, P. M. Albrecht and F. Calaza, *Topics in Catalysis*, 2013, **56**, 1345-1362.
47. M. Nolan, S. C. Parker and G. W. Watson, *Surface Science*, 2005, **595**, 223-232.
48. M. V. Ganduglia-Pirovano, J. L. F. Da Silva and J. Sauer, *Physical Review Letters*, 2009, **102**, 026101.
49. D. Zhang, X. Du, L. Shi and R. Gao, *Dalton transactions*, 2012, **41**, 14455-14475.
50. Q. Wu, F. Zhang, P. Xiao, H. Tao, X. Wang, Z. Hu and Y. Lü, *The Journal of Physical Chemistry C*, 2008, **112**, 17076-17080.
51. X. Liu, K. Zhou, L. Wang, B. Wang and Y. Li, *Journal of the American Chemical Society*, 2009, **131**, 3140-3141.
52. C. Pan, D. Zhang and L. Shi, *Journal of Solid State Chemistry*, 2008, **181**, 1298-1306.
53. S. Yang and L. Gao, *Journal of the American Chemical Society*, 2006, **128**, 9330-9331.
54. H.-I. Chen and H.-Y. Chang, *Solid state communications*, 2005, **133**, 593-598.
55. N. Du, H. Zhang, B. Chen, X. Ma and D. Yang, *The Journal of Physical Chemistry C*, 2007, **111**, 12677-12680.
56. J.-G. Li, T. Ikegami, Y. Wang and T. Mori, *Journal of the American Ceramic Society*, 2002, **85**, 2376-2378.
57. H.-Y. Chang and H.-I. Chen, *Journal of crystal growth*, 2005, **283**, 457-468.
58. M. Cabus-Llaurado, Y. Cesteros, F. Medina, P. Salagre and J. Sueiras, *Microporous and mesoporous materials*, 2007, **100**, 167-172.
59. H. Y. Ma, H. J. Ren, P. Koshy, C. C. Sorrell and J. N. Hart, *J Phys Chem C*, 2020, **124**, 2644-2655.
60. B. Tang, L. Zhuo, J. Ge, G. Wang, Z. Shi and J. Niu, *Chemical Communications*, 2005, 3565-3567.
61. Z. Yang, J. Wei, H. Yang, L. Liu, H. Liang and Y. Yang, *European Journal of Inorganic Chemistry*, 2010, **2010**, 3354-3359.
62. W.-Q. Han, L. Wu and Y. Zhu, *Journal of the American Chemical Society*, 2005, **127**, 12814-12815.
63. H.-X. Mai, L.-D. Sun, Y.-W. Zhang, R. Si, W. Feng, H.-P. Zhang, H.-C. Liu and C.-H. Yan, *The Journal of Physical Chemistry B*, 2005, **109**, 24380-24385.
64. G. Li, K. Chao, H. Peng, K. Chen and Z. Zhang, *The Journal of Physical Chemistry C*, 2008, **112**, 16452-16456.
65. Z.-R. Tang, Y. Zhang and Y.-J. Xu, *RSC Advances*, 2011, **1**, 1772-1777.
66. Z. Guo, F. Du, G. Li and Z. Cui, *Inorganic chemistry*, 2006, **45**, 4167-4169.

67. Y. Zhang, F. Hou and Y. Tan, *Chemical Communications*, 2012, **48**, 2391-2393.
68. K. W. Kolasinski, *Current Opinion in Solid State and Materials Science*, 2006, **10**, 182-191.
69. D. Wang, Y. Kang, V. Doan-Nguyen, J. Chen, R. Küngas, N. L. Wieder, K. Bakhmutsky, R. J. Gorte and C. B. Murray, *Angewandte Chemie International Edition*, 2011, **50**, 4378-4381.
70. X. Wang, J. Zhuang, Q. Peng and Y. Li, *Advanced Materials*, 2006, **18**, 2031-2034.
71. T. Yu, J. Joo, Y. I. Park and T. Hyeon, *Angewandte Chemie International Edition*, 2005, **44**, 7411-7414.
72. D. Zhang, F. Niu, H. Li, L. Shi and J. Fang, *Powder technology*, 2011, **207**, 35-41.
73. C. Sun, H. Li and L. Chen, *Energy & Environmental Science*, 2012, **5**, 8475-8505.
74. Q. Yuan, H.-H. Duan, L.-L. Li, L.-D. Sun, Y.-W. Zhang and C.-H. Yan, *J Colloid Interf Sci*, 2009, **335**, 151-167.
75. K. Wu, L. D. Sun and C. H. Yan, *Advanced Energy Materials*, 2016, **6**, 1600501.
76. I. Florea, C. d. Feral-Martin, J. r. Majimel, D. Ihiawakrim, C. Hirlimann and O. Ersen, *Crystal growth & design*, 2013, **13**, 1110-1121.
77. M. Nolan, *Journal of Materials Chemistry*, 2011, **21**, 9160-9168.
78. M. Nolan, V. S. Verdugo and H. Metiu, *Surface Science*, 2008, **602**, 2734-2742.
79. L. Wu, H. J. Wiesmann, A. R. Moodenbaugh, R. F. Klie, Y. Zhu, D. O. Welch and M. Suenaga, *Physical Review B*, 2004, **69**, 125415.
80. R. K. Hailstone, A. G. DiFrancesco, J. G. Leong, T. D. Allston and K. J. Reed, *The Journal of Physical Chemistry C*, 2009, **113**, 15155-15159.
81. J. Xu, J. Harmer, G. Li, T. Chapman, P. Collier, S. Longworth and S. C. Tsang, *Chemical Communications*, 2010, **46**, 1887-1889.
82. M. K. Ghosalya, X. S. Li, A. Beck, J. A. Van Bokhoven and L. Artiglia, *J Phys Chem C*, 2021, **125**, 9303-9309.
83. C. Paun, O. V. Safonova, J. Szlachetko, P. M. Abdala, M. Nachtegaal, J. Sa, E. Kleymenov, A. Cervellino, F. Krumeich and J. A. van Bokhoven, *The Journal of Physical Chemistry C*, 2012, **116**, 7312-7317.
84. X.-D. Zhou and W. Huebner, *Applied Physics Letters*, 2001, **79**, 3512-3514.
85. F. Zhang, S.-W. Chan, J. E. Spanier, E. Apak, Q. Jin, R. D. Robinson and I. P. Herman, *Applied Physics Letters*, 2002, **80**, 127-129.
86. J. Seo, A. Gowda and S. Babu, *ECS Journal of Solid State Science and Technology*, 2018, **7**, P243-P252.
87. J. Seo, J. Moon, J. H. Kim, K. Lee, J. Hwang, H. Yoon, D. K. Yi and U. Paik, *Applied surface science*, 2016, **389**, 311-315.
88. K. M. Kumar, M. Mahendhiran, M. C. Diaz, N. Hernandez-Como, A. Hernandez-Eligio, G. Torres-Torres, S. Godavarthi and L. M. Gomez, *Materials Letters*, 2018, **214**, 15-19.
89. B. Choudhury, P. Chetri and A. Choudhury, *Journal of Experimental Nanoscience*, 2015, **10**, 103-114.
90. G. N. Vayssilov, Y. Lykhach, A. Migani, T. Staudt, G. P. Petrova, N. Tsud, T. Skála, A. Bruix, F. Illas, K. C. Prince, V. r. Matolín, K. M. Neyman and J. Libuda, *Nature Materials*, 2011, **10**, 310.
91. P. Nachimuthu, W.-C. Shih, R.-S. Liu, L.-Y. Jang and J.-M. Chen, *Journal of Solid State Chemistry*, 2000, **149**, 408-413.
92. A. Migani, G. N. Vayssilov, S. T. Bromley, F. Illas and K. M. Neyman, *Journal of Materials Chemistry*, 2010, **20**, 10535-10546.
93. A. Bruix and K. M. Neyman, *Catalysis Letters*, 2016, **146**, 2053-2080.
94. M. A. Sk, S. M. Kozlov, K. H. Lim, A. Migani and K. M. Neyman, *Journal of Materials Chemistry A*, 2014, **2**, 18329-18338.
95. A. Ruiz Puigdollers, P. Schlexer, S. Tosoni and G. Pacchioni, *ACS catalysis*, 2017, **7**, 6493-6513.

96. M. Boaro, S. Colussi and A. Trovarelli, *Frontiers in chemistry*, 2019, **7**, 28.
97. H. J. Kim, M. G. Jang, D. Shin and J. W. Han, *ChemCatChem*, 2020, **12**, 11-26.
98. L. Mei, L. Zhaogang, H. Yanhong, W. Mitang and L. Hangquan, *Journal of Rare Earths*, 2008, **26**, 357-361.
99. C. Gunawan, M. S. Lord, E. Lovell, R. J. Wong, M. S. Jung, D. Oscar, R. Mann and R. Amal, *ACS omega*, 2019, **4**, 9473-9479.
100. D. A. Andersson, S. I. Simak, N. V. Skorodumova, I. A. Abrikosov and B. Johansson, *Proceedings of the National Academy of Sciences*, 2006, **103**, 3518-3521.
101. M. Coduri, S. Checchia, M. Longhi, D. Ceresoli and M. Scavini, *Frontiers in chemistry*, 2018, **6**, 526.
102. T. Vinodkumar, B. G. Rao and B. M. Reddy, *Catalysis Today*, 2015, **253**, 57-64.
103. D. Mukherjee and B. M. Reddy, *Catalysis Today*, 2018, **309**, 227-235.
104. C. Veranitisagul, N. Koonsaeng, N. Laosiripojana and A. Laobuthee, *journal of industrial and Engineering Chemistry*, 2012, **18**, 898-903.
105. U. Hennings and R. Reimert, *Applied Catalysis A: General*, 2007, **325**, 41-49.
106. D. N. Durgasri, T. Vinodkumar, P. Sudarsanam and B. M. Reddy, *Catalysis letters*, 2014, **144**, 971-979.
107. K. Krishna, A. Bueno-López, M. Makkee and J. Moulijn, *Applied Catalysis B: Environmental*, 2007, **75**, 189-200.
108. A. Bueno-López, *Applied Catalysis B: Environmental*, 2014, **146**, 1-11.
109. S. Patil, S. Seal, Y. Guo, A. Schulte and J. Norwood, *Applied Physics Letters*, 2006, **88**, 243110.
110. S. Babu, R. Thanneeru, T. Inerbaev, R. Day, A. E. Masunov, A. Schulte and S. Seal, *Nanotechnology*, 2009, **20**, 085713.
111. N. Shehata, K. Meehan, M. Hudait, N. Jain and S. Gaballah, *J. Nanomaterials*, 2014, **2014**, 156-156.
112. K. Kim, J. D. Yoo, S. Lee, M. Bae, J. Bae, W. Jung and J. W. Han, *ACS applied materials & interfaces*, 2017, **9**, 15449-15458.
113. I. Hemmilä, V.-M. Mukkala and H. Takalo, *Journal of Alloys and Compounds*, 1997, **249**, 158-162.
114. Q. Ma, J. Wang, Z. Li, X. Lv, L. Liang and Q. Yuan, *Small*, 2019, **15**, 1804969.
115. J. Wu, G. Wang, D. Jin, J. Yuan, Y. Guan and J. Piper, *Chemical Communications*, 2008, 365-367.
116. L. Li, H. K. Yang, B. K. Moon, Z. Fu, C. Guo, J. H. Jeong, S. S. Yi, K. Jang and H. S. Lee, *The Journal of Physical Chemistry C*, 2009, **113**, 610-617.
117. A. Kumar, S. Babu, A. S. Karakoti, A. Schulte and S. Seal, *Langmuir*, 2009, **25**, 10998-11007.
118. K. Woan, Y.-Y. Tsai and W. Sigmund, *Nanomedicine*, 2010, **5**, 233-242.
119. I. Celardo, M. De Nicola, C. Mandoli, J. Z. Pedersen, E. Traversa and L. Ghibelli, *ACS Nano*, 2011, **5**, 4537-4549.
120. N. O. Yang, P.; Bartolomeo, E.D.; Foglietti, V.; Piero Torelli, O.; Levlev, E.V.; Rossi, G.; Licoccia, S.; Balestrino, G.; Kalinin, S.V.; Aruta, C., *J. Phys. Chem. C*, 2017, **121**, 8841-8849.
121. N. Novik, V. Konakov and I. Y. Archakov, *Reviews on Advanced Materials Science*, 2015, **40**.
122. S. Damyanova, B. Pawelec, K. Arishtirova, M. V. M. Huerta and J. L. G. Fierro, *Applied Catalysis A: General*, 2008, **337**, 86-96.
123. T. Masui, T. Ozaki, K.-i. Machida and G.-y. Adachi, *Journal of Alloys and Compounds*, 2000, **303-304**, 49-55.
124. D. Devaiah, L. H. Reddy, S.-E. Park and B. M. Reddy, *Catalysis Reviews*, 2018, **60**, 177-277.
125. E. Aneggi, M. Boaro, S. Colussi, C. de Leitenburg and A. Trovarelli, in *Handbook on the Physics and Chemistry of Rare Earths*, eds. J.-C. G. Bünzli and V. K. Pecharsky, Elsevier, 2016, vol. 50, pp. 209-242.
126. N. Guillén-Hurtado, I. Atribak, A. Bueno-López and A. García-García, *Journal of Molecular Catalysis A: Chemical*, 2010, **323**, 52-58.
127. C. Hu, Q. Zhu, Z. Jiang, L. Chen and R. Wu, *Chemical Engineering Journal*, 2009, **152**, 583-590.

128. C. Hu, *Chemical Engineering Journal*, 2011, **168**, 1185-1192.
129. R. Qin, J. Chen, X. Gao, X. Zhu, X. Yu and K. Cen, *RSC Advances*, 2014, **4**, 43874-43881.
130. P. Venkataswamy, D. Mukherjee, D. Devaiah, M. Vithal and B. M. Reddy, *Current Nanomaterials*, 2018, **3**, 103-113.
131. S. Ramana, B. G. Rao, P. Venkataswamy, A. Rangaswamy and B. M. Reddy, *Journal of Molecular Catalysis A: Chemical*, 2016, **415**, 113-121.
132. W. Derafa, F. Paloukis, B. Mewafy, W. Baaziz, O. Ersen, C. Petit, G. Corbel and S. Zafeiratos, *RSC Advances*, 2018, **8**, 40712-40719.
133. A. J. M. Araújo, V. D. Silva, A. R. O. Sousa, J. P. F. Grilo, T. A. Simões, D. A. Macedo, R. M. Nascimento and C. A. Paskocimas, *Ceramics International*, 2019, **45**, 7157-7165.
134. A. Jha, D.-W. Jeong, Y.-L. Lee, I. W. Nah and H.-S. Roh, *RSC Advances*, 2015, **5**, 103023-103029.
135. A. A. Ansari, J. Labis, M. Alam, S. M. Ramay, N. Ahmad and A. Mahmood, *Phase Transitions*, 2016, **89**, 261-272.
136. Y. Wang, F. Wang, Y. Chen, D. Zhang, B. Li, S. Kang, X. Li and L. Cui, *Applied Catalysis B: Environmental*, 2014, **147**, 602-609.
137. M. O. Mazan, J. Marrero-Jerez, A. Soldati, P. Núñez and S. A. Larrondo, *International Journal of Hydrogen Energy*, 2015, **40**, 3981-3989.
138. J. Wang, B. Zhang, M. Shen, J. Wang, W. Wang, J. Ma, S. Liu and L. Jia, *Journal of Sol-Gel Science and Technology*, 2011, **58**, 259-268.
139. L. Kundakovic and M. Flytzani-Stephanopoulos, *Journal of Catalysis*, 1998, **179**, 203-221.
140. A. A. Ansari, J. P. Labis, M. Alam, S. M. Ramay, N. Ahmed and A. Mahmood, *Analytical Letters*, 2017, **50**, 1360-1371.
141. W. Tang, Z. Hu, M. Wang, G. D. Stucky, H. Metiu and E. W. McFarland, *Journal of Catalysis*, 2010, **273**, 125-137.
142. Y.-Q. Su, I. A. W. Filot, J.-X. Liu and E. J. M. Hensen, *ACS Catalysis*, 2018, **8**, 75-80.
143. S. Colussi, A. Gayen, M. Farnesi Camellone, M. Boaro, J. Llorca, S. Fabris and A. Trovarelli, *Angewandte Chemie International Edition*, 2009, **48**, 8481-8484.
144. E. Aneggi, C. de Leitenburg and A. Trovarelli, *Catalysis Today*, 2012, **181**, 108-115.
145. I. Atribak, A. Bueno-Lopez and A. Garcia-Garcia, *Topics in Catalysis*, 2009, **52**, 2088.
146. M. Konsolakis, S. A. C. Carabineiro, G. E. Marnellos, M. F. Asad, O. S. G. P. Soares, M. F. R. Pereira, J. J. M. Órfão and J. L. Figueiredo, *Inorganica Chimica Acta*, 2017, **455**, 473-482.
147. D. Marrocchelli, S. R. Bishop, H. L. Tuller and B. Yildiz, *Advanced Functional Materials*, 2012, **22**, 1958-1965.
148. R. Grau-Crespo, H. de Leeuw Nora, S. Hamad and V. Waghmare Umesh, *Proceedings of the Royal Society A: Mathematical, Physical and Engineering Sciences*, 2011, **467**, 1925-1938.
149. M. Yashima, *The Journal of Physical Chemistry C*, 2009, **113**, 12658-12662.
150. F. Capel, C. Moure and P. Durán, *Ceramics International*, 2002, **28**, 627-636.
151. M. Fu, L. Wei, Y. Li, X. Zhou, S. Hao and Y. Li, *Solid State Sciences*, 2009, **11**, 2133-2137.
152. X. Feng, D. C. Sayle, Z. L. Wang, M. S. Paras, B. Santora, A. C. Sutorik, T. X. T. Sayle, Y. Yang, Y. Ding, X. Wang and Y.-S. Her, *Science*, 2006, **312**, 1504.
153. A. Gupta, U. V. Waghmare and M. S. Hegde, *Chemistry of Materials*, 2010, **22**, 5184-5198.
154. U. Castanet, C. Feral-Martin, A. Demourgues, R. L. Neale, D. C. Sayle, F. Caddeo, J. M. Flitcroft, R. Caygill, B. J. Pointon, M. Molinari and J. Majimel, *ACS applied materials & interfaces*, 2019, **11**, 11384-11390.
155. A. Gupta, A. Kumar, U. V. Waghmare and M. S. Hegde, *Chemistry of Materials*, 2009, **21**, 4880-4891.
156. G. Dutta, U. V. Waghmare, T. Baidya, M. S. Hegde, K. R. Priolkar and P. R. Sarode, *Chemistry of Materials*, 2006, **18**, 3249-3256.

157. M. Nolan, *The Journal of Chemical Physics*, 2009, **130**, 144702.
158. Z. Yang, Z. Lu, G. Luo and K. Hermansson, *Physics Letters A*, 2007, **369**, 132-139.
159. M. Alfredsson and C. R. A. Catlow, *Physical Chemistry Chemical Physics*, 2002, **4**, 6100-6108.
160. M. D. Krcha, A. D. Mayernick and M. J. Janik, *Journal of catalysis*, 2012, **293**, 103-115.
161. A. Romero-Núñez and G. Díaz, *RSC Advances*, 2015, **5**, 54571-54579.
162. S. Gatla, D. Aubert, G. Agostini, O. Mathon, S. Pascarelli, T. Lunkenbein, M. G. Willinger and H. Kaper, *ACS Catalysis*, 2016, **6**, 6151-6155.
163. H. Zhu, Y. Chen, Z. Wang, W. Liu and L. Wang, *RSC Advances*, 2018, **8**, 14888-14897.
164. M. Mittal, A. Gupta and O. P. Pandey, *Solar Energy*, 2018, **165**, 206-216.
165. S. D. Senanayake, D. Stacchiola and J. A. Rodriguez, *Accounts of Chemical Research*, 2013, **46**, 1702-1711.
166. K. Mudiyanselage, S. D. Senanayake, L. Feria, S. Kundu, A. E. Baber, J. Graciani, A. B. Vidal, S. Agnoli, J. Evans, R. Chang, S. Axnanda, Z. Liu, J. F. Sanz, P. Liu, J. A. Rodriguez and D. J. Stacchiola, *Angewandte Chemie International Edition*, 2013, **52**, 5101-5105.
167. X. Wang, J. A. Rodriguez, J. C. Hanson, D. Gamarra, A. Martínez-Arias and M. Fernández-García, *The Journal of Physical Chemistry B*, 2006, **110**, 428-434.
168. R. Kopelent, J. A. van Bokhoven, J. Szlachetko, J. Edebeli, C. Paun, M. Nachtegaal and O. V. Safonova, *Angewandte Chemie International Edition*, 2015, **54**, 8728-8731.
169. A. S. Karakoti, N. A. Monteiro-Riviere, R. Aggarwal, J. P. Davis, R. J. Narayan, W. T. Self, J. McGinnis and S. Seal, *Jom-Us*, 2008, **60**, 33-37.
170. S. Das, J. M. Dowding, K. E. Klump, J. F. McGinnis, W. Self and S. Seal, *Nanomedicine*, 2013, **8**, 1483-1508.
171. C. Walkey, S. Das, S. Seal, J. Erlichman, K. Heckman, L. Ghibelli, E. Traversa, J. F. McGinnis and W. T. Self, *Environ Sci-Nano*, 2015, **2**, 33-53.
172. C. Korsvik, S. Patil, S. Seal and W. T. Self, *Chemical Communications*, 2007, 1056-1058.
173. T. Pirmohamed, J. M. Dowding, S. Singh, B. Wasserman, E. Heckert, A. S. Karakoti, J. E. S. King, S. Seal and W. T. Self, *Chemical Communications*, 2010, **46**, 2736-2738.
174. B. A. Rzigalinski, K. Meehan, R. M. Davis, Y. Xu, W. C. Miles and C. A. Cohen, *Nanomedicine*, 2006, **1**, 399-412.
175. M. Das, S. Patil, N. Bhargava, J.-F. Kang, L. M. Riedel, S. Seal and J. J. Hickman, *Biomaterials*, 2007, **28**, 1918-1925.
176. Y. Xue, Q. Luan, D. Yang, X. Yao and K. Zhou, *The Journal of Physical Chemistry C*, 2011, **115**, 4433-4438.
177. C. Li, X. Shi, Q. Shen, C. Guo, Z. Hou and J. Zhang, *Journal of Nanomaterials*, 2018, **2018**, 12.
178. B. C. Nelson, M. E. Johnson, M. L. Walker, K. R. Riley and C. M. Sims, *Antioxidants*, 2016, **5**, 15.
179. F. Pagliari, C. Mandoli, G. Forte, E. Magnani, S. Pagliari, G. Nardone, S. Licoccia, M. Minieri, P. Di Nardo and E. Traversa, *ACS Nano*, 2012, **6**, 3767-3775.
180. C. Xu and X. Qu, *Npg Asia Materials*, 2014, **6**, e90.
181. C. López-Alarcón and A. Denicola, *Analytica Chimica Acta*, 2013, **763**, 1-10.
182. B. Drew and C. Leeuwenburgh, *Annals of the New York Academy of Sciences*, 2002, **959**, 66-81.
183. B. Uttara, A. V. Singh, P. Zamboni and R. T. Mahajan, *Current Neuropharmacology*, 2009, **7**, 65-74.
184. J. M. McCord and I. Fridovich, *Journal of Biological Chemistry*, 1969, **244**, 6049-6055.
185. S. Singh, *Frontiers in chemistry*, 2019, **7**, 46.
186. T. Fukai and M. Ushio-Fukai, *Antioxidants & redox signaling*, 2011, **15**, 1583-1606.
187. E. G. Heckert, A. S. Karakoti, S. Seal and W. T. Self, *Biomaterials*, 2008, **29**, 2705-2709.
188. A. Karakoti, S. Singh, J. M. Dowding, S. Seal and W. T. Self, *Chem Soc Rev*, 2010, **39**, 4422-4432.
189. S. Singh, T. Dosani, A. S. Karakoti, A. Kumar, S. Seal and W. T. Self, *Biomaterials*, 2011, **32**, 6745-6753.

190. J. M. Perez, A. Asati, S. Nath and C. Kaittanis, *Small*, 2008, **4**, 552-556.
191. A. S. Karakoti, P. Munusamy, K. Hostetler, V. Kodali, S. Kuchibhatla, G. Orr, J. G. Pounds, J. G. Teeguarden, B. D. Thrall and D. R. Baer, *Surface and interface analysis*, 2012, **44**, 882-889.
192. B. Lipinski, *Oxidative Medicine and Cellular Longevity*, 2011, **2011**.
193. V. Prabhakaran, C. G. Arges and V. Ramani, *Proceedings of the National Academy of Sciences*, 2012, **109**, 1029-1034.
194. Y. Zhang, K. Zhou, Y. Zhai, F. Qin, L. Pan and X. Yao, *RSC Advances*, 2014, **4**, 50325-50330.
195. Y. Y. Huang, J. S. Ren and X. G. Qu, *Chem Rev*, 2019, **119**, 4357-4412.
196. D. W. Jiang, D. L. Ni, Z. T. Rosenkrans, P. Huang, X. Y. Yan and W. B. Cai, *Chem Soc Rev*, 2019, **48**, 3683-3704.
197. L. A. Ridnour, D. D. Thomas, D. Mancardi, M. G. Espey, K. M. Miranda, N. Paolocci, M. Feelisch, J. Fukuto and D. A. Wink, in *Biological Chemistry*, 2004, vol. 385, p. 1.
198. J. M. Dowding, T. Dosani, A. Kumar, S. Seal and W. T. Self, *Chemical Communications*, 2012, **48**, 4896-4898.
199. S. Singh, *Frontiers in chemistry*, 2019, **7**.
200. J. M. Dowding, S. Das, A. Kumar, T. Dosani, R. McCormack, A. Gupta, T. X. T. Sayle, D. C. Sayle, L. von Kalm, S. Seal and W. T. Self, *ACS Nano*, 2013, **7**, 4855-4868.
201. X. Jiao, H. Song, H. Zhao, W. Bai, L. Zhang and Y. Lv, *Analytical Methods*, 2012, **4**, 3261-3267.
202. P. Cohen, *Nature Cell Biology*, 2002, **4**, E127.
203. J. Chin, *Current Opinion in Chemical Biology*, 1997, **1**, 514-521.
204. S. J. Franklin, *Current Opinion in Chemical Biology*, 2001, **5**, 201-208.
205. F. Tan, Y. Zhang, J. Wang, J. Wei, Y. Cai and X. Qian, *Journal of Mass Spectrometry*, 2008, **43**, 628-632.
206. A. J. Patil, R. K. Kumar, N. J. Barron and S. Mann, *Chemical Communications*, 2012, **48**, 7934-7936.
207. M. H. Kuchma, C. B. Komanski, J. Colon, A. Teblum, A. E. Masunov, B. Alvarado, S. Babu, S. Seal, J. Summy and C. H. Baker, *Nanomedicine: Nanotechnology, Biology and Medicine*, 2010, **6**, 738-744.
208. H. J. Kwon, D. Kim, K. Seo, Y. G. Kim, S. I. Han, T. Kang, M. Soh and T. Hyeon, *Angewandte Chemie International Edition*, 2018, **57**, 9408-9412.
209. P. Eriksson, A. A. Tal, A. Skallberg, C. Brommesson, Z. Hu, R. D. Boyd, W. Olovsson, N. Fairley, I. A. Abrikosov, X. Zhang and K. Uvdal, *Scientific Reports*, 2018, **8**, 6999.
210. M. Huang and S. Fabris, *Physical Review B*, 2007, **75**, 081404.
211. X. Huang and M. J. Beck, *Chemistry of Materials*, 2015, **27**, 5840-5844.
212. Z. Wu, M. Li, J. Howe, H. M. Meyer III and S. H. Overbury, *Langmuir*, 2010, **26**, 16595-16606.
213. G. Preda, A. Migani, K. M. Neyman, S. T. Bromley, F. Illas and G. Pacchioni, *The Journal of Physical Chemistry C*, 2011, **115**, 5817-5822.
214. S. Fabris, G. Vicario, G. Balducci, S. de Gironcoli and S. Baroni, *The Journal of Physical Chemistry B*, 2005, **109**, 22860-22867.
215. V. V. Pushkarev, V. I. Kovalchuk and J. L. d'Itri, *The Journal of Physical Chemistry B*, 2004, **108**, 5341-5348.
216. C. Li, K. Domen, K.-I. Maruya and T. Onishi, *Journal of Catalysis*, 1990, **123**, 436-442.
217. Y. M. Choi, H. Abernathy, H.-T. Chen, M. C. Lin and M. Liu, *ChemPhysChem*, 2006, **7**, 1957-1963.
218. C. Loschen, A. Migani, S. T. Bromley, F. Illas and K. M. Neyman, *Physical Chemistry Chemical Physics*, 2008, **10**, 5730-5738.
219. C. Li, K. Domen, K. Maruya and T. Onishi, *Journal of the American Chemical Society*, 1989, **111**, 7683-7687.
220. Z. Wu, M. Li, J. Howe, H. M. Meyer and S. H. Overbury, *Langmuir*, 2010, **26**, 16595-16606.
221. F. Vindigni, M. Manzoli, A. Damin, T. Tabakova and A. Zecchina, *Chemistry–A European Journal*, 2011, **17**, 4356-4361.

222. C. Yang, X. Yu, S. Heissler, P. G. Weidler, A. Nefedov, Y. Wang, C. Woell, T. Kropp, J. Paier and J. Sauer, *Angewandte Chemie International Edition*, 2017, **56**, 16399-16404.
223. H.-T. Chen, J.-G. Chang, H.-L. Chen and S.-P. Ju, *Journal of Computational Chemistry*, 2009, **30**, 2433-2442.
224. M. Ornatska, E. Sharpe, D. Andreescu and S. Andreescu, *Analytical chemistry*, 2011, **83**, 4273-4280.
225. S. S. Lee, W. Song, M. Cho, H. L. Puppala, P. Nguyen, H. Zhu, L. Segatori and V. L. Colvin, *ACS Nano*, 2013, **7**, 9693-9703.
226. S. Saraf, C. J. Neal, S. Das, S. Barkam, R. McCormack and S. Seal, *ACS Applied Materials & Interfaces*, 2014, **6**, 5472-5482.
227. P. Yu, S. A. Hayes, T. J. O'Keefe, M. J. O'Keefe and J. O. Stoffer, *Journal of The Electrochemical Society*, 2006, **153**, C74-C79.
228. F. H. Scholes, C. Soste, A. E. Hughes, S. G. Hardin and P. R. Curtis, *Applied Surface Science*, 2006, **253**, 1770-1780.
229. M. Ornatska, E. Sharpe, D. Andreescu and S. Andreescu, *Anal Chem*, 2011, **83**, 4273-4280.
230. N. P. Sardesai, D. Andreescu and S. Andreescu, *Journal of the American Chemical Society*, 2013, **135**, 16770-16773.
231. Y.-J. Wang, H. Dong, G.-M. Lyu, H.-Y. Zhang, J. Ke, L.-Q. Kang, J.-L. Teng, L.-D. Sun, R. Si, J. Zhang, Y.-J. Liu, Y.-W. Zhang, Y.-H. Huang and C.-H. Yan, *Nanoscale*, 2015, **7**, 13981-13990.
232. D. Damatov and J. M. Mayer, *Chemical Communications*, 2016, **52**, 10281-10284.
233. K. Binnemans, P. T. Jones, K. Van Acker, B. Blanpain, B. Mishra and D. Apelian, *Jom-Us*, 2013, **65**, 846-848.
234. G. A. Campbell, *Mineral Economics*, 2014, **27**, 21-31.
235. K. Binnemans, P. T. Jones, B. Blanpain, T. Van Gerven, Y. Yang, A. Walton and M. Buchert, *Journal of Cleaner Production*, 2013, **51**, 1-22.
236. S. Jakab, S. Picart, B. Tribollet, P. Rousseau, H. Perrot and C. Gabrielli, *Analytical Chemistry*, 2009, **81**, 5139-5145.
237. X. Beaudoux, M. Virot, T. Chave, G. Durand, G. Leturcq and S. I. Nikitenko, *Green Chemistry*, 2016, **18**, 3656-3668.
238. M. Virot, T. Chave, D. Horlait, N. Clavier, N. Dacheux, J. Ravaux and S. I. Nikitenko, *Journal of Materials Chemistry*, 2012, **22**, 14734-14740.
239. S. Tamilmani, V. Lowalekar, S. Raghavan and R. Small, 7th International Symposium on Ultra Clean Processing of Silicon Surfaces, UCPSS 2004, 2005.
240. *US Pat.*, US6568995B1, 2003.
241. *US Pat.*, US6326305 B1, 2001.
242. N. Um, M. Miyake and T. Hirato, Tokyo, 2011.
243. D. Horlait, N. Clavier, S. Szenknect, N. Dacheux and V. Dubois, *Inorganic chemistry*, 2012, **51**, 3868-3878.
244. K. Dhamodharan, T. Aneesh and A. Pius, *Journal of Radioanalytical and Nuclear Chemistry*, 2019, **319**, 1127-1133.
245. J. T. Dahle, K. Livi and Y. Arai, *Chemosphere*, 2015, **119**, 1365-1371.
246. M. S. A. Asghar, B. J. Inkson and G. Möbus, *ChemPhysChem*, 2017, **18**, 1247-1251.
247. P. Janos, P. Kuran, M. Kormunda, V. Stengl, T. M. Grygar, M. Dosek, M. Stastny, J. Ederer, V. Pilarova and L. Vrtoch, *Journal of Rare Earths*, 2014, **32**, 360-370.
248. P. Janoš, J. Ederer and M. Došek, 2014, **13**, 148.
249. P. Janoš, P. Kuráň, J. Ederer, M. Šťastný, L. Vrtoch, M. Pšenička, J. Henych, K. Mazanec and M. Skoumal, *Advances in Materials Science and Engineering*, 2015, **2015**.
250. W. Kim, B. Kim, D. Choi, T. Oki and S. Kim, *Journal of Hazardous Materials*, 2010, **183**, 29-34.

251. Y. Xu, S. S. Mofarah, R. Mehmood, C. Cazorla, P. Koshy and C. C. Sorrell, *Materials horizons*, 2021, **8**, 102-123.
252. Y. Shlapa, S. Solopan, V. Sarnatskaya, K. Siposova, I. Garcarova, K. Veltruska, I. Timashkov, O. Lykhova, D. Kolesnik, A. Musatov, V. Nikolaev and A. Belous, *Colloids and Surfaces B: Biointerfaces*, 2022, **220**, 112960.
253. M. Nyoka, Y. Choonara, P. Kumar, P. P. D. Kondiah and V. Pillay, *Nanomaterials*, 2020, **10(2)**, 242.
254. T. Yu, J. Joo, Y. I. Park and T. Hyeon, *Angewandte Chemie*, 2005, **44**, 7411-7414.
255. V. D. Araújo, W. Avansi, H. B. de Carvalho, M. L. Moreira, E. Longo, C. Ribeirod and M. I. B. Bernardia, *CrystEngComm*, 2012, **14,**, 1150-1154.
256. S. Kar, C. Patel and S. Santra, *J. Phys. Chem. C.*, 2009, **113**, 4862-4867.
257. A. F. Zedan, S. Moussa and M. S. El-Shall, *Materials Research Express*, 2023, **10**.
258. K. R. Singh, V. Nayak, T. Sarkar and R. P. Singh, *RSC Adv*, 2020, **10**, 27194-27214.
259. R. Olbrich, G. E. Murgida, V. Ferrari, C. Barth, A. M. Llois, M. Reichling and M. V. Ganduglia-Pirovano, *J. Phys. Chem. C* 2017, **121**, 6844-6851.
260. Z. Nie, A. Petukhova and E. Kumacheva, *Nature Nanotechnology*, 2009, **5**, 15.
261. W.-J. Ong, L.-L. Tan, S.-P. Chai and S.-T. Yong, *Chemical Communications*, 2015, **51**, 858-861.
262. Z. Ji, X. Shen, M. Li, H. Zhou, G. Zhu and K. Chen, *Nanotechnology*, 2013, **24**, 115603.
263. M. E. Khan, M. M. Khan and M. H. Cho, *Scientific Reports*, 2017, **7**, 5928.
264. A. S. Dezfuli, M. R. Ganjali, H. R. Naderi and P. Norouzi, *RSC Advances*, 2015, **5**, 46050-46058.
265. D. Joung, V. Singh, S. Park, A. Schulte, S. Seal and S. I. Khondaker, *J Phys Chem C*, 2011, **115**, 24494-24500.
266. Y. Wang, C. X. Guo, J. Liu, T. Chen, H. Yang and C. M. Li, *Dalton Transactions*, 2011, **40**, 6388-6391.
267. M. M. Khan, S. A. Ansari, D. Pradhan, D. H. Han, J. Lee and M. H. Cho, *Industrial & Engineering Chemistry Research*, 2014, **53**, 9754-9763.
268. D. Joung, V. Singh, S. Park, A. Schulte, S. Seal and S. I. Khondaker, *The Journal of Physical Chemistry C*, 2011, **115**, 24494-24500.
269. A. Othman, E. Dumitrescu, D. Andreescu and S. Andreescu, *ACS Sustainable Chemistry & Engineering*, 2018, **6**, 12542-12561.
270. L. Yu, Y. Ma, C. N. Ong, J. Xie and Y. Liu, *RSC Advances*, 2015, **5**, 64983-64990.
271. A. Baranik, R. Sitko, A. Gagor, I. Queralt, E. Marguí and B. Zawisza, *Analytical Chemistry*, 2018, **90**, 4150-4159.
272. T. S. Sakthivel, S. Das, C. J. Pratt and S. Seal, *Nanoscale*, 2017, **9**, 3367-3374.
273. A. Szabó, C. Perri, A. Csató, G. Giordano, D. Vuono and J. B. Nagy, *Materials*, 2010, **3**, 3092-3140.
274. X. Qin, F. Peng, F. Yang, X. He, H. Huang, D. Luo, J. Yang, S. Wang, H. Liu, L. Peng and Y. Li, *Nano Letters*, 2014, **14**, 512-517.
275. S. Sarkar, E. Guibal, F. Quignard and A. K. SenGupta, *Journal of Nanoparticle Research*, 2012, **14**, 715.
276. S. Wu, J. Dzubiella, J. Kaiser, M. Drechsler, X. Guo, M. Ballauff and Y. Lu, *Angewandte Chemie International Edition*, 2012, **51**, 2229-2233.
277. A. Asati, S. Santra, C. Kaittanis and J. M. Perez, *ACS Nano*, 2010, **4**, 5321-5331.
278. W. Song, S. Soo Lee, M. Savini, L. Popp, V. L. Colvin and L. Segatori, *ACS Nano*, 2014, **8**, 10328-10342.
279. R. Mehmood, S. S. Mofarah, A. Rawal, F. Tomasetig, X. C. Wang, J. L. Yang, P. Koshy and C. C. Sorrell, *Acs Sustainable Chemistry & Engineering*, 2019, **7**, 9189-9201.
280. M. Mari, B. Müller, K. Landfester and R. Muñoz-Espí, *ACS Applied Materials & Interfaces*, 2015, **7**, 10727-10733.
281. K. Katta, D. Busko, Y. Avlasevich, K. Landfester, S. Baluschev and R. Muñoz-Espí, *Beilstein Journal of Nanotechnology* 2019, **10**, 522–530.

282. M. E. Culica, A. L. Chibac-Scutaru, V. Melinte and S. Coseri, *Materials (Basel)*, 2020, **13**.
283. R. Cao, D. Sun, Y. Liang, M. Hong, K. Tatsumi and Q. Shi, *Inorganic Chemistry*, 2002, **41**, 2087-2094.
284. R. Mohammadinasab, M. Tabatabaee, B.-M. Kukovec and H. Aghaie, *Inorganica Chimica Acta*, 2013, **405**, 368-373.
285. P. Gohari Derakhshandeh and J. Soleimannejad, *Ultrasonics Sonochemistry*, 2016, **31**, 122-128.
286. A. K. Boal, F. Ilhan, J. E. DeRouchey, T. Thurn-Albrecht, T. P. Russell and V. M. Rotello, *Nature*, 2000, **404**, 746-748.
287. L. Qi, J. Fresnais, P. Muller, O. Theodoly, J. F. Berret and J. P. Chapel, *Langmuir*, 2012, **28**, 11448-11456.
288. Z. Shen, J. Liu, F. Hu, S. Liu, N. Cao, Y. Sui, Q. Zeng and Y. Shen, *CrystEngComm*, 2014, **16**, 3387-3394.
289. P. G. Derakhshandeh, J. Soleimannejad and J. Janczak, *Ultrasonics Sonochemistry*, 2015, **26**, 273-280.
290. Z. Shen, S. He, P. Yao, X. Lao, B. Yang, Y. Dai, X. Sun and T. Chen, *RSC Advances*, 2014, **4**, 12844-12848.
291. A. U. Czaja, N. Trukhan and U. Müller, *Chem Soc Rev*, 2009, **38**, 1284-1293.
292. W. P. Mounfield, U. Tumuluri, Y. Jiao, M. Li, S. Dai, Z. Wu and K. S. Walton, *Microporous and Mesoporous Materials*, 2016, **227**, 65-75.
293. M. Lammert, M. T. Wharmby, S. Smolders, B. Bueken, A. Lieb, K. A. Lomachenko, D. D. Vos and N. Stock, *Chemical Communications*, 2015, **51**, 12578-12581.
294. T. Islamoglu, A. Atilgan, S.-Y. Moon, G. W. Peterson, J. B. DeCoste, M. Hall, J. T. Hupp and O. K. Farha, *Chemistry of Materials*, 2017, **29**, 2672-2675.
295. A. M. Ebrahim and T. J. Bandosz, *ACS Applied Materials & Interfaces*, 2013, **5**, 10565-10573.
296. J. Qi, J. Chen, G. Li, S. Li, Y. Gao and Z. Tang, *Energy & Environmental Science*, 2012, **5**, 8937-8941.
297. T. K. Kim, K. J. Lee, J. Y. Cheon, J. H. Lee, S. H. Joo and H. R. Moon, *Journal of the American Chemical Society*, 2013, **135**, 8940-8946.
298. H. Wang, M. Liu, S. Guo, Y. Wang, X. Han and Y. Bai, *Molecular Catalysis*, 2017, **436**, 120-127.
299. Z. Zhang, H. Shi, Q. Wu, X. Bu, Y. Yang, J. Zhang and Y. Huang, *New Journal of Chemistry*, 2019, **43**, 4581-4589.
300. M. H. Hassan, D. Andreescu and S. Andreescu, *Acs Appl Nano Mater*, 2020, **3**, 3288-3294.
301. J. M. Thomas, *The Journal of Chemical Physics*, 2008, **128**, 182502.
302. J. Zhang, L. P. Li, X. S. Huang and G. S. Li, *Journal of Materials Chemistry*, 2012, **22**, 10480-10487.
303. J. Qi, J. Chen, G. D. Li, S. X. Li, Y. Gao and Z. Y. Tang, *Energy & Environmental Science*, 2012, **5**, 8937-8941.
304. S. Song, X. Wang and H. Zhang, *Npg Asia Materials*, 2015, **7**, e179.
305. A. Figueroba, A. Bruix, G. Kovács and K. M. Neyman, *Physical Chemistry Chemical Physics*, 2017, **19**, 21729-21738.
306. N. Acerbi, S. Golunski, S. C. Tsang, H. Daly, C. Hardacre, R. Smith and P. Collier, *The Journal of Physical Chemistry C*, 2012, **116**, 13569-13583.
307. E. A. Derevyannikova, T. Y. Kardash, L. S. Kibis, E. M. Slavinskaya, V. A. Svetlichnyi, O. A. Stonkus, A. S. Ivanova and A. I. Boronin, *Physical Chemistry Chemical Physics*, 2017, **19**, 31883-31897.
308. L. Wang, H. He, Y. Yu, L. Sun, S. Liu, C. Zhang and L. He, *Journal of Inorganic Biochemistry*, 2014, **135**, 45-53.
309. C. M. Magdalane, K. Kaviyarasu, J. J. Vijaya, B. Siddhardha and B. Jeyaraj, *Journal of Photochemistry and Photobiology B: Biology*, 2016, **163**, 77-86.
310. R. Kannan, A. R. Kim, S. K. Eo, S. H. Kang and D. J. Yoo, *Ceramics International*, 2017, **43**, 3072-3079.
311. Z. Kebin and L. Yadong, *Angewandte Chemie International Edition*, 2012, **51**, 602-613.

312. M. Krishnan, J. W. Nalaskowski and L. M. Cook, *Chem Rev*, 2010, **110**, 178-204.
313. S. Park, J. M. Vohs and R. J. Gorte, *Nature*, 2000, **404**, 265.
314. P. Jasinski, T. Suzuki and H. U. Anderson, *Sensors and Actuators B: Chemical*, 2003, **95**, 73-77.
315. L. Truffault, M.-T. Ta, T. Devers, K. Konstantinov, V. Harel, C. Simmonard, C. Andreazza, I. P. Nevirkovets, A. Pineau, O. Veron and J.-P. Blondeau, *Materials Research Bulletin*, 2010, **45**, 527-535.
316. F. Caputo, M. Mameli, A. Sienkiewicz, S. Licoccia, F. Stellacci, L. Ghibelli and E. Traversa, *Scientific Reports*, 2017, **7**, 4636.
317. U. Tumuluri, G. Rother and Z. Wu, *Industrial & Engineering Chemistry Research*, 2016, **55**, 3909-3919.
318. J. A. Rodriguez, D. C. Grinter, Z. Liu, R. M. Palomino and S. D. Senanayake, *Chem Soc Rev*, 2017, **46**, 1824-1841.
319. *Catalysis Reviews*, 1996, **38**, 439-520.
320. K. Polychronopoulou, A. F. Zedan, M. AlKetbi, S. Stephen, M. Ather, M. S. Katsiotis, J. Arvanitidis, D. Christofilos, A. F. Isakovic and S. AlHassan, *Journal of Environmental Chemical Engineering*, 2018, **6**, 266-280.
321. J. Zhang, Y. Cao, C.-A. Wang and R. Ran, *ACS Applied Materials & Interfaces*, 2016, **8**, 8670-8677.
322. S. H. Kim, B. C. Park, Y. S. Jeon and Y. K. Kim, *ACS Applied Materials & Interfaces*, 2018, **10**, 32112-32119.
323. J. Quiroz, J.-M. Giraudon, A. Gervasini, C. Dujardin, C. Lancelot, M. Trentesaux and J.-F. Lamonier, *ACS Catalysis*, 2015, **5**, 2260-2269.
324. L. Song, T. Xu, D. Gao, X. Hu, C. Li, S. Li and G. Chen, *Chemistry – A European Journal*, **0**.
325. M. Dubey, S. Wadhwa, A. Mathur and R. Kumar, *Applied Surface Science Advances*, 2022, **12**, 100340.
326. Y. Mordekovitz, L. Shelly, B. A. Rosen and S. Hayun, *Journal of the American Ceramic Society*, 2021, **104**, 2337-2347.
327. S. Zhang, C. Zhao, Y. Liu, W. Li, J. Wang, G. Wang, Y. Zhang, H. Zhang and H. Zhao, *Chemical Communications*, 2019, **55**, 2952-2955.
328. I. Y. Habib, J. Burhan, F. Jaladi, C. M. Lim, A. Usman, N. T. R. N. Kumara, S. C. E. Tsang and A. H. Mahadi, *Catalysis Today*, 2021, **375**, 506-513.
329. K. Polychronopoulou, A. A. AlKhoori, A. M. Efstathiou, M. A. Jaoude, C. M. Damaskinos, M. A. Baker, A. Almutawa, D. H. Anjum, M. A. Vasiliades, A. Belabbes, L. F. Vega, A. F. Zedan and S. J. Hinder, *ACS Applied Materials & Interfaces*, 2021, **13**, 22391-22415.
330. H. A. Aleksandrov, I. Z. Koleva, K. M. Neyman, T. T. Tabakova and G. N. Vayssilov, *RSC Advances*, 2018, **8**, 33728-33741.
331. K. Kuntaiah, P. Sudarsanam, B. M. Reddy and A. Vinu, *RSC Advances*, 2013, **3**, 7953-7962.
332. A. Chien, N. Ye, C. W. Huang and I. H. Tseng, *Catalysts*, 2021, **11**, 731.
333. N. Sutradhar, A. Sinhamahapatra, S. Pahari, M. Jayachandran, B. Subramanian, H. C. Bajaj and A. B. Panda, *The Journal of Physical Chemistry C*, 2011, **115**, 7628-7637.
334. J. Liu and C. Zhu, 2021, **11**.
335. A. A. Aboud, H. Al-Kelesh, W. M. A. E. Rouby, A. A. Farghali, A. Hamdedein and M. H. Khedr, *Journal of Materials Research and Technology*, 2018, **7**, 14-20.
336. G. Jayakumar, A. Albert Irudayaraj, A. Dhayal Raj, S. John Sundaram and K. Kaviyarasu, *Journal of Physics and Chemistry of Solids*, 2022, **160**, 110369.
337. M. Makkee and J. A. Moulijn, *Catalysis Reviews*, 2001, **43**, 489-564.
338. P. Sudarsanam, K. Kuntaiah and B. M. Reddy, *New Journal of Chemistry*, 2014, **38**, 5991-6001.
339. L. F. Nascimento, J. F. Lima, P. C. de Sousa Filho and O. A. Serra, *Chemical Engineering Journal*, 2016, **290**, 454-464.

340. Q. Shen, G. Lu, C. Du, Y. Guo, Y. Wang, Y. Guo and X. Gong, *Chemical Engineering Journal*, 2013, **218**, 164-172.
341. B. Suryadevara, *Advances in chemical mechanical planarization (CMP)*, Woodhead Publishing, 2016.
342. P. V. Dandu, B. Peethala and S. Babu, *Journal of The Electrochemical Society*, 2010, **157**, H869-H874.
343. N. K. Penta, B. Peethala, H. Amanapu, A. Melman and S. Babu, *Colloids and Surfaces A: Physicochemical and Engineering Aspects*, 2013, **429**, 67-73.
344. R. Srinivasan, P. V. Dandu and S. Babu, *ECS Journal of Solid State Science and Technology*, 2015, **4**, P5029-P5039.
345. P. D. Veera, S. Peddeti and S. Babu, *Journal of The Electrochemical Society*, 2009, **156**, H936-H943.
346. J. Seo, J. Moon, J.-Y. Bae, K. S. Yoon, W. Sigmund and U. Paik, *Journal of nanoscience and nanotechnology*, 2014, **14**, 4351-4356.
347. R. Sabia and H. J. Stevens, *Machining science and technology*, 2000, **4**, 235-251.
348. H. Doi, M. Suzuki and K. Kinuta, Proceedings of International Conference on Planarization/CMP Technology 2014, 2014.
349. L. M. Cook, *Journal of Non-Crystalline Solids*, 1990, **120**, 152-171.
350. S. R. Alety, K. V. Sagi and S. Babu, *ECS Journal of Solid State Science and Technology*, 2017, **6**, P898.
351. J. Seo, J. W. Lee, J. Moon, W. Sigmund and U. Paik, *ACS applied materials & interfaces*, 2014, **6**, 7388-7394.
352. J.-S. Kim, H.-G. Kang, M. Kanemoto, U. Paik and J.-G. Park, *Japanese Journal of Applied Physics*, 2007, **46**, 7671.
353. P. Janoš, J. Ederer, V. Pilařová, J. Henych, J. Tolasz, D. Milde and T. Opletal, *Wear*, 2016, **362**, 114-120.
354. S.-K. Kim, Y.-H. Kim, U. Paik and J.-G. Park, *Journal of The Electrochemical Society*, 2007, **154**, H642-H646.
355. D. Ryuzaki, Y. Hoshi, Y. Machii, N. Koyama, H. Sakurai and T. Ashizawa, 2009 Symposium on VLSI Technology, 2009.
356. H.-G. Kang, J.-D. Koh, S.-W. Han, J. W. Lee, B.-G. Lee, S.-H. Pyi, B.-S. Lee, J.-W. Kim, B. Reiss and J.-D. Jeong, ICPT 2012-International Conference on Planarization/CMP Technology, 2012.
357. *USA Pat.*, 2014.
358. *USA Pat.*, 2012.
359. A. Chen, J. Long, Z. Li and Y. Chen, *Journal of Materials Science: Materials in Electronics*, 2018, **29**, 11466-11477.
360. Y. Chen, C. Zuo, Z. Li and A. Chen, *Journal of Alloys and Compounds*, 2018, **736**, 276-288.
361. Y. Chen, W. Cai, W. Wang and A. Chen, *Journal of Nanoparticle Research*, 2019, **21**, 226.
362. Y. Chen, Z. Li and N. Miao, *Tribology International*, 2015, **82**, 211-217.
363. Y. Chen and R. Long, *Applied surface science*, 2011, **257**, 8679-8685.
364. K. Kim, J. Seo, M. Lee, J. Moon, K. Lee, D. K. Yi and U. Paik, *Journal of Materials Research*, 2017, **32**, 2829-2836.
365. N. D. Urban, D. Dickmann, B. Her and B. Santora, *ECS Transactions*, 2016, **72**, 37-42.
366. J. Choe, *Comparison of 20 nm & 10 nm-class 2D Planar NAND and 3D V-NAND Architecture*, Techinsights, 2015.
367. T. C. Li, B. Reiss, S. P. Kuttiatoor, V. Lam, J.-D. Lee and R. Jia, 2015 International Conference on Planarization/CMP Technology (ICPT), 2015.
368. B. Praveen, B.-J. Cho, J.-G. Park and S. Ramanathan, *Materials Science in Semiconductor Processing*, 2015, **33**, 161-168.
369. J. Cheng, S. Huang, Y. Li, T. Wang, L. Xie and X. Lu, *Applied Surface Science*, 2020, **506**, 144668.

370. X. Feng, Y.-S. Her and Y. Mao, Google Patents, 2005.
371. X. Feng, D. C. Sayle, Z. L. Wang, M. S. Paras, B. Santora, A. C. Sutorik, T. X. Sayle, Y. Yang, Y. Ding and X. Wang, *Science*, 2006, **312**, 1504-1508.
372. B. W. Liu and J. W. Liu, *Trac-Trend Anal Chem*, 2019, **121**.
373. D. Jampaiah, T. Srinivasa Reddy, V. E. Coyle, A. Nafady and S. K. Bhargava, *Journal of Materials Chemistry B*, 2017, **5**, 720-730.
374. Y. Tao, E. Ju, J. Ren and X. Qu, *Advanced Materials*, 2015, **27**, 1097-1104.
375. A. S. Finny, A. Othman and S. Andreescu, in *Cerium Oxide (CeO_2): Synthesis, Properties and Applications*, eds. S. Scirè and L. Palmisano, Elsevier, 2020, pp. 259-277.
376. A. Othman, A. Karimi and S. Andreescu, *Journal of Materials Chemistry B*, 2016, **4**, 7178-7203.
377. A. Karimi, A. Othman, A. Uzunoglu, L. Stanciu and S. Andreescu, *Nanoscale*, 2015, **7**, 6909-6923.
378. J. Wu, X. Wang, Q. Wang, Z. Lou, S. Li, Y. Zhu, L. Qin and H. Wei, *Chem Soc Rev*, 2019, **48**, 1004-1076.
379. H. Wei and E. Wang, *Chem Soc Rev*, 2013, **42**, 6060-6093.
380. L. Song, C. Huang, W. Zhang, M. Ma, Z. Chen, N. Gu and Y. Zhang, *Colloids and Surfaces A: Physicochemical and Engineering Aspects*, 2016, **506**, 747-755.
381. Y.-Z. Li, T.-T. Li, W. Chen and Y.-Y. Song, *ACS Applied Materials & Interfaces*, 2017, **9**, 29881-29888.
382. C. Hou, Y. Wang, Q. Ding, L. Jiang, M. Li, W. Zhu, D. Pan, H. Zhu and M. Liu, *Nanoscale*, 2015, **7**, 18770-18779.
383. L. Ai, L. Li, C. Zhang, J. Fu and J. Jiang, *Chemistry – A European Journal*, 2013, **19**, 15105-15108.
384. S. Kumar, P. Bhushan and S. Bhattacharya, *RSC Advances*, 2017, **7**, 37568-37577.
385. Y.-W. Bao, X.-W. Hua, H.-H. Ran, J. Zeng and F.-G. Wu, *Journal of Materials Chemistry B*, 2019, **7**, 296-304.
386. H. Sun, Y. Zhou, J. Ren and X. Qu, *Angewandte Chemie International Edition*, 2018, **57**, 9224-9237.
387. I. Celardo, J. Z. Pedersen, E. Traversa and L. Ghibelli, *Nanoscale*, 2011, **3**, 1411-1420.
388. A. A. Ansari, P. R. Solanki and B. D. Malhotra, *J Biotechnol*, 2009, **142**, 179-184.
389. J. M. Yong, L. Fu, F. Tang, P. Yu, R. P. Kuchel, J. M. Whitelock and M. S. Lord, 2022, **8**, 512-525.
390. C. Ispas, J. Njagi, M. Cates and S. Andreescu, *Journal of the Electrochemical Society* 2008, **155 (8),**, F169.
391. H. Wu, F. Li, S. Wang, J. Lu, J. Li, Y. Du, X. Sun, X. Chen, J. Gao and D. Ling, *Biomaterials*, 2018, **151**, 66-77.
392. S. M. Hirst, A. S. Karakoti, R. D. Tyler, N. Sriranganathan, S. Seal and C. M. Reilly, *Small*, 2009, **5**, 2848-2856.
393. K. Chaudhury, N. Babu K, A. K. Singh, S. Das, A. Kumar and S. Seal, *Nanomedicine: Nanotechnology, Biology and Medicine*, 2013, **9**, 439-448.
394. D. Zahra, A. Javaid, M. Iqbal, I. Akbar and U. A. Ashfaq, *Critical reviews in therapeutic drug carrier systems*, 2021, **38**, 1-26.
395. Y. Gao, K. Chen, J.-L. Ma and F. Gao, *OncoTargets and therapy*, 2014, **7**, 835-840.
396. N. Pourkhalili, A. Hosseini, A. Nili-Ahmadabadi, S. Hassani, M. Pakzad, M. Baeeri, A. Mohammadirad and M. Abdollahi, *World journal of diabetes*, 2011, **2**, 204-210.
397. R. Najafi, A. Hosseini, H. Ghaznavi, S. Mehrzadi and A. M. Sharifi, *Brain Research Bulletin*, 2017, **131**, 117-122.
398. H. Bao, Z. Zhang, Q. Hua and W. Huang, *Langmuir*, 2014, **30**, 6427-6436.
399. L. Artiglia, S. Agnoli, M. C. Paganini, M. Cattelan and G. Granozzi, *ACS Applied Materials & Interfaces*, 2014, **6**, 20130-20136.
400. A. Othman, A. Hayat and S. Andreescu, *Acs Appl Nano Mater*, 2018, **1**, 5722-5735.
401. E. O. Gubernatorova, X. Liu, A. Othman, W. T. Muraoka, E. P. Koroleva, S. Andreescu and A. V. Tumanov, *Advanced Healthcare Materials*, 2017, **6**, 1700176.

402. H. Zhao, Y. Dong, P. Jiang, G. Wang and J. Zhang, *ACS Applied Materials & Interfaces*, 2015, **7**, 6451-6461.
403. A. A. Ansari, P. R. Solanki and B. D. Malhotra, *Applied Physics Letters*, 2008, **92**, 263901.
404. B. W. Liu, Z. C. Huang and J. W. Liu, *Nanoscale*, 2016, **8**, 13562-13567.
405. S. Radhakrishnan and S. J. Kim, *RSC Advances*, 2015, **5**, 12937-12943.
406. M. Molinari, A. R. Symington, D. C. Sayle, T. S. Sakthivel, S. Seal and S. C. Parker, *ACS Applied Bio Materials*, 2019, **2**, 1098-1106.
407. P. Pentyala, V. Singhania, V. K. Duggineni and P. A. Deshpande, *Molecular Catalysis*, 2022, **522**, 112190.
408. M. Chen, X. Zhou, C. Xiong, T. Yuan, W. Wang, Y. Zhao, Z. Xue, W. Guo, Q. Wang, H. Wang, Y. Li, H. Zhou and Y. Wu, *ACS Applied Materials & Interfaces*, 2022, **14**, 21989-21995.
409. A. Kolmakov and M. Moskovits, *Annu Rev Mater Res*, 2004, **34**, 151-180.
410. C. Schilling and C. Hess, *J Phys Chem C*, 2018, **122**, 2909-2917.
411. C. A. Zito, T. M. Perfecto, A. C. Dippel, D. P. Volanti and D. Koziej, *ACS Appl Mater Interfaces*, 2020, **12**, 17745-17751.
412. L. Lyu, Q. Xie, Y. Y. Yang, R. R. Wang, W. F. Cen, S. Y. Luo, W. S. Yang, Y. Gao, Q. Q. Xiao, P. Zou and Y. Yang, *Applied surface science*, 2022, **571**.
413. P. Jasinski, T. Suzuki and H. U. Anderson, *Sensor Actuat B-Chem*, 2003, **95**, 73-77.
414. H. J. Beie and A. Gnorich, *Sensor Actuat B-Chem*, 1991, **4**, 393-399.
415. T. Divya, M. P. Nikhila, M. Anju, T. V. A. Kusumam, A. K. Akhila, Y. T. Ravikiran and N. K. Renuka, *Sensor Actuat a-Phys*, 2017, **261**, 85-93.
416. L. S. R. Rocha, M. Cilense, M. A. Ponce, C. M. Aldao, L. L. Oliveira, E. Longo and A. Z. Simoes, *Physica B*, 2018, **536**, 280-288.
417. F. Charbgoo, M. Ramezani and M. Darroudi, *Biosens Bioelectron*, 2017, **96**, 33-43.
418. A. Hayat, J. Cunningham, G. Bulbul and S. Andreescu, *Analytica Chimica Acta*, 2015, **885**, 140-147.
419. A. Hayat and S. Andreescu, *Analytical Chemistry*, 2013, **85**, 10028-10032.
420. G. Bulbul, A. Hayat, X. B. Liu and S. Andreescu, *Rsc Advances*, 2016, **6**, 60007-60014.
421. A. Hayat, G. Bulbul and S. Andreescu, *Biosens Bioelectron*, 2014, **56**, 334-339.
422. F. Mustafa, S. Liebich and S. Andreescu, *Analytica Chimica Acta*, 2021, **1186**.
423. E. Sharpe, R. Bradley, T. Frasco, D. Jayathilaka, A. Marsh and S. Andreescu, *Sensor Actuat B-Chem*, 2014, **193**, 552-562.
424. V. Andrei, E. Sharpe, A. Vasilescu and S. Andreescu, *Talanta*, 2016, **156**, 112-118.
425. E. Sharpe, T. Frasco, D. Andreescu and S. Andreescu, *Analyst*, 2013, **138**, 249-262.
426. A. Othman, L. Norton, A. S. Finny and S. Andreescu, *Talanta*, 2020, **208**.
427. F. Mustafa, M. Carhart and S. Andreescu, *Acs Appl Nano Mater*, 2021, **4**, 9361-9369.
428. F. Mustafa, A. Othman and S. Andreescu, *Sensor Actuat B-Chem*, 2021, **332**.
429. J. Njagi, M. M. Chernov, J. C. Leiter and S. Andreescu, *Analytical chemistry*, 2010, **82**, 989-996.
430. R. E. Ozel, C. Ispas, M. Ganesana, J. C. Leiter and S. Andreescu, *Biosens Bioelectron*, 2014, **52**, 397-402.
431. N. P. Sardesai, M. Ganesana, A. Karimi, J. C. Leiter and S. Andreescu, *Analytical chemistry*, 2015, **87**, 2996-3003.
432. N. P. Sardesai, A. Karimi and S. Andreescu, *Chemelectrochem*, 2014, **1**, 2082-2088.
433. Z. H. Yang, Y. Zhuo, R. Yuan and Y. Q. Chai, *Biosens Bioelectron*, 2015, **69**, 321-327.
434. M. B. Gumpu, N. Nesakumar, S. Sethuraman, U. M. Krishnan and J. B. B. Rayappan, *Sensor Actuat B-Chem*, 2014, **199**, 330-338.
435. E. Kang, J. Lee, B. Y. Won, S. Kim, S. Shin, M. I. Kim and H. G. Park, *RSC Advances*, 2015, **5**, 78747-78753.

436. A. Pinna, E. Cali, G. Kerherve, G. Galleri, M. Maggini, P. Innocenzi and L. Malfatti, *Nanoscale Adv*, 2020, **2**, 2387-2396.
437. R. Khan and S. Andreescu, *Biosens Bioelectron*, 2024, **248**, 115975.
438. H. Y. Kim, J. K. Ahn, M. I. Kim, K. S. Park and H. G. Park, *Electrochem Commun*, 2019, **99**, 5-10.
439. H. Y. Kim, K. S. Park and H. G. Park, *Theranostics*, 2020, **10**, 4507-4514.
440. G. Bubul, A. Hayat and S. Andreescu, *Advanced Healthcare Materials*, 2016, **5**, 822-828.
441. A. Asati, S. Santra, C. Kaittanis, S. Nath and J. M. Perez, *Angew Chem Int Edit*, 2009, **48**, 2308-2312.
442. G. Bulbul, A. Hayat and S. Andreescu, *Nanoscale*, 2015, **7**, 13230-13238.
443. R. Wang, Y. Du, Y. Fu, Y. Guo, X. Gao, X. Guo, J. Wei and Y. Yang, *ACS sensors*, 2023, **8**, 4442-4467.
444. X. Z. Wang, B. W. Liu and J. W. Liu, *Langmuir*, 2018, **34**, 15871-15877.
445. B. W. Liu, Z. Y. Sun, P. J. J. Huang and J. W. Liu, *Journal of the American Chemical Society*, 2015, **137**, 1290-1295.
446. J. Y. Zhang, J. Wang, J. Liao, Y. Lin, C. B. Zheng and J. W. Liu, *ACS applied materials & interfaces*, 2021, **13**, 50236-50245.
447. Y. Y. Chang, Q. S. Chen, B. W. Liu, Z. J. Zhang, M. Liu and J. W. Liu, *Inorg Chem Commun*, 2021, **134**.
448. R. N. McCormack, P. Mendez, S. Barkam, C. J. Neal, S. Das and S. Seal, *J Phys Chem C*, 2014, **118**, 18992-19006.
449. M. Al Sharabati, R. Sabouni and G. A. Husseini, *Nanomaterials (Basel)*, 2022, **12**, 277.
450. Y. Ma, X. Qu, C. Liu, Q. Xu and K. Tu, *Frontiers in Molecular Biosciences*, 2021, **8**.
451. S. Wang, Z. Li, F. Duan, B. Hu, L. He, M. Wang, N. Zhou, Q. Jia and Z. Zhang, *Analytica Chimica Acta*, 2019, **1047**, 150-162.
452. N. Zhou, Y. Ma, B. Hu, L. He, S. Wang, Z. Zhang and S. Lu, *Biosensors and Bioelectronics*, 2019, **127**, 92-100.
453. X. Ouyang, W. Li, S. Xie, T. Zhai, M. Yu, J. Gan and X. Lu, *New Journal of Chemistry*, 2013, **37**, 585-588.
454. S. Olivera, K. Chaitra, K. Venkatesh, H. B. Muralidhara, Inamuddin, A. M. Asiri and M. I. Ahamed, *Environmental Chemistry Letters*, 2018, **16**, 1233-1246.
455. G. K. Sarma, S. Sen Gupta and K. G. Bhattacharyya, *Environmental Science and Pollution Research*, 2019, **26**, 6245-6278.
456. M. Lürling, G. Waajen and F. van Oosterhout, *Water Res.*, 2014, **54**, 78-88.
457. M. H. Hassan, R. Stanton, J. Secora, D. J. Trivedi and S. Andreescu, *ACS Applied Materials & Interfaces*, 2020, **12**, 52788-52796.
458. T. M. Arsic, A. Kalijadis, B. Matovic, M. Stoiljkovic, J. Pantic, J. Jovanovic, R. Petrovic, B. Jokic and B. Babic, *Process Appl Ceram*, 2016, **10**, 17-23.
459. A. Othman, P. Vargo and S. Andreescu, *Acs Appl Nano Mater*, 2019, **2**, 7008-7018.
460. W. Xu, J. Wang, L. Wang, G. Sheng, J. Liu, H. Yu and X. J. Huang, *J Hazard Mater*, 2013, **260**, 498-507.
461. R. Sawana, Y. Somasundar, V. S. Iyer and B. Baruwati, *Applied Water Science*, 2017, **7**, 1223-1230.
462. A. Baranik, A. Gagor, I. Queralt, E. Marguí, R. Sitko and B. Zawisza, *Microchimica Acta*, 2018, **185**, 264.
463. A. Karimi, S. Andreescu and D. Andreescu, *ACS applied materials & interfaces*, 2019, **11**, 24725-24734.
464. G. Zhang, Z. He and W. Xu, *Chemical Engineering Journal*, 2012, **183**, 315-324.
465. J. Wang, W. Xu, L. Chen, Y. Jia, L. Wang, X.-J. Huang and J. Liu, *Chemical Engineering Journal*, 2013, **231**, 198-205.
466. P. Zhang, T. Ouyang, S. Chen, R. Li and L. Lai, 2010 4th International Conference on Bioinformatics and Biomedical Engineering, 2010.

467. J. Lin, Y. Wu, A. Khayambashi, X. Wang and Y. Wei, *Adsorption Science & Technology*, 2018, **36**, 743-761.
468. K. Mukhopadhyay, A. Ghosh, S. K. Das, B. Show, P. Sasikumar and U. Chand Ghosh, *RSC Advances*, 2017, **7**, 26037-26051.
469. M. Chigondo, H. Kamdem Paumo, M. Bhaumik, K. Pillay and A. Maity, *J Colloid Interf Sci*, 2018, **532**, 500-516.
470. E. E. Merodio-Morales, H. E. Reynel-Ávila, D. I. Mendoza-Castillo, C. J. Duran-Valle and A. Bonilla-Petriciolet, *International Journal of Environmental Science and Technology*, 2019.
471. A. Dhillon, T. Kumar Sharma, S. K. Soni and D. Kumar, *RSC Advances*, 2016, **6**, 89198-89209.
472. J. G. Dale, S. S. Cox, M. E. Vance, L. C. Man and M. F. Hochella, *Environ Sci Technol*, 2017, **51**, 1973-1980.
473. L. Zhang, J. Pierce, V. L. Leung, D. Wang and W. S. Epling, *J Phys Chem C*, 2013, **117**, 8282-8289.
474. P. Dinesha, S. Kumar and M. A. Rosen, *Biofuel Res J*, 2021, **8**, 1374-1383.
475. J. X. Chen, Y. X. Chen, M. J. Zhou, Z. W. Huang, J. Y. Gao, Z. Ma, J. M. Chen and X. F. Tang, *Environ Sci Technol*, 2017, **51**, 473-478.
476. A. F. Santiago, J. F. Sousa, R. C. Guedes, C. E. Jeronimo and M. Benachour, *J Hazard Mater*, 2006, **138**, 325-330.
477. L. Chang, I. P. Chen and S. S. Lin, *Chemosphere*, 2005, **58**, 485-492.
478. S. S. Lin, C. L. Chen, D. J. Chang and C. C. Chen, *Water Res*, 2002, **36**, 3009-3014.
479. D. Wilson, W. Wang and R. J. G. Lopes, *Appl Catal B-Environ*, 2012, **123**, 273-281.
480. F. Carraro, A. Fapohunda, M. C. Paganini and S. Agnoli, *Acs Appl Nano Mater*, 2018, **1**, 1492-1501.
481. S. Kurajica, I. K. Ivkovic, G. Drazic, V. Shvalya, M. Duplancic, G. Matijasic, U. Cvelbar and K. Muzina, *Nanotechnology*, 2022, **33**.
482. P. K. Sane, S. Tambat, S. Sontakke and P. Nemade, *Journal of Environmental Chemical Engineering*, 2018, **6**, 4476-4489.
483. Y. W. Wang, T. T. Liu and J. W. Liu, *Acs Appl Nano Mater*, 2020, **3**, 842-849.
484. A. D. Mayernick, R. Li, K. M. Dooley and M. J. Janik, *J Phys Chem C*, 2011, **115**, 24178-24188.
485. Q. L. Wang, J. J. Zhou, J. C. Zhang, H. Zhu, Y. H. Feng and J. Jin, *Aerosol Air Qual Res*, 2020, **20**, 477-488.
486. Y. Z. Guo and H. Therien-Aubin, *ACS applied materials & interfaces*, 2021, **13**, 37578-37588.
487. D. J. Conley, H. W. Paerl, R. W. Howarth, D. F. Boesch, S. P. Seitzinger, K. E. Havens, C. Lancelot and G. E. Likens, *Science*, 2009, **323**, 1014-1015.
488. Y. G. Ko, T. Do, Y. Chun, C. H. Kim, U. S. Choi and J.-Y. Kim, *Journal of Hazardous Materials*, 2016, **307**, 91-98.
489. M. Teng, L. Luo and X. Yang, *Microporous Mesoporous Mater.*, 2009, **119**, 158-164.
490. Y. Zhang, M. Yang, X.-M. Dou, H. He and D.-S. Wang, *Environ Sci Technol*, 2005, **39**, 7246-7253.
491. Y. Su, W. Yang, W. Sun, Q. Li and J. K. Shang, *Chem. Eng. J.*, 2015, **268**, 270-279.
492. J. Liu, J. Cao, Y. Hu, Y. Han and J. Zhou, *Water Sci. Technol.*, 2017, **76**, 2867-2875.
493. H. Ding, Y. Zhao, Q. Duan, J. Wang, K. Zhang, G. Ding, X. Xie and C. Ding, *J. Rare Earth.*, 2017, **35**, 984-994.
494. M. A. Hassan, S., *Inorganic Chemistry*, 2023, **62, 51,** , 20970-20979.
495. A. Othman, D. Andreescu, D. P. Karunaratne, S. V. Babu and S. Andreescu, *ACS applied materials & interfaces*, 2017, **9**, 12893-12905.
496. E. Dumitrescu, D. P. Karunaratne, S. V. Babu, K. N. Wallace and S. Andreescu, *Chemosphere*, 2018, **192**, 178-185.
497. J. J. Zhang, K. B. Lee, L. He, J. Seiffert, P. Subramaniam, L. Yang, S. Chen, P. Maguire, G. Mainelis, S. Schwander, T. Tetley, A. Porter, M. Ryan, M. Shaffer, S. Hu, J. Gong and K. F. Chung, *Environmental science. Processes & impacts*, 2016, **18**, 1333-1342.

498. B. Collin, M. Auffan, A. C. Johnson, I. Kaur, A. A. Keller, A. Lazareva, J. R. Lead, X. M. Ma, R. C. Merrifield, C. Svendsen, J. C. White and J. M. Unrine, *Environ Sci-Nano*, 2014, **1**, 533-548.
499. A. Arumugam, C. Karthikeyan, A. S. Haja Hameed, K. Gopinath, S. Gowri and V. Karthika, *Materials Science and Engineering: C*, 2015, **49**, 408-415.
500. S. Kannan and M. Sundrarajan, *International journal of nanoscience*, 2014, **13**, 1450018.
501. G. S. Priya, A. Kanneganti, K. A. Kumar, K. V. Rao and S. Bykkam, *Int J Sci Res Publ*, 2014, **4**, 199-224.
502. S. Maensiri, C. Masingboon, P. Laokul, W. Jareonboon, V. Promarak, P. L. Anderson and S. Seraphin, *Crystal Growth & Design*, 2007, **7**, 950-955.
503. M. Darroudi, S. J. Hoseini, R. Kazemi Oskuee, H. A. Hosseini, L. Gholami and S. Gerayli, *Ceramics International*, 2014, **40**, 7425-7430.
504. S. A. Khan and A. Ahmad, *Materials Research Bulletin*, 2013, **48**, 4134-4138.
505. F. Charbgoo, M. B. Ahmad and M. Darroudi, *Int J Nanomedicine*, 2017, **12**, 1401-1413.
506. F. Zeng, Y. Wu, X. Li, X. Ge, Q. Guo, X. Lou, Z. Cao, B. Hu, N. J. Long, Y. Mao and C. Li, *Angewandte Chemie International Edition*, 2018, **130**.
507. J. L. Y. Tang, S. S. Moonshi and H. T. Ta, *Cellular and molecular life sciences : CMLS*, 2023, **80**, 46.
508. W. Yang, M. Zhang, J. He, M. Gong, J. Sun and X. Yang, *Regenerative biomaterials*, 2022, **9**, rbac037.
509. Q. Bao, P. Hu, Y. Xu, T. Cheng, C. Wei, L. Pan and J. Shi, *ACS Nano* 2018, **12, 7,** , 6794-6805.
510. Y. Malyukin, P. Maksimchuk, V. Seminko, E. Okrushko and N. Spivak, *J Phys Chem C*, 2018, **122**, 16406-16411.
511. R. W. Tarnuzzer, J. Colon, S. Patil and S. Seal, *Nano Lett*, 2005, **5**, 2573-2577.
512. M. Das, N. Bhargava, S. Patil, L. Riedel, P. Molnar, S. Seal and J. J. Hickman, *In Vitro Cellular & Developmental Biology-Animal*, 2005, **41**, 9A-9A.
513. G. A. Silva, *Nat Nanotechnol*, 2006, **1**, 92-94.
514. D. Schubert, R. Dargusch, J. Raitano and S. W. Chan, *Biochemical and Biophysical Research Communications*, 2006, **342**, 86-91.
515. J. M. Dowding, W. Song, K. Bossy, A. Karakoti, A. Kumar, A. Kim, B. Bossy, S. Seal, M. H. Ellisman, G. Perkins, W. T. Self and E. Bossy-Wetzel, *Cell Death Differ*, 2014, **21**, 1622-1632.
516. D.-W. Kang, C. K. Kim, H.-J. Jeong, M. Soh, T. Kim, I. Choi, C.-K. Ki, D. Kim, W. Yang, T. Hyeon and S.-H. Lee, *NanoResearch*, 2017, **10**, 2743-2760.
517. H. Nosrati, M. Heydari and M. Khodaei, *Materials today. Bio*, 2023, **23**, 100823.
518. A. P. Dayanandan, W. J. Cho, H. Kang, A. B. Bello, B. J. Kim, Y. Arai and S. H. Lee, *Biomaterials research*, 2023, **27**, 68.
519. Y. Xue, F. Yang, L. Wu, D. Xia and Y. Liu, *Adv Healthc Mater*, 2024, **13**, e2302858.
520. Q. Weng, H. Sun, C. Fang, F. Xia, H. Liao, J. Lee, J. Wang, A. Xie, J. Ren, X. Guo, F. Li, B. Yang and D. Ling, *Nature Communications*, 2021, **12**.
521. A. García, J. A. Cámara, A. M. Boullosa, M. Gustà, L. Mondragón, S. Schwartz, E. Casals, I. Abasolo, N. J. Bastús and V. Puntes, *Nanomaterials*, 2023.
522. P. C. Naha, J. C. Hsu, J. Kim, S. Shah, M. Bouche, S. Si-Mohamed, D. N. Rosario-Berrios, P. Douek, M. Hajfathalian, P. Yasini, S. Singh, M. A. Rosen, M. A. Morgan and D. P. Cormode, *ACS Nano*, 2020, **14**, 10187-10197.
523. S. Kargozar, F. Baino, S. J. Hoseini, S. Hamzehlou, M. Darroudi, J. Verdi, L. Hasanzadeh, H. W. Kim and M. Mozafari, *Nanomedicine (Lond)*, 2018, **13**, 3051-3069.